

ISTANBUL TECHNICAL UNIVERSITY ★ GRADUATE SCHOOL OF SCIENCE
ENGINEERING AND TECHNOLOGY

**AN EXPERIMENTAL STUDY OF SHOCK WAVE/BOUNDARY LAYER
INTERACTIONS IN SUPERSONIC INLETS**

M.Sc. THESIS

Serdar SEÇKİN

Department of Aeronautics and Astronautics Engineering

Aeronautics and Astronautics Engineering Programme

JUNE 2014

ISTANBUL TECHNICAL UNIVERSITY ★ GRADUATE SCHOOL OF SCIENCE
ENGINEERING AND TECHNOLOGY

**AN EXPERIMENTAL STUDY OF SHOCK WAVE/BOUNDARY LAYER
INTERACTIONS IN SUPERSONIC INLETS**

M.Sc. THESIS

Serdar SEÇKİN
(51121186)

Department of Aeronautics and Astronautics Engineering

Aeronautics and Astronautics Engineering Programme

Thesis Advisor: Asst. Prof. Dr. K. Bülent YÜCEİL

JUNE 2014

İSTANBUL TEKNİK ÜNİVERSİTESİ ★ FEN BİLİMLERİ ENSTİTÜSÜ

**SESÜSTÜ HAVA ALIKLARINDA ŞOK DALGASI SINIR TABAKASI
ETKİLŞİMİNİN DENEYSEL İNCELENMESİ**

YÜKSEK LİSANS TEZİ

**Serdar SEÇKİN
(51121186)**

Uçak ve Uzay Mühendisliği Anabilim Dalı

Uçak ve Uzay Mühendisliği Programı

Tez Danışmanı: Y. Doç. Dr. K. Bülent YÜCEİL

HAZİRAN 2014

Serdar SEÇKİN, a **M.Sc.** student of ITU **Graduate School of Science Engineering and Technology** student ID **511121186**, successfully defended the **thesis** entitled “**AN EXPERIMENTAL STUDY OF SHOCK WAVE/BOUNDARY LAYER INTERACTIONS IN SUPERSONIC INLETS**”, which he prepared after fulfilling the requirements specified in the associated legislations, before the jury whose signatures are below.

Thesis Advisor : **Asst. Prof. Dr. K. Bülent YÜCEİL**
Istanbul Technical University

Jury Members : **Asst. Prof. Dr. Bayram ÇELİK**
Istanbul Technical University

Prof. Dr. Mustafa ÖZDEMİR
Istanbul Technical University

Date of Submission : 05 May 2014
Date of Defense : 29 May 2014

To my family,

FOREWORD

Foremost, I would like to express my initial gratitude and appreciation to my supervisor, Asst. Prof. Dr. K. Bülent YÜCEİL, for encouraging, guiding and supporting me in this study.

I would like to like to thank technicians Aliosman TABANLI and Murat TARHAN for their help during model manufacturing process.

Trisonik Laboratory, with its family-like atmosphere, has a significant positive effect on my studies. I would like to thank every person for their support.

I am also thankful to Berkay AÇIKGÖZ for his great knowledge and help on CFD analyses and I would like to thank to Zeynep ASLAN, Bertan KAYNAROĞLU, Selman MESTANLI, Hasan TABANLI and Onur SON for their support and help in my study.

Above all, I am especially very grateful to my lovely friends for being with me in many memorable moments and motivating me all the time to write this thesis.

At last but at most, one more time I realized how glorious family I have. I would like to express very special thanks to my mother, father and sister who never hesitated to support me and always give countenance to me.

June 2014

Serdar SEÇKİN

TABLE OF CONTENTS

	<u>Page</u>
FOREWORD	ix
TABLE OF CONTENTS	xi
ABBREVIATIONS	xiii
LIST OF TABLES	xv
LIST OF FIGURES	xvii
SUMMARY	xix
ÖZET	xxiii
1. INTRODUCTION	1
1.1 Purpose of Thesis	1
1.2 Literature Review	2
1.2.1 Subsonic Inlets	2
1.2.2 Supersonic Inlets	5
1.2.2.1 Internal Compression Inlets	5
1.2.2.2 External Compression Inlets	9
1.2.2.3 Mixed Compression Inlets	13
1.2.3 Flow Control Mechanism.....	15
2. EXPERIMENTAL SETUP	17
2.1 Wind Tunnel.....	17
2.2 Shadowgraph System	22
2.3 Schlieren System	23
2.4 Surface Oil Flow Visualization	25
2.5 Internal Compression Inlet Model.....	26
2.6 Pressure Transducers.....	28
3. RESULTS	31
3.1 External Compression Inlets	31
3.2 Internal Compression Inlets	36
3.2.1 Analytical Calculations	36
3.2.2 CFD Analyses	39
3.2.3 Experimental Results	48
4. CONCLUSIONS AND RECOMMENDATIONS	61
REFERENCES	63
APPENDICES	65
APPENDIX A	66
CURRICULUM VITAE	71

ABBREVIATIONS

2D	: Two-Dimensional
AUSM	: Advection Upstream Splitting Method
C-D	: Converging Diverging
CAD	: Computer Aided Design
CFD	: Computational Fluid Dynamics
CNC	: Computer Numeric Control
FFT	: Fast Fourier transform
RMS	: Root Mean Square
SBLI	: Shock Wave Boundary Layer Interaction
SPL	: Sound Pressure Level

LIST OF TABLES

	<u>Page</u>
Table 3.1 : Design calculations for external compression inlet performance.	35
Table 3.2 : Analytical results of the 1 st internal compression inlet model.	38
Table 3.3 : Analytical results of the 2 nd internal compression inlet model.	39
Table 3.4 : Mesh properties.	40
Table 3.5 : Boundary conditions of CFD model.	41
Table 3.6 : Analysis methodology.	42
Table 3.7 : Mach number range outputs of the inviscid 2 nd model.	44
Table 3.8 : Experiments with blocks at the back of the model.	52

LIST OF FIGURES

	<u>Page</u>
Figure 1.1 : Typical oncoming flow patterns for subsonic inlets.....	3
Figure 1.2 : Schematic diagram of captured streamtube by inlet.....	3
Figure 1.3 : Maximum mass flow passed by the inlet.	4
Figure 1.4 : Flow structure around small and large lip radius [3].....	4
Figure 1.5 : Flow through duct with internal throat.....	6
Figure 1.6 : Shock wave positions in the internal compression inlet.....	7
Figure 1.7 : Required throat area variation of an internal compression inlet.....	7
Figure 1.8 : Area relationships of an internal compression inlet [1].....	8
Figure 1.9 : Captured area to throat area ratio of an internal compression inlet.....	8
Figure 1.10 : External compression inlet types [2].	10
Figure 1.11 : Character of normal shock loss [4].....	11
Figure 1.12 : Shock pressure recovery for two-dimensional shocks [4].	11
Figure 1.13 : Difference between wedge and cone flows [4].	12
Figure 1.14 : Different flow conditions at Mach number below design [4].	12
Figure 1.15 : 4 shock inlets types designed for Mach 2.....	14
Figure 1.16 : F-14 inlet characteristics [7].	15
Figure 2.1 : Supersonic wind tunnel compressors and tanks.	19
Figure 2.2 : Supersonic wind tunnel test section and other components.	19
Figure 2.3 : Axial Control Valve from Mokveld Company.....	20
Figure 2.4 : Nickel membrane.....	20
Figure 2.5 : Test section module and the designed inlet model assembly.	21
Figure 2.6 : Mounting apparatus.	22
Figure 2.7 : Schematic of shadowgraph system [18].	23
Figure 2.8 : Schematic of a schlieren system [18].	24
Figure 2.9 : Schlieren system with mirrors [19].	24
Figure 2.10 : Schilieren system of the supersonic wind tunnel.	25
Figure 2.11 : Side view of upper and lower ramps for the 2 nd model.....	26
Figure 2.12 : Details of the model assembly and components.....	27
Figure 2.13 : Kulite transducers for pressure measurements.	28
Figure 2.14 : Assembly details of Kulite transducers.	28
Figure 2.15 : Designed LabVIEW interface for measurements.....	29
Figure 3.1 : Total pressure recovery of external compression inlets.	32
Figure 3.2 : Schematic diagram of external compression inlets.	34
Figure 3.3 : Shock wave structure of the 1 st internal compression inlet model.	37
Figure 3.4 : Interior flow regions of the 1 st internal compression inlet model.	38
Figure 3.5 : Shock wave structure of the 2 nd internal compression inlet model.	38
Figure 3.6 : Interior flow regions of the 2 nd internal compression inlet model.....	39
Figure 3.7 : Cell edge length details of viscous 2 nd model.	40
Figure 3.8 : Boundaries of the CFD model.....	41
Figure 3.9 : Mach contours.	43
Figure 3.10 : Vector field of the viscous calculations for the 2 nd model.	45

Figure 3.11 : p/p_∞ contours.	46
Figure 3.12 : ρ/ρ_∞ contours.	47
Figure 3.13 : Shadowgraph image of the 1 st model at Mach 2.03.	49
Figure 3.14 : Shadowgraph image of the flow around 2 nd model at Mach 2.03.	50
Figure 3.15 : Shadowgraph image at Mach 2.02.	51
Figure 3.16 : $p_\# / p_\infty$ values of Run2349.	53
Figure 3.17 : Short started model without block.	54
Figure 3.18 : Short unstated model with block in the center height at the back.	55
Figure 3.19 : Long started model without block.	56
Figure 3.20 : Long unstated model with block in the center height at the back.	57
Figure 3.21 : Oil flow image of short started model.	58
Figure 3.22 : Planar shock-wave/boundary-layer interaction [20].	58
Figure A.1 : Power spectra of the tare pressure at P1, P2 and P3 for Run2352.	66
Figure A.2 : Power spectra of the tare pressure at P4, P5 and P6 for Run2352.	67
Figure A.3 : Power spectra of the pressure at P1, P2 and P3 for Run2352.	68
Figure A.4 : Power spectra of the pressure at P4, P5 and P6 for Run2352.	69

AN EXPERIMENTAL STUDY OF SHOCK WAVE/BOUNDARY LAYER INTERACTIONS IN SUPERSONIC INLETS

SUMMARY

Air breathing engines use the jet flow of exhaust gases formed by combustion of air that enters the engine from the inlet. In order to operate the engine at high efficiency, the inlet design is of vital importance to supply the desired flow conditions. General requirements expected from inlets can be listed as; to capture the sufficient volume of air required by the engine, to provide low total pressure loss by efficiently compressing the airflow, to have low external drag, to operate over the designed range of Mach numbers and angles of attack, to have a good starting and stability characteristics, to produce uniform subsonic flow field after the required compression and to have a small, simple and lightweight design. Experimental and computational investigations with analytical calculations were performed for this purpose.

In a typical gas turbine, air velocity at compressor entrance ranges from Mach 0.4 to 0.5. Inlets are basically used to achieve desired flow conditions at gas turbine entrance and are classified as subsonic and supersonic inlets. Supersonic inlets can be categorized as internal compression inlets, external compression inlets and mixed compression inlets.

Inlets are one of the most crucial components for air breathing engines and experimental investigation of inlets is indispensable for engine performance where SBLI is an essential issue for all types of inlets. Since this interaction creates complex and unsteady flow fields commonly experimental investigation is the most appropriate way to understand the underlying physics. The primary purpose of this study is to obtain a proper shock system for internal compression inlets where one or more oblique shock reflections are formed followed by a terminating normal shock. After completing the preliminary design with the help of CFD analyses and analytical calculations, experiments were performed and the results showed the unstable characteristics of internal compression inlets, which were hard to control. Therefore, external compression inlets are more preferable on the basis of shock stability and inlet performance. This thesis is, in part, a follow-up study of the previously carried out national industrial subproject related to the conceptual preliminary design of the simplified external compression inlet model of TX/FX National Training/Fighter Aircraft. By using the experience coming from this previous project, a complementary analytical study was carried out related to the optimization of total pressure recovery for external compression inlets which were more feasible than internal compression inlets in reality.

The experiments were performed at supersonic wind tunnel of Trisonic Research Laboratory in Istanbul Technical University. The wind tunnel is a blowdown type and has a test section with a cross section of 15×15 cm and a length of 40 cm. Mach number in the test section can be adjusted between 0.4 – 2.2. Side walls of the test section consist of quartz windows for optical access and top and bottom walls are equipped with perforated plates to supply suction/blow. Some modifications were made on the

bottom wall by replacing the suction/blow mechanism and the perforated plate with a plain wall piece designed to be able to mount the inlet model on the test section floor. Two high pressure air tanks each of which has a volume of 40 m³ supply air for the experiments. The ambient air is pressurized and stored in the tanks by a two-stage screw-type compressor system up to 40 bars. Filters and a chemical dryer are used to eliminate the oil, dust and humidity. An isolation valve separates the high pressure tanks from the rest of the system. During experiments, isolation valve is opened and the air is sent to the regulation valve in order to adjust the pressure in the settling chamber to a desired value. Supersonic flow is obtained by a convergent-divergent nozzle with a variable throat and a diffuser is used at the exit of the test section to slow down the flow to subsonic speeds.

An internal compression inlet was designed and manufactured. For optical access, side walls of the model were made of acrylic and the rest of the components machined from brass to withstand the aerodynamic loads. Moreover, a support was manufactured to keep the inlet model away from the relatively thick boundary layer on the bottom surface of the test section. Since acrylic side walls of the inlet model produced a second focal point in the schlieren visualization apart from the main flow outside the inlet, shadowgraph visualization system was used instead of schlieren system to obtain more distinct contrast on the recorded image of shock waves. Because of their good static and dynamic characteristics, fast-response Kulite transducers were used for pressure measurements. Pressure data were obtained up to 100 kHz for FFT analyses. In addition, surface oil flow visualization method was used to reveal the separation/reattachment lines formed by SBLIs.

At first, an analytical study was carried out in order to understand the limits of inlet geometry and to determine primary performance characteristics for external compression inlets. For this purpose, a MATLAB code was written by using shock wave and isentropic flow properties under inviscid approach. Total pressure recovery at various Mach numbers ranging from 1.3 to 5 was obtained for five different shock systems. Secondly, the ramp angle was chosen as 4° for a symmetrical internal compression inlet. Another code calculating shock-shock and shock-expansion interactions analytically was written to calculate the properties of the shock structure within the inlet. The inlet model designed firstly remained in the not-started condition in the experiments due to the high captured area to throat area ratio. Therefore, a second model was formed by enlarging the throat height of the first model. 2D CFD analyses of both models were performed for both inviscid and viscous cases and the results appeared to be compatible with the analytical results. On the other hand, even though the first model was analyzed and calculated as a started inlet, experiments showed the opposite. In the experiments, Mach number was set to about 2. The purpose was to obtain one or more oblique shocks followed by a normal shock. To obtain this condition, various block shapes and sizes were tested but non of the runs illustrated this condition. The inlet model either remained started or not-started. Pressure measurements in the experiments showed a good agreement with the calculated results. RMS values were observed to be higher near SBLI regions. In addition, the inlet was modified by extending the length but results from pressure measurements and shadowgraph images were nearly the same as the shorter model. The primary purpose was to make FFT analyses and obtain SPL values to find a dominant frequency related to the duct length of the subsonic portion of the inlet after the normal shock. Since no normal shock structure was obtained inside the inlet, no normal shock/boundary layer interaction occurred. No dominant frequency was observed for the unstarted inlet condition where the normal shock stayed at the tip of the inlet. Finally, surface oil flow

visualization method was used to see the separation lines caused by SBLI regions and two separation lines were observed in two different locations along the inlet floor. A total of about 70 experiments were performed and the difficulties about starting and unstart phenomena of internal compression inlets were presented with analytical calculations, computational analyses and experimental investigations.

SESÜSTÜ HAVA ALIKLARINDA ŞOK DALGASI SINIR TABAKASI ETKİLEŞİMİNİN DENEYSEL İNCELENMESİ

ÖZET

Hava soluyan motorlar, hava alığından giren havanın yakıt ile karıştırılarak yanmasıyla oluşan egzoz gazlarının motordan çıkarken oluşturduğu jet etkisini kullanan motorlardır. Motorun verimli bir şekilde çalışması için istenilen giriş koşullarını sağlayabilen hava alığı tasarımı önemli bir role sahiptir. Hava alıklarında genel olarak istenilen özellikler şu şekilde sıralanabilir; motor için gerekli debiyi sağlamak, toplam basınç kaybını minimuma indirecek şekilde gelen havayı etkili bir şekilde sıkıştırmak, düşük sürüklemeye sahip olmak, farklı hücum açılarında ve Mach sayılarında çalışabiliyor olmak, iyi bir başlatma ve kararlılık karakterine sahip olmak, uygun sıkıştırma sisteminden sonra düzgün bir akış alanı oluşturmak ve küçük, basit ve hafif bir tasarıma sahip olmak. Bu amaçta geniş kapsamda analitik hesaplar yardımı ile deneysel çalışmalar ve hesaplamalı akışkanlar dinamiği analizleri gerçekleştirilmiştir.

Tipik bir gaz türbininde kompresör hava giriş hızı 0.4 – 0.5 Mach aralığındadır. Hava alıkları temel olarak serbest akımı, arzulanan gaz türbini giriş şartlarına getirmek için kullanılmaktadır ve genel olarak sesaltı ve sesüstü olarak sınıflandırılabilir. Sesüstü hava alıklarının ise iç sıkıştırmalı, dış sıkıştırmalı ve karışık sıkıştırmalı çeşitleri bulunmaktadır.

Hava alıkları jet motorlarının en önemli bileşenlerinden biridir. Jet motorunun performansı hava alığının doğru bir şekilde tasarlanmasına bağlıdır. Bu nedenle hava alıklarının deneysel olarak incelenmesi son derece önem arz etmektedir. Bu araştırmalarda genellikle tüm hava alığı tipleri için ana konu şok dalgası-sınır tabakası etkileşimleridir. Bu etkileşimler karmaşık ve zamana bağlı akış alanları yaratarak hava alığının performansını etkileyen önemli bir problem olarak ortaya çıkar. Bu yüzden etkileşimlerin karmaşık ve zamana bağlı karakterinin incelenemesinin en uygun yolu deneysel yöntemler kullanmaktır. Ön tasarımın ortaya çıkmasında hesaplamalı akışkanlar dinamiği analizleri ve analitik hesaplamalar kullanılmıştır ve daha sonra deneylere geçilmiştir. Bu çalışmadaki asıl amaç iç sıkıştırmalı bir hava alığında bir ya da daha fazla eğik şok yansımalarının ardından bir normal şok oluşturarak bu etkileşimleri incelemektir. Fakat yapılan deneyler sonucunda seçilen hava alığı geometrisi için böyle bir durumun elde edilemeyeceği gözlemlenmiştir. Deneylerden elde edilen sonuçlar doğrultusunda iç sıkıştırmalı hava alıklarının çok kararsız bir yapıya sahip olduğu ve içindeki akış yapısının kontrolünün çok zor olduğu anlaşılmıştır. Bu teze ayrıca daha önce aynı deney sisteminde incelenen ulusal bir endüstri projesi olan TX\FX ulusal eğitim/savaş uçağının kavramsal ön tasarımındaki basitleştirilmiş dış sıkıştırmalı hava alığındaki şok dalgası-sınır tabakası etkileşimi çalışmasının iç sıkıştırmalı hava alıklarına olan uzantısını yapmak amacıyla başlanmıştır. TX\FX projesinden de kazanılan tecrübe ile dış sıkıştırmalı alıkların şok dalgalarının kararlılığı ve alık performansı açısından iç sıkıştırmalı alıklara göre daha uygun ve genel anlamda daha tercih edilebilir bir alık tipi olduğu sonucuna varılmıştır.

Bu doğrultuda dış sıkıştırılmalı alıklar için tamamlayıcı bir analitik çalışma yapılarak alık performansını arttırıcı bir toplam basınç geri kazanımı optimizasyonu gerçekleştirilmiştir.

Deneyler İstanbul Teknik Üniversitesi'nde Trisonik Araştırma Merkezi'nde bulunan sesüstü rüzgar tüneline gerçekleştirilmiştir. Tünel tipi üflemlerli rüzgar tüneline olup, test odasının kesiti 15×15 cm, uzunluğu ise 40cm'dir. Test odasında Mach sayısı değişken kesitli bir boğaz yardımıyla 0.4 ile 2.2 arasında ayarlanabilmektedir. Gerekli olması durumunda, daha yüksek Mach sayılarına ulaşabilen (2.6 – 4.0) ikinci bir test odası var olan sistem ile değiştirilebilmektedir. Test odasının yan duvarlarında bulunan kalın kuartz camlar akım görüntüleme methodları için optik erişim sağlarken, alt ve üst duvarlarda bulunan delikli yüzeyler emme/üfleme sağlamaktadır. Tünelin orijinal model bağlama sistemi mermi/füze tipinde aksel simetrik cisimlerin bağlanmasına uygun bir bağlantı çubuğu şeklindedir. Hava alık tipi aksel simetrik olmayan modellerinin test odasına bağlanması sırasında karşılaşılan problemlerden dolayı, modifiye çalışmaları başlatılmış ve bu kapsamda, deney odasının alt yüzeyinde bulunan gözenekli plaka ile birlikte bunun altında bulunan sınır tabaka emme/üfleme mekanizması kaldırılarak yerine hava alığı benzeri modellerin deney odası tabanına bağlanmasına uygun yeni bir taban bağlantı aparatı tasarlanıp üretilmiştir. Deneyler için gerekli hava herbiri 40 m³ olan iki adet yüksek basınç tankından sağlanmaktadır. Tanklara hava iki ayrı vidalı kompresör yardımıyla doldurulmaktadır. Kompresörlerden ilki atmosferden aldığı havayı 10 bara kadar basınçlandırır ve ikinci kompresör bu havayı 40 bara kadar çıkartır. Aradaki filtreler yardımı ile havanın içerisindeki yağ ve toz parçacıkları arındırılır. Kompresör çıkışında yüksek basınçlı hava soğutucudan geçerek kimyasal kurutucuya gönderilir. Kimyasal kurucunun sıra ile çalışan iki ayrı kulesi mevcuttur. Yüksek basınç altında havanın içindeki nem kulelerde bulunan kimyasal oluşumların yüzeyine tutunarak havanın kurutulması sağlanır. Kurutulmuş basınçlı havanın geri kaçmasını engellemek için tek yön akış vanası bulduran bir ayar tankı kullanılır ve basınçlandırılmış hava yüksek basınç tanklarına depolanır. Tankların çıkışında bulunan izolasyon vanası depolanmış yüksek basınçlı havayı sistemin geri kalanından ayırmaktadır. Deney yapılacağı sırada bu valf açılarak basınçlı hava ayar vanasına gönderilir ve dinlenme odasında elde edilmek istenilen basınca ayarlanır. Dinlenme odasında çalkantısı azaltılmış akış yakınsak-iraksak lüle yardımıyla istenilen sesüstü hız, boğaz kesit alanını ayarlayabilen bir motor yardımıyla ulaştırılır. Test odasından geçen hava çıkışta bulunan bir difüzör yardımıyla sesaltı hızlara düşürülerek tekrar atmosfere bırakılır.

Yapılan bu tez çalışmasında, iç sıkıştırılmalı bir sesüstü hava alığı, çeşitli akım görüntüleme yöntemleri ile incelenmiş, basınç duyargaları ile hava alığı modeli içerisinde yüzey boyunca çeşitli istasyonlarda statik basınç verisi farklı örnekleme frekanslarında dinamik olarak elde edilmiştir. Hava alık modelinde alt ve üst rampalar pirinç, yan duvarlar ise alık içerisinde oluşan şok dalgalarını görüntüleyebilmek için saydam akrilik (pleksiglas) malzemeden üretilmiştir. Modelin arkasına çeşitli bloklar yerleştirilmiştir. Bu blokların dikdörtgen kesitli olanları yine akrilik malzemeden bir lazer kesici ile kesilmiştir, daire kesitli olanlar için de çelik civata gövdeleri kullanılmıştır. Modelin geri kalan tüm bileşenleri aerodinamik yüklere dayanıklı olması açısından pirinç malzemeden üretilmiştir. Ek olarak modeli tüneline kalın sınır tabakasından yukarıda tutmak için yine pirinç malzemeden bir ara parça üretilmiştir. Alt rampada orta eksen boyunca basınç ölçümü yapabilmek için çeşitli istasyonlarda basınç duyargalarının yerleştirilebileceği delikler açılmıştır. Hava alık modeli, alık uzunluğunun etkisini incelemek amacıyla orijinal alığa eklenebilen akrilik yüzeylerle uzatılıp aynı şartlar korunarak deneyler tekrarlanmıştır. Gerçeğe yakın koşullar elde

etmek amacıyla, modelin arkasına motorun varlığının yaratacağı benzer basınç artışını sağlayabilecek, çeşitli büyüklüklerde bloklar monte edilmiştir ve hava alığı “başlamama” (“unstart”) durumu incelenmiştir. Akrilik yan duvarlar ikinci bir odak noktası yarattığı için schlieren yöntemi kullanılırken bıçak sırtının yeri tam olarak ayarlanamamaktadır. Bu nedenle şok dalgalarını daha net görebilmek için gölgeleme yöntemi kullanılmıştır. Gölgeleme yöntemi temel olarak akışkan yoğunluğundaki değişimin ikinci türevine duyarlı olduğundan şok dalgalarının görüntülenmesini sağlar. Basınç ölçümleri için iyi bir statik ve yüksek dinamik cevabı olan Kulite marka duyarlılar kullanılmıştır. FFT analizleri için 25, 50 ve 100 kHz’de bir çok basınç datası ölçümü yapılmıştır. Ayrıca yağ ile yüzey akım görünürlüğü ile şok dalgası-sınır tabakası etkileşimi sonucunda meydana gelebilecek akım ayrılması bölgelerini sınırlayan, yüzeydeki ayrılma ve yeniden yapışma çizgileri tespit edilmiştir.

İlk olarak dış sıkıştırılmalı alıkların geometrik limitlerini ve birincil performans karakterlerini anlamak için analitik bir çalışma yapılmıştır. Bunun için viskoz etkilerin hesaba katılmadığı şok dalgası ve izentropik akış denklemlerini kullanan bir MATLAB kodu yazılmıştır. 5 ayrı şok sistemi için Mach sayısının 1.3’ten 5’e kadar değiştiği aralıkta toplam basınç kazanımı grafiği elde edilmiştir. Böylece Mach sayısı arttıkça rampa sayısının da artması gerekliliğinin önemi gösterilmiş ve rampa açılarının düşükten başlayarak giderek büyüyecek şekilde tasarlanması gerektiği sonucuna varılmıştır. Analitik çalışmaların devamında rampa açıları 4° olarak simetrik bir iç sıkıştırılmalı alık modeli seçilmiştir. İkinci bir kod yazılarak iki şok dalgasının kesişimi ve bir şok dalgasının bir genişleme dalgasıyla kesişimi hesaplanarak alığın içinde oluşan şok yapıları belirlenmiştir. Tasarlanan ilk alık modeli yüksek alan oranı (giriş alanının boğaz alanına oranı) nedeniyle deneylerde başlamamış alık durumunda kalmıştır. Bu nedenle boğaz alanı hem üstten hem de alttan 2 mm tıraşlanarak toplamda 4 mm büyütülmüştür. Böylelikle ikinci alık modeli oluşturulmuştur. Hem viskoz hem de viskoz olmayan durumlarda her iki model için iki boyutlu hesaplamalı akışkanlar dinamiği analizleri yapılmıştır. Analiz sonuçlarının analitik sonuçlarla uyumlu olduğu görülmüştür. Diğer taraftan her ne kadar ilk model başlamış bir alık olarak hesaplanmış ve analiz edilmiş olsa da, deneyler daha önce de belirtildiği gibi alan oranı nedeniyle bu durumun tersini göstermiştir. Deneylerde Mach sayısı 2.0’a ayarlanmıştır fakat sonuçlar her zaman tam olarak 2.0 çıkmamaktadır ve ilk ondalık basamakta ufak değişiklikler olabilmektedir. Deneylerde amaç bir ya da daha fazla eğik şok dalgası yansımalarının ardından bir normal şok dalgası ile serbest akım hızının ses altına düşürülmesiydi. Bu nedenle çeşitli büyüklüklerde blok modelleri deneyerek alığın çıkışındaki basınç arttırılmıştır. Alığın içerisinde normal şok oluşturacak basınç artışını yakalayabilmek için farklı kalınlıklardaki blok modelleriyle ve kombinasyonlarıyla bir çok deneme yapılmıştır. Fakat deneylerin hiçbirinde istenilen koşul sağlanamamıştır. Alık modeli ya başlamış alık olarak kalmakta ya da başlamamış alık durumuna geçmektedir. Deneylerin sonucunda bu kararsız yapının iç sıkıştırılmalı alıklar için büyük bir problem oluşturduğu gözlemlenmiştir. Basınç ölçümlerinin analitik hesaplarla ve hesaplamalı akışkanlar dinamiği analizleriyle son derece benzer sonuçlar verdiği görülmüştür. Basınç ölçümlerinden elde edilen RMS değerlerinin şok dalgası-sınır tabakası etkileşimlerinin olduğu bölgelerde arttığı gözlemlenmiştir. Ek olarak alık modelinin arkası uzatılarak bloklu ve bloksuz şekilde deneyler tekrarlanmıştır. Elde edilen sonuçlarda uzun modelin kısa modelle benzer sonuçlar verdiği görülmüştür. Uzun modelle yapılan deneylerde alığın içinde yine normal şok elde edilememiştir. Deneylerde yapılan basınç ölçümlerindeki birincil amaç FFT analizleri yaparak frekansa bağlı SPL değerlerini elde etmek ve alık modelinin içinde normal şok arkasındaki ses altı bölgenin uzunluğuyla elde edilen

baskın frekans arasında bir ilişki kurmaktı. Fakat alık içerisinde bir normal şok elde edilemediği için normal şok ile sınır tabaka etkileşimi oluşmamış. Bu nedenle normal şokun alığın ağzında yani iç bölgenin ses altı olduğu durumlarda elde edilen ölçümlerde baskın bir frekans bulunamamıştır. Son olarak yağ ile yüzey akım görünürlüğü yönteminin kullanıldığı deneylerde şok dalgası-sınır tabakası etkileşiminin olduğu iki ayrı bölgelerde ayrılma çizgisi görülmüştür. Bu ayrılma çizgileri şok dalgasının arkasında oluşan ters basınç nedeniyle sınır tabakanın kalınlaşarak akım ayrılmasına sebep olduğunu göstermektedir. Toplamda 70'ten fazla deney yapılmış ve iç sıkıştırılmalı alıkların başlama problemi ve unstart olma karakteri analitik hesaplarla, hesaplamalı akışkanlar dinamiği analizleriyle ve deneysel araştırmalarla ortaya koyulmuştur.

1. INTRODUCTION

Inlets are one of the most important components for aircraft that enable to capture required amount of airflow for engines. They are located headmost of the air breathing system and provide the rest of the system with diminishing the freestream flow to required low speeds and increasing the static pressure with the maximum possible total pressure recovery. Handling off-design conditions and overcoming unstart problems carry an important role for a robust design. Therefore, shock structure and SBLIs should be examined well for the performance of a supersonic inlet.

1.1 Purpose of Thesis

Since inlets are the essential components for air breathing engines, experimental investigation of an inlet is of prime importance for engine development. SBLI is an important issue for both external and internal compression inlets, which affects the inlet performance significantly. This interaction causes complex and unsteady flow fields which are generally investigated experimentally. The main purpose of this thesis is to obtain a proper shock system for an internal compression inlet and investigate the SBLIs and unsteady characteristics of the flow field. Preliminary 2D CFD analyses were used to estimate the flow field, the transducer locations and the dimensions of the inlet model. Furthermore, experimental results supply benchmark data for further CFD studies. Comparison between analytical calculations and experimental results is made in order to obtain a better understanding of SBLI effects. This thesis is, in part, a follow-up study of the previously carried out national industrial subproject related to the conceptual preliminary design of the TX\FX National Training/Fighter Aircraft, which is based on the investigation of SBLI in an external compression inlet using the same experimental facilities. Due to the unsteadiness of shock wave boundary layer interactions, unstart phenomena and starting problems of internal compression inlets, with the experience from the national industrial project it was concluded that external compression inlets were more feasible on the basis of shock stability and inlet performance. Therefore, another analytical study was carried out to optimize the total

pressure recovery performance of external compression inlets. Thus, a general overview was provided with this thesis about the problems caused by SBLIs and the selection of the right inlet type for better inlet performance.

1.2 Literature Review

For air breathing engines, inlets are the most crucial component that directly interacts with the surrounding air. Since subsonic airflow is required at the entrance of engines or in the combustion chamber for ramjet engines, supersonic inlets should provide a proper shock system to decelerate the incoming supersonic freestream to subsonic velocities. The tip speed of the compressor blades should be about Mach 0.4 – 0.5 for an efficient operation [1,2]. Several considerations for supersonic inlet design may be listed as follows:

- Capturing the sufficient volume of air required by the engine
- Providing low total pressure loss by efficiently compressing the airflow
- Having low external drag
- Operating over the designed range of Mach numbers and angles of attack
- Having a good starting and stability characteristics
- Producing uniform subsonic flow field after the shock system
- Having a small, simple and lightweight design

1.2.1 Subsonic Inlets

This type of inlets is known as pitot intakes and they are widely used for aircraft flying less than speed of sound like airliners. Subsonic inlets generally have a quasi-circular cross-section. As shown in Figure 1.1, different streamline patterns form according to operation speed.

Due to the flight velocity and the mass flow requirement of the engine, various operation conditions occur [1]. At *static operation* (Figure 1.1a), air around the inlet entrance is accelerated into the engine owing to the lack of required air mass flow. *Low-speed operation* (Figure 1.1b) shows the desired flight condition. At *high-speed*

operation (Figure 1.1c), captured streamtube diminishes due to the excess air than the engine needs.

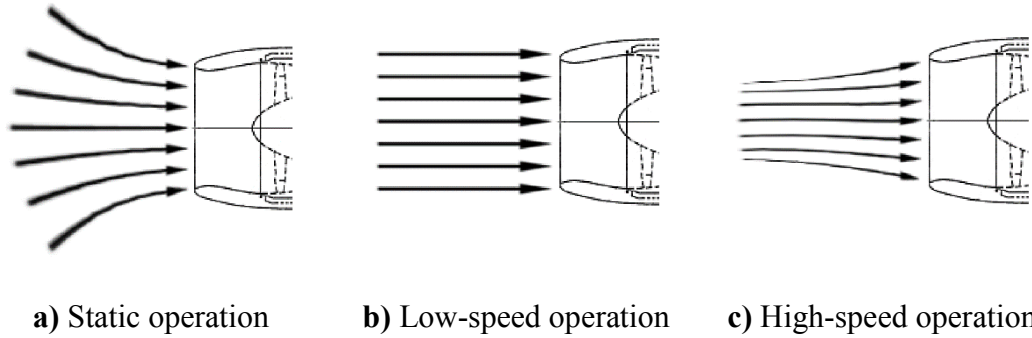


Figure 1.1 : Typical oncoming flow patterns for subsonic inlets.

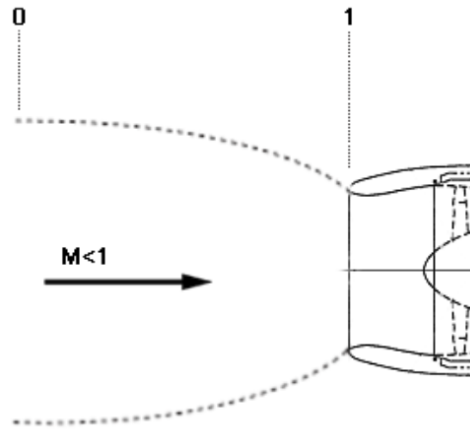


Figure 1.2 : Schematic diagram of captured streamtube by inlet.

If quasi-one-dimensional approach is applied to a simple inlet shown in Figure 1.2, the relation between the ratio of captured streamtube area to inlet entrance area and the freestream Mach number is given in Equation (1.1) [3].

$$\left(\frac{A_0}{A_1}\right)_{max} = \frac{M_1}{M_0} \left[\frac{1 + \frac{\gamma-1}{2} M_0^2}{1 + \frac{\gamma-1}{2} M_1^2} \right]^{\frac{\gamma+1}{2(\gamma-1)}} = \frac{1}{M_0} \left[\frac{2}{\gamma+1} \left(1 + \frac{\gamma-1}{2} M_0^2 \right) \right]^{\frac{\gamma+1}{2(\gamma-1)}} \quad (1.1)$$

The Mach number at station 1 of the inlet has been set to $M_1 = 1$ which corresponds to the maximum mass flow condition. For air, where $\gamma = 1.4$, the maximum mass flow passed by the inlet can be examined in Figure 1.3. It is easily observed that as the flight Mach number increases, the captured streamtube area decreases. Here the main concern is the inlet lip design. A normal shock wave may arise above the outer surface of the lip, which leads to boundary layer separation and increases the drag, when the

cruise speed is about Mach 0.8 which can correspond to the critical Mach number for the lip having a large radius. Moreover, at take-off and climb, where the cruise speeds are low, high mass flow is required to produce high thrust. Therefore, flow separation at the lip should be taken into account carefully due to the angle-of-attack and cross-flow winds.

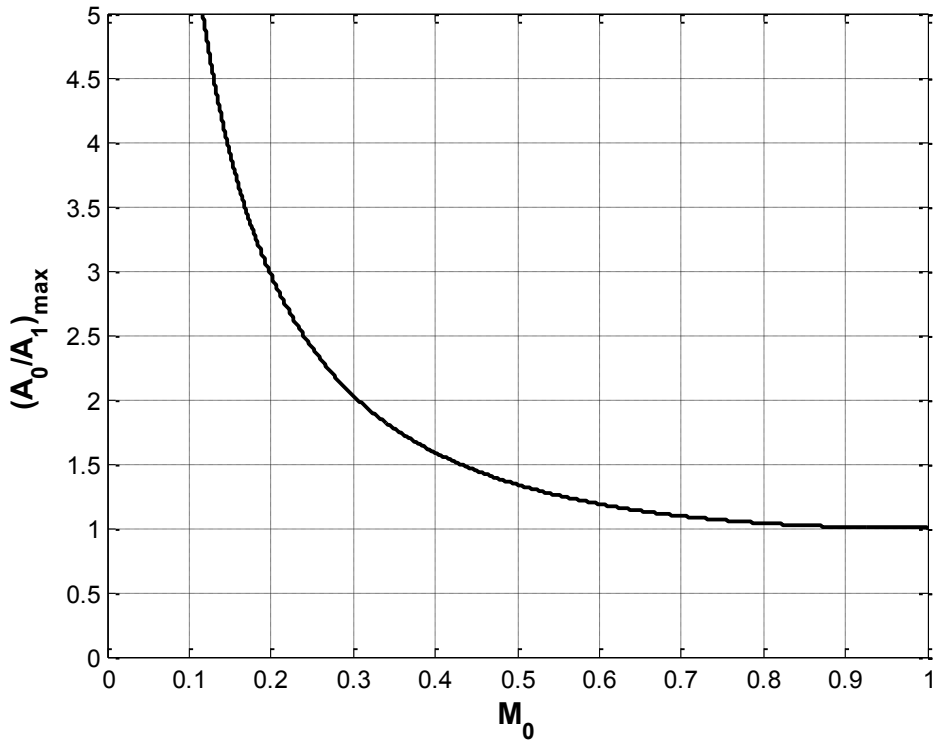


Figure 1.3 : Maximum mass flow passed by the inlet.

Lip radius is the most critical parameter for subsonic inlets [3]. Detailed schematic view of lip radius at two different Mach numbers is shown in Figure 1.4.

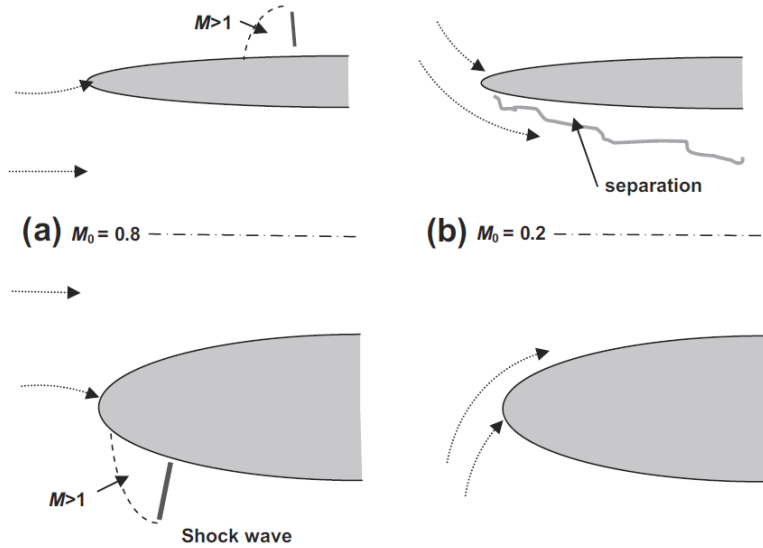


Figure 1.4 : Flow structure around small and large lip radius [3].

At Mach numbers around 0.8, flow velocity becomes supersonic at some region outside the lip and by a normal shock it is decelerated to subsonic speeds. Large lip radii reduce the critical Mach number and extend the supersonic region where the normal shock wave causes boundary layer separation leading to a surge in drag. Therefore, small lip radius is more efficient around these speeds from the point of drag considerations. On the other hand, since high thrust is required at low speeds such as take-off and climb, captured streamtube is large. Thus, the flow encounters a large turn in order to enter the inlet and consequently separation at the lip arises for small lip radii, which decreases the mass flow entering the inlet. In addition, angle-of-attack and cross-flow winds can aggravate the separation. From this point of view, large lip radius is better for low cruise speeds.

1.2.2 Supersonic Inlets

Supersonic inlets can be classified mainly under three different types that are internal compression inlets, external compression inlets and mixed compression inlets. Further details about types of supersonic inlets and their operating conditions are presented in the following sections.

1.2.2.1 Internal Compression Inlets

One of the concerns of internal supersonic compression is the flow starting problem [3,4]. The stages of a quasi-one-dimensional flow through duct are illustrated in Figure 1.5(a) to (f). When the freestream Mach number is less than the starting Mach number, a bow shock is observed and the captured streamtube is smaller than the inlet entrance area (Figure 1.5a). At the starting Mach number condition, the shock is attached at the lip of the inlet (Figure 1.5b). As decreasing the back pressure by increasing the exit area, the shock is swallowed through the throat to a stabilized position (Figure 1.5c). Then, by increasing the back pressure gradually, the shock settles to the throat (Figure 1.5d). For the case where the $M_t = 1$ with the detached shock, further increase of the exit area makes no change for the upstream if the duct chokes at the throat (Figure 1.5e). By continuing to increase the exit area, a second shock forms at the downstream of the throat (Figure 1.5f). Also, this condition is called as to be “unstarted” [4].

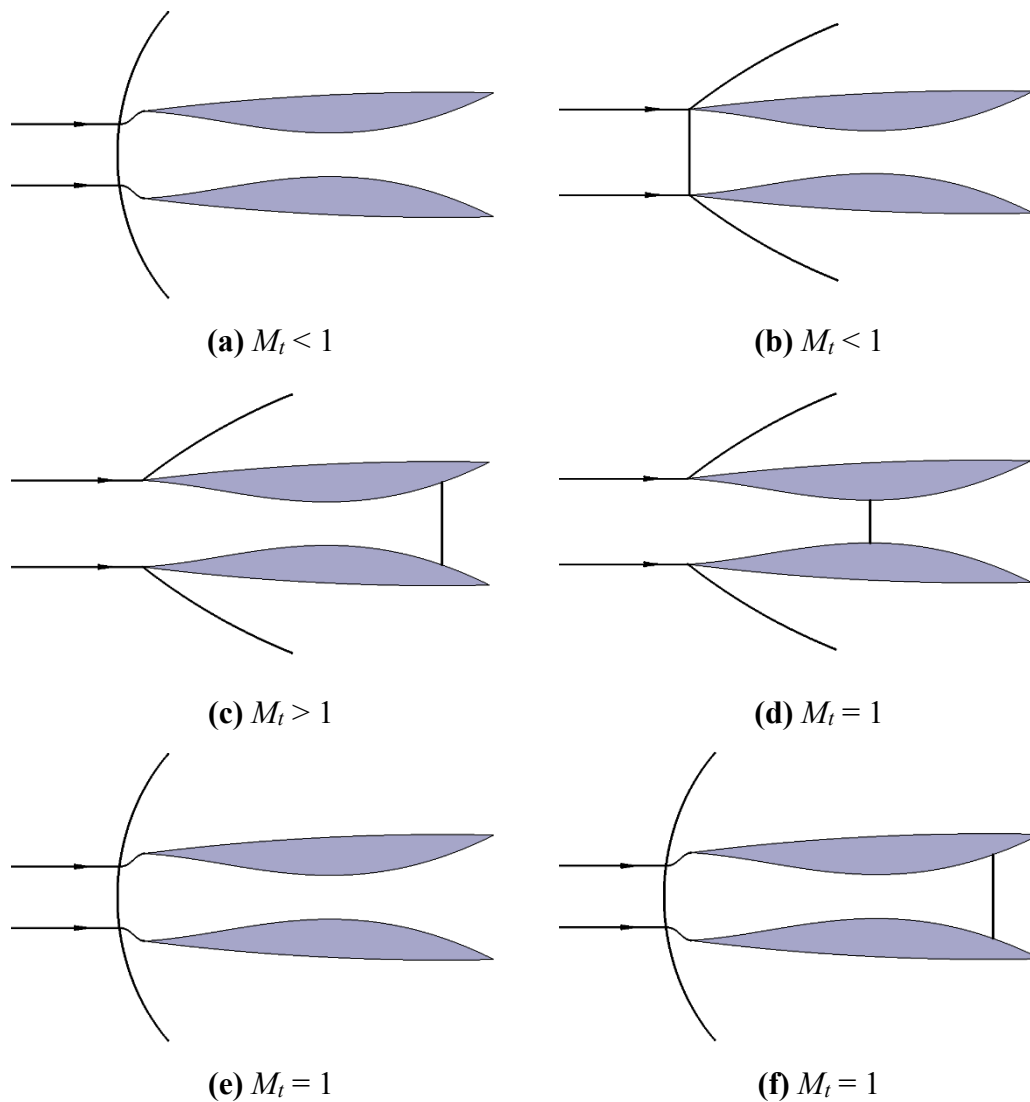


Figure 1.5 : Flow through duct with internal throat.

Various conditions for an internal compression inlet are illustrated in Figure 1.6. A terminal normal shock wave settles at the downstream of the throat after a series of internal oblique shock waves enabling the compression of the oncoming air. At starting, in order to swallow the normal shock, variable throat area is required for this type of inlets [1]. In addition, related to the changing flight velocities and the engine condition, fast reaction bypass doors are needed for the correct positioning of the normal shock. Through the normal operation, if the flight Mach number is reduced or the back pressure is increased, the flow pattern inside the inlet is totally corrupted and it leads to inlet unstart. In this case, since the captured streamtube is diminished, mass flow passing through the inlet reduces, low total pressure ratio is induced, high spillage drag occurs and engine flameout may arise.

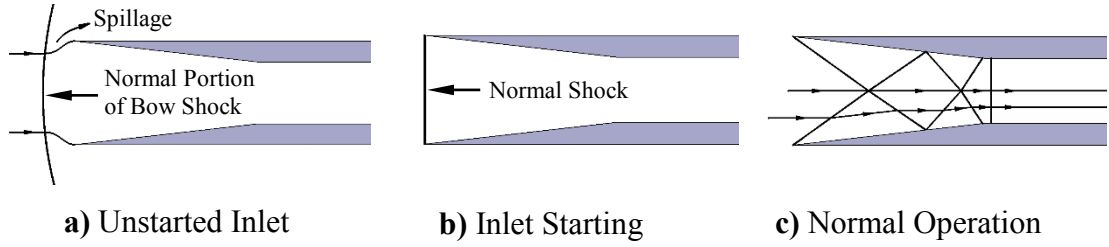


Figure 1.6 : Shock wave positions in the internal compression inlet.

Starting of this type of inlet requires sufficiently large throat area [1]. Figure 1.7 shows the ratio of the throat area required to start the inlet (A_{ts}) to the throat area required at normal operation (A_{tr} , where $M_t = 1.2$). The expression by using basic one-dimensional flow is stated in Equation (1.2), where $(P_{02}/P_{01})_{M_0}$ is the total pressure ratio across a normal shock (subscripts 1 and 2 represent the upstream and the downstream of the shock, respectively) with upstream Mach number (M_0). As it can be observed from Figure 1.7, Mach numbers greater than 2 require extremely large throat area variation to start the inlet which is mechanically not suitable for a variable throat geometry.

$$\frac{A_{ts}}{A_{tr}} = \frac{1}{\left(\frac{A}{A^*}\right)_{M_t} \left(\frac{P_{02}}{P_{01}}\right)_{M_0}} = \frac{1}{1.0304 \left(\frac{P_{02}}{P_{01}}\right)_{M_0}} \quad (1.2)$$

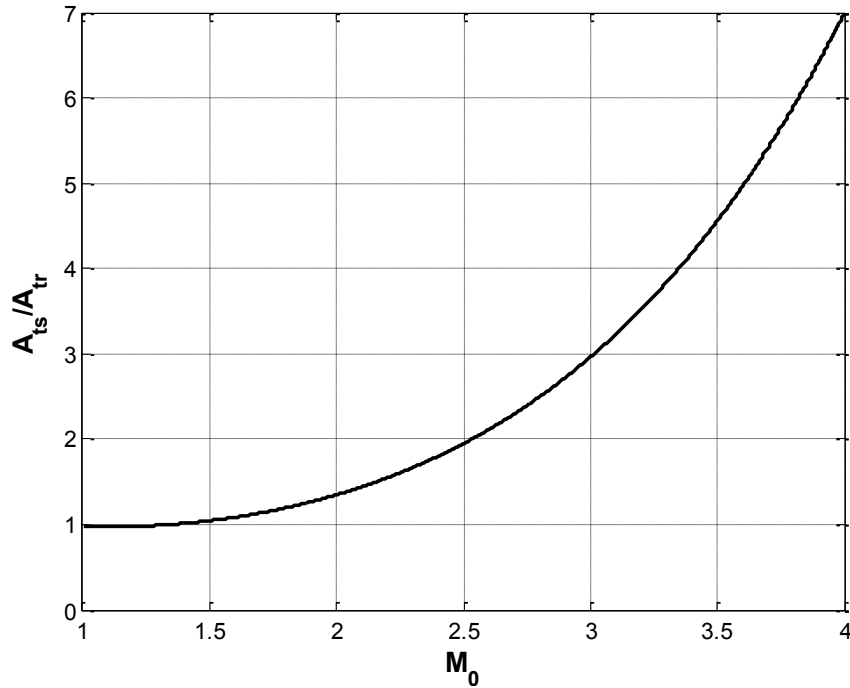


Figure 1.7 : Required throat area variation of an internal compression inlet.

If ideal quasi-one-dimensional internal compression inlet is considered, area relationships can be examined as illustrated in Figure 1.8. Under the assumption of no viscous boundary layer losses, the area ratio of captured streamtube to throat can be defined from Equation (1.3) for a simple fixed-geometry inlet [1].

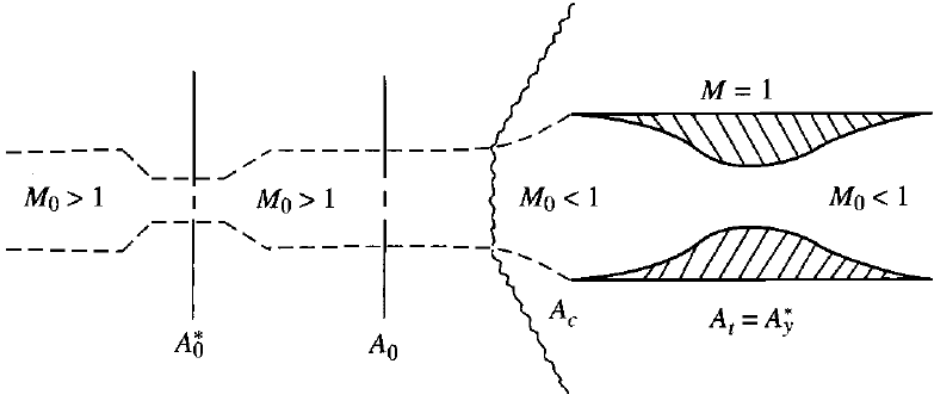


Figure 1.8 : Area relationships of an internal compression inlet [1].

The curve of captured/throat area ratio is plotted in Figure 1.9. In order to ensure the required mass flow passing through the inlet, area ratio should be less than that of the designed operating condition. Otherwise, any small perturbation on the back pressure can push the shocks out of the inlet and this unstable condition can cause inlet unstart.

$$\frac{A_0}{A_t} = \left[\left(\frac{A}{A^*} \right) \frac{P_{02}}{P_{01}} \right]_{M_0} \tag{1.3}$$

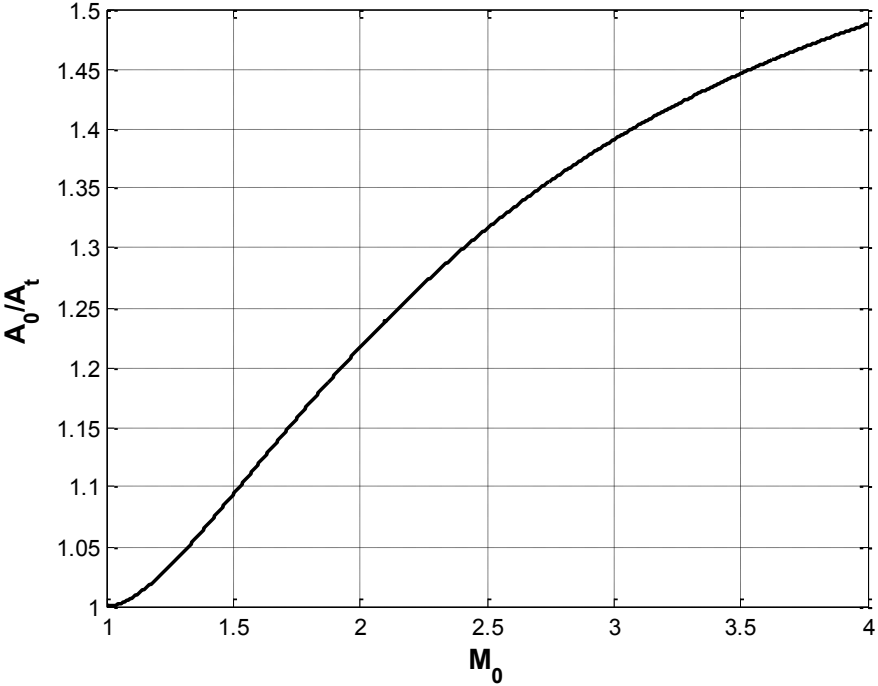


Figure 1.9 : Captured area to throat area ratio of an internal compression inlet.

Performance losses at angles of attack, starting problems of the inlet, unstart phenomenon and several other concerns, diverted the attentions of researchers to other types of compression inlets.

1.2.2.2 External Compression Inlets

The idea of external compression inlet is based on the shock structure where the system of oblique shock waves is situated outside the intake duct. Since the total pressure loss of a normal shock is greater than that of oblique shocks, a system of several weak oblique shocks followed by a terminal normal shock at the cowl lip is preferred for the performance of an inlet.

Figure 1.10 illustrates the basic types of external compression inlets. Freestream Mach number is decelerated through oblique shocks and the flow becomes subsonic after passing through the terminating normal shock. Different shock structures provide different compression ratio and the performance of the inlet is determined by means of total pressure ratio which shows us the amount of total pressure recovery or total pressure loss. Due to the changing conditions during flight, variable inlet geometry may be preferred as shown at the bottom side of Figure 1.10. In order to prevent shock-induced separation, boundary layer bleed is required [2]. Isentropic compression is the theoretical optimal corresponding to infinite oblique shocks that enable 100% pressure recovery after ignoring friction losses. Isentropic compression inlet works properly at only its design Mach number.

Total pressure loss through a normal shock is plotted in Figure 1.11. One of the features of this curve demonstrates that the loss is less than 4% up to Mach 1.4 and the second feature of the curve is the well-approximated straight line that gives a loss rate of 4% per 0.1 Mach number above Mach 1.4 [4].

Shock pressure recovery is presented for several shock systems as a function of freestream Mach number in Figure 1.12. Commonly, while equal deflection angles give better results up to about Mach 2, for higher Mach numbers, leading deflection angle should be the smallest and the rest of the deflection angles must increase in order till the last for better pressure recovery [4].

Design criteria of optimum shock systems for axisymmetric inlets may be determined by graphical methods as presented by Connors [6]. Figure 1.13 shows the difference between wedge and cone. For the wedge case while the flow is parallel to the wedge surface and has a constant Mach number behind the oblique shock, the flow for the case of a cone is conical behind the conical shock and Mach number is constant along rays from the apex but varies along a streamline [4]. Conical shock is weaker than the oblique shock created by the wedge for the same apex angle. Therefore, conical system is more efficient even if mostly wedge system is more preferable for engineering ease. Further detail about shock pressure recovery between wedge and cone is indicated by Seddon [4].

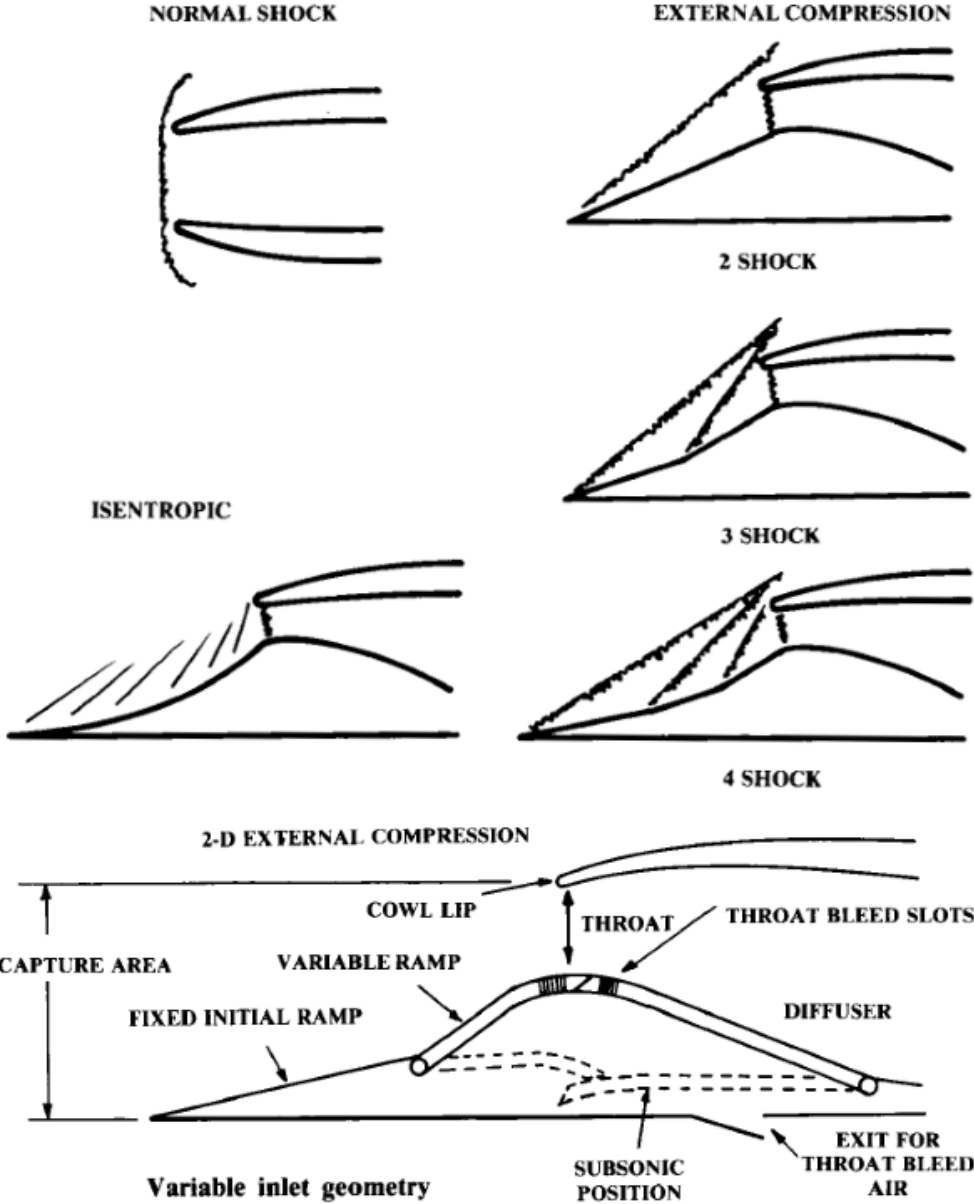


Figure 1.10 : External compression inlet types [2].

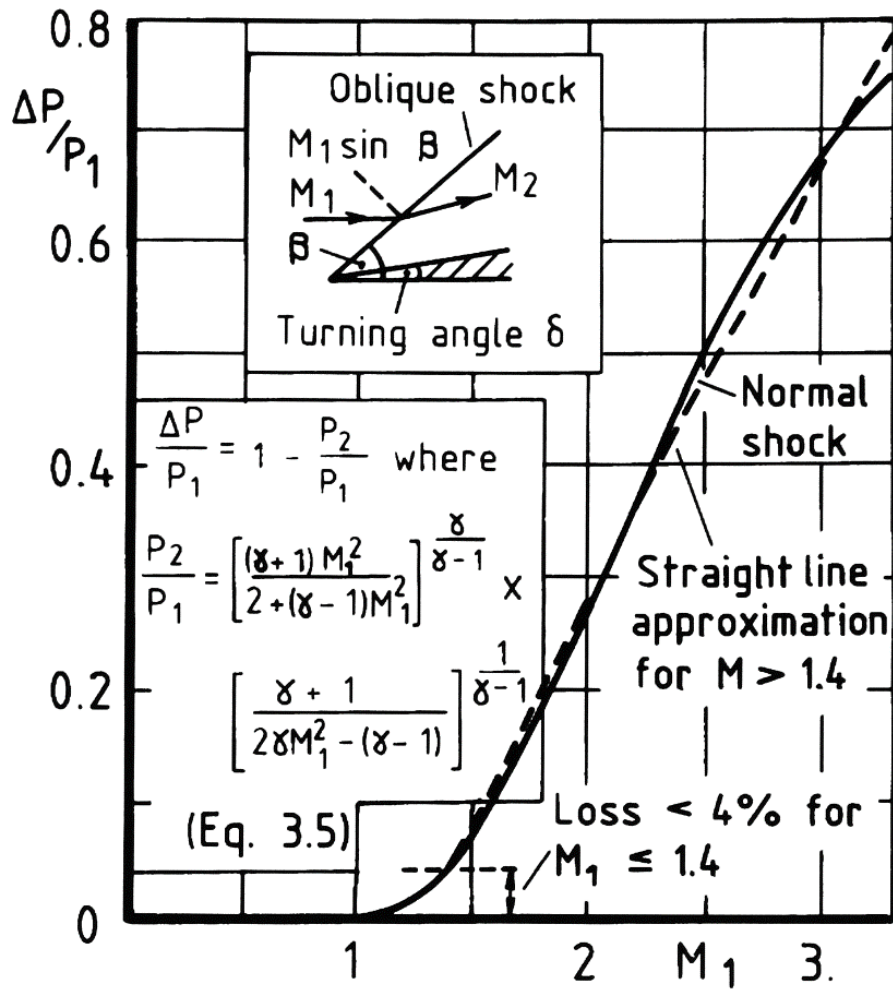


Figure 1.11 : Character of normal shock loss [4].

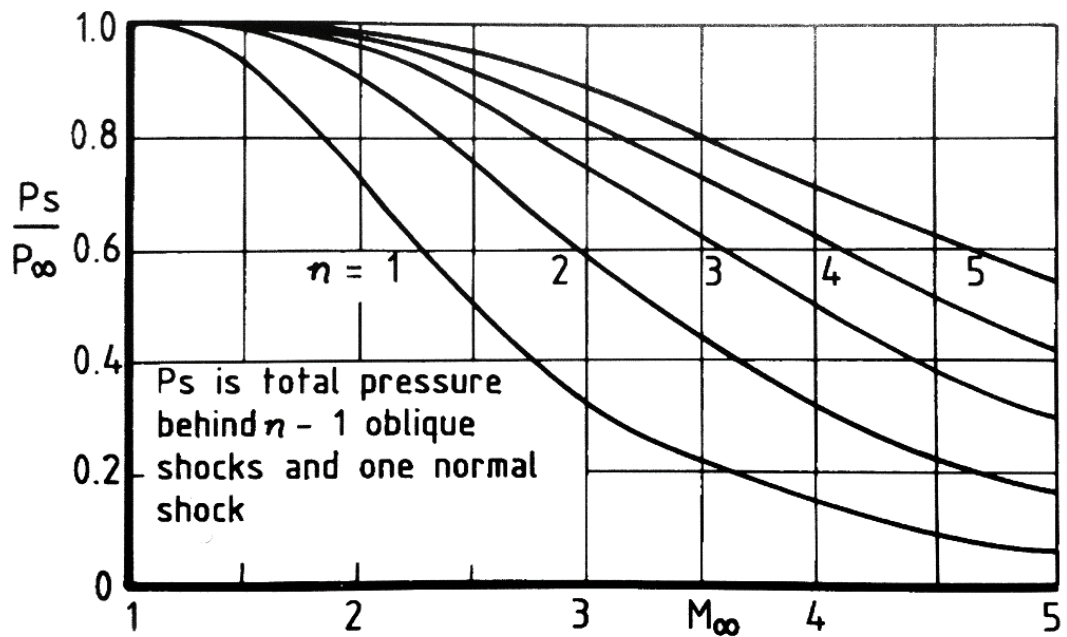


Figure 1.12 : Shock pressure recovery for two-dimensional shocks [4].

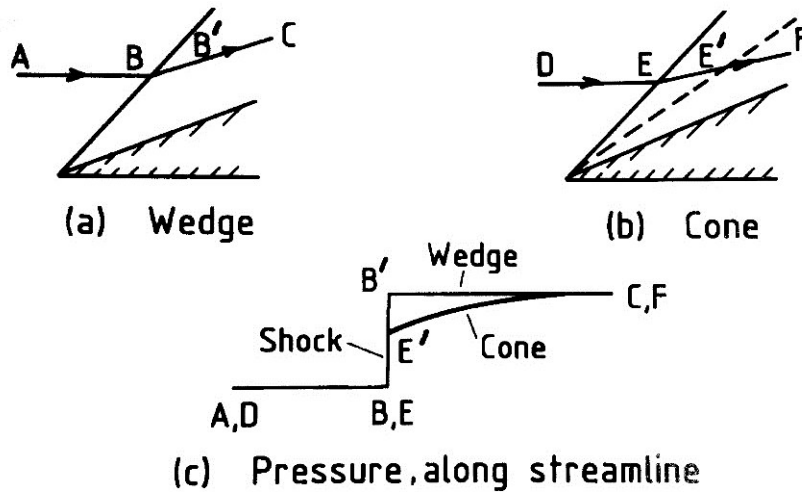


Figure 1.13 : Difference between wedge and cone flows [4].

Flight conditions change the shock system structure during operation and sometimes undesired situations may be encountered. Different flow conditions at off-design Mach number are illustrated in Figure 1.14. At subcritical condition, the drawbacks are high spillage drag and the possibility of buzz occurrence [4]. At supercritical condition, inlet operates at lower total pressure recovery. Here the disadvantages are high thrust-loss and flow maldistribution which may cause engine surge. In addition, for internal compression inlets, subcritical operation leads to the discharge of internal shocks. Remarkable drop in total pressure recovery and flow starting problem should be considered deeply for off-design conditions.

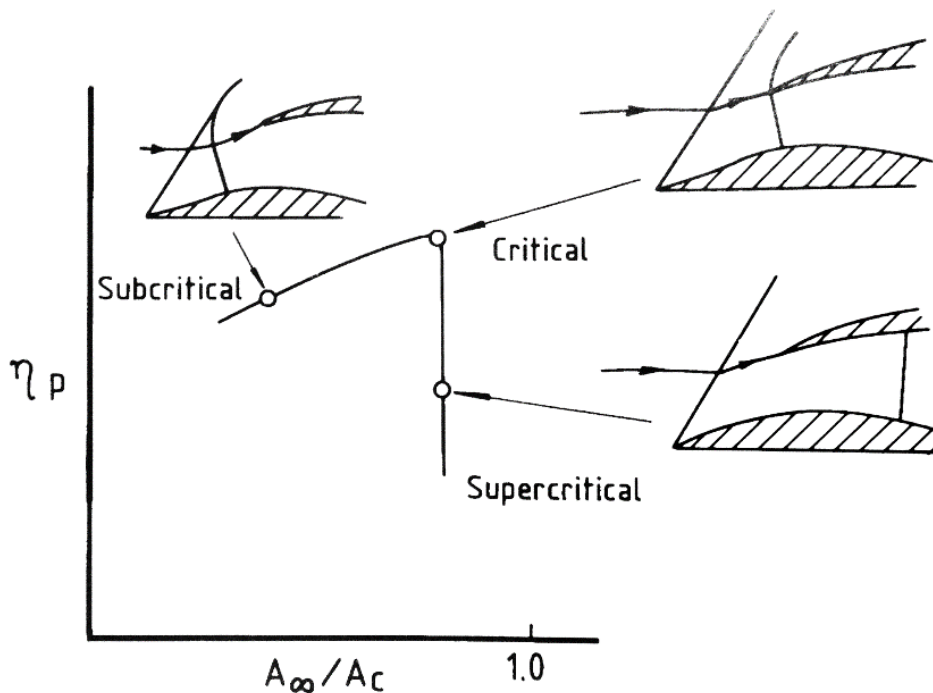
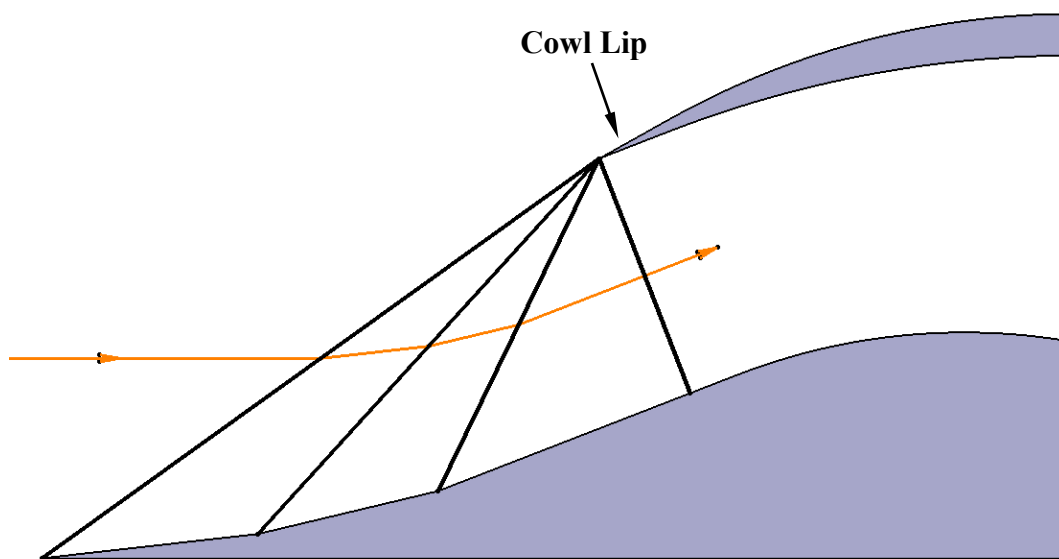


Figure 1.14 : Different flow conditions at Mach number below design [4].

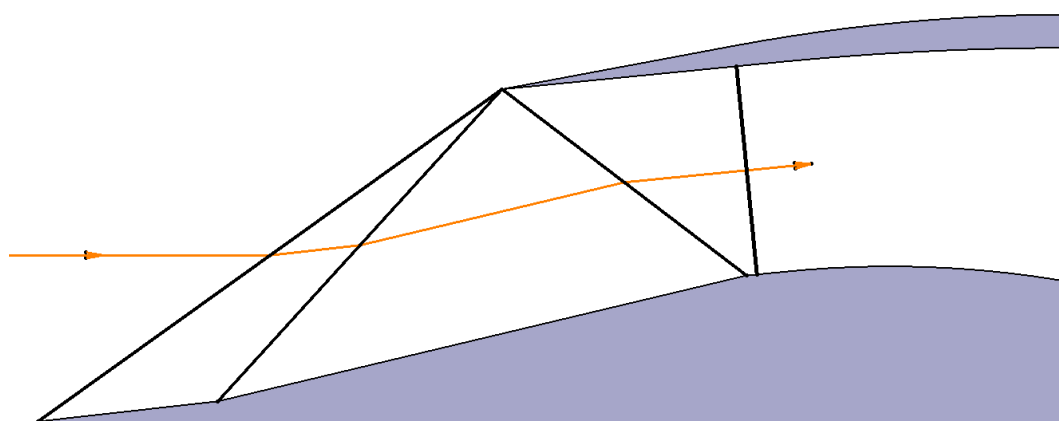
1.2.2.3 Mixed Compression Inlets

Mixed compression inlets have a combination of both external and internal compression shock structure. The main purpose of this type is to reduce the cowl drag. Figure 1.15a illustrates a four-shock external compression inlet designed for Mach 2. Further details about the calculations of angles and other parameters are presented in Chapter 3. The ramp angles consist of 6.4, 7.0 and 7.8 degrees starting from the most upstream location. Therefore, the total deflection angle of the freestream flow is $6.4^\circ + 7.0^\circ + 7.8^\circ = 21.2^\circ$. As a result, the cowl lip should have an angle at least slightly more than 21.2° . If Figure 1.15b is examined closely, two external shocks are followed by two internal shocks. The total turn angle of this case is $6.4^\circ + 7.0^\circ - 7.8^\circ = 5.6^\circ$. Thus, this lower deflection angle leads to a smaller cowl lip angle enabling lower cowl drag. Another example of mixed compression inlet is shown in Figure 1.15c where the total turn angle is $6.4^\circ - 7.0^\circ - 7.8^\circ = -8.4^\circ$.

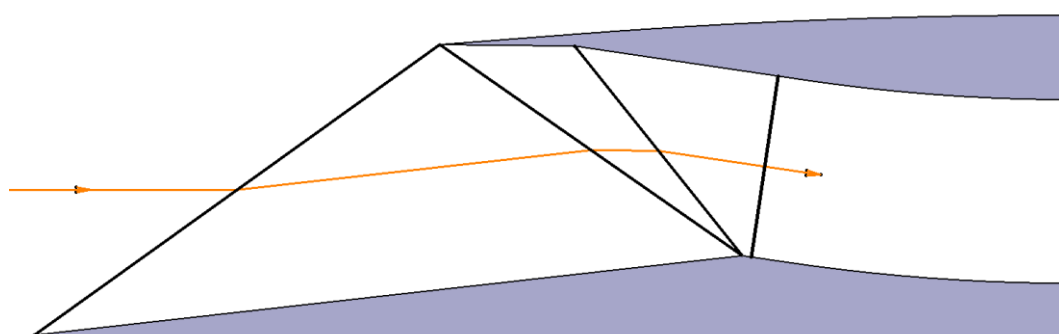
Since compression ramps enable the same sequence of Mach numbers, the shock pressure recovery is the same in all three cases. Moreover, while the shortest possible inlet (defined from the most upstream position to the normal shock location) is 4 shock external compression inlet, the longest one is 25/75 external/internal mixed compression inlet. If boundary layer effects are taken into account, 25/75 mixed compression inlet is expected to have more loss on pressure recovery than 50/50 mixed compression inlet.



a) 4 shock external compression inlet with shocks focused on cowl lip



b) 50/50 mixed compression inlet with external shocks focused on cowl lip



c) 25/75 mixed compression inlet with internal shocks focused at shoulder

Figure 1.15 : 4 shock inlets types designed for Mach 2.

1.2.3 Flow Control Mechanism

In order to achieve desired flow structure for different cruise conditions and inlet starting, area ratio must be adjusted properly. Figure 1.16 illustrates the variable inlet geometry of F-14 Tomcat fighter aircraft [7].

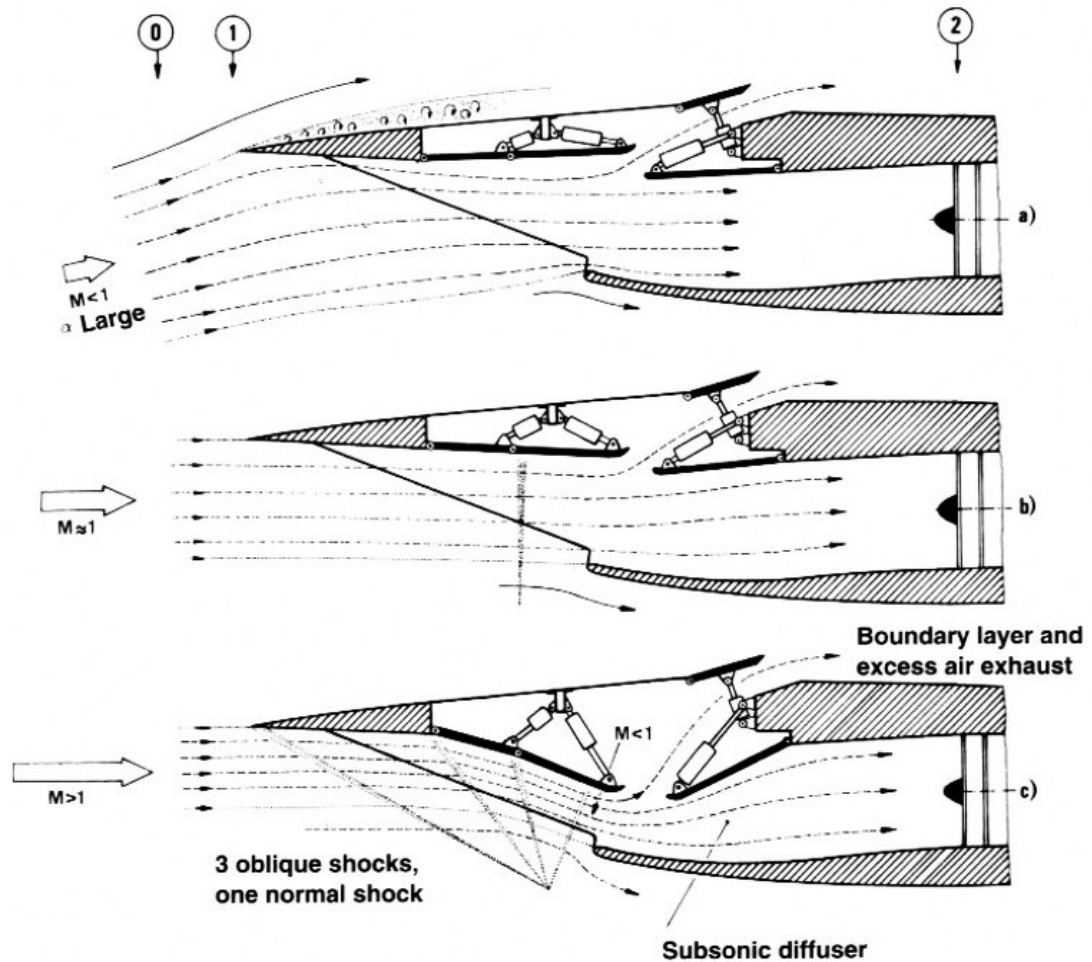


Figure 1.16 : F-14 inlet characteristics [7].

For the case of subsonic flow at high angle-of-attack (Figure 1.16a), throat area is widened to increase the mass flow. In supersonic flow, moving ramps provide the inlet act as a four-shock external compression inlet (Figure 1.16c). Variable ramps control the position of shocks. Moreover, the bleed door on the top of the inlet enables boundary layer bleeding to prevent engine “buzz”.

Buzz is defined as low-frequency and high-amplitude pressure oscillation which is related to SBLI or shock-shock interaction at low mass flow ratios. Trapier et al. presented an experimental study of supersonic inlet buzz in a mixed compression rectangular inlet model with/without bleed at Mach numbers ranging from 1.8 to 3 [8].

Gefroh et al. investigated the effect of aeroelastic mesoflaps in order to control SBLIs through passive cavity recirculation by achieving appropriate mass bleed or injection under gas dynamic pressure loading [9]. Moreover, Srinivasan et al. studied passive methods of controlling SBLI at Mach 1.42 such as conventional porous plate, microporous plate, streamwise slots, conventional mesoflap array and hybrid flap array [10]. Since boundary layer bleed causes the loss of captured mass flow and the additional drag increase, vortex generators are another type of flow control method for SBLIs. They generate a tip vortex which energize the near-wall flowfield and experiments present the ability of postponing the boundary layer separation due to the SBLI [11–16]. Today, numerous studies still continue to have a better understanding and to establish robust control systems over SBLIs.

2. EXPERIMENTAL SETUP

2.1 Wind Tunnel

Experiments were performed in the supersonic wind tunnel in the Trisonic Research Laboratory at the Faculty of Aeronautics and Astronautics of Istanbul Technical University. This supersonic wind tunnel has a test section size of 15×15 cm and can operate at Mach number ranges of 0.4 – 2.2 and 2.4 – 4.0 by using two different test-section / nozzle-block modules. However, since the lower Mach number test section had relatively larger glass side walls for imaging, and the test section floor was already modified for mounting inlet-type models, the test section with the Mach number range 0.4 – 2.2 was used in the experiments. A schematic of the portion of the wind tunnel facility that shows the compressors and tanks is shown in Figure 2.1 with components numbered as:

1. **10-Bar Compressor:** This is the starting point of the system. Air is first compressed to about 10 bars and delivered to the next station by pipes as shown in blue in Figure 2.1.
2. **10-Bar Pressure Tank:** Compressed air is sent to this buffer tank at 10 bars and is passed through a filter at the exit of the tank.
3. **Gas Dryer:** Gas dryer provides first step in decreasing the humidity of the compressed air.
4. **40-Bar Compressor:** This screw-type compressor receives the compressed air at 10 bars and compresses it up to 40 bars. High pressure air is delivered to the next station by pipes as shown in red in Figure 2.1.
5. **Cooler:** Because of the compression process, the temperature of the compressed air increases very much. Since the working range of the chemical dryer at the next station is between -10 °C and 60 °C, the cooler is used to drop the temperature of the air. It

has a simple radiator mechanism with a fan cooling the air as it passes through capillary tubes.

6. Filter: Compressed and cooled air passes through a filter by which small particles, water and oil are held.

7. Chemical (Adsorption) Dryer: Chemical dryer, which is the type 0260-1200 from Donaldson Ultrafilter Company, has two cylinders placed vertically, which operate in order. While one of the cylinders is active and drying the air, the other is put in regeneration mode and becomes inactive. The humidity of the air is held by adsorption using suitable chemicals at high pressure. When a certain time period has passed for the operating cylinder it goes into the regeneration phase in which low pressure air is passed through to dry the moist chemicals. When a cylinder goes into the regeneration phase, the pressure in the cylinder is decreased to about atmospheric value, then it is kept at this regeneration state for about 10 minutes until it becomes active while the other cylinder goes into the regeneration phase.

8. High Pressure Tank for Dryer: This tank is used to maintain high pressure around 35 – 40 bars at the exit of the chemical dryer via a check-valve at the exit of the tank.

9. Check-Valve: This valve is adjustable and is set to pass the flow above about 30 bars. This valve is used to keep the pressure in the High Pressure Tank for Dryer at or above 30 bars in order for the chemical dryer to work efficiently.

10 - 11. High-Pressure Tanks: Compressed air is stored up to 40 bars in these long horizontal tanks. Their volumes are 40 m³ each and they are tested at 60 bars by Turkish Lloyd. The diameter and length of the tanks are 2 meters and 15 meters, respectively. Air is supplied to the wind tunnel from these tanks during the experiments.

12. Isolation Valve: Isolation valve is used to deliver the high pressure air to the regulation valve just before the start of the tunnel run and separates the high-pressure air stored in the main tanks from the rest of the system. This valve operates pneumatically using a remote switch in the control room and requires a supply pressure of about 7 bars. At the beginning of the experiment, the isolation valve is opened by the operator. For emergency situations where the air flow in the tunnel circuit must be cut

off immediately or at the ending the experimental process, this valve is closed by the operator remotely. Figure 2.2 shows the rest of the system after the isolation valve (12).

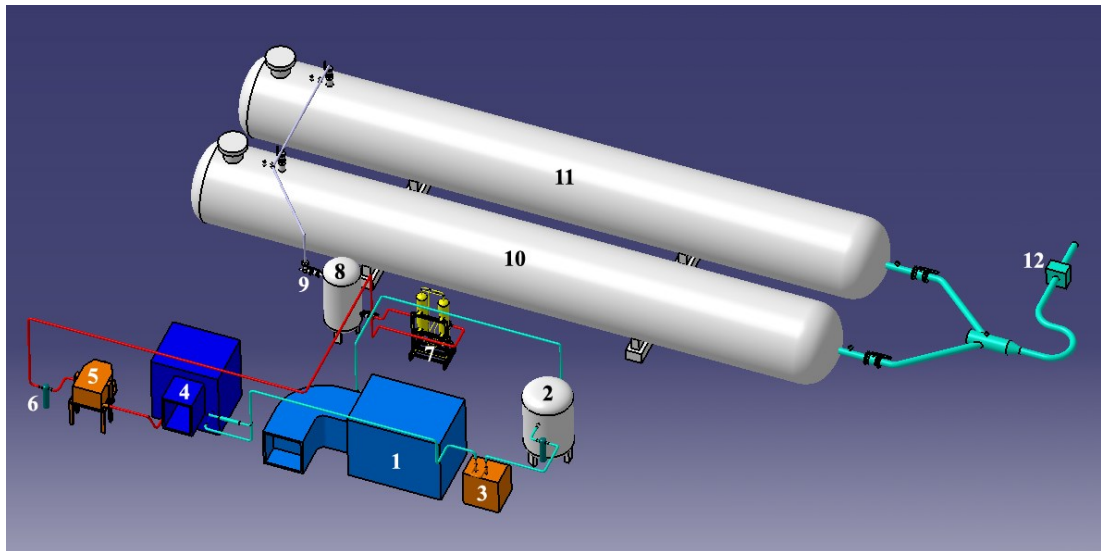


Figure 2.1 : Supersonic wind tunnel compressors and tanks.

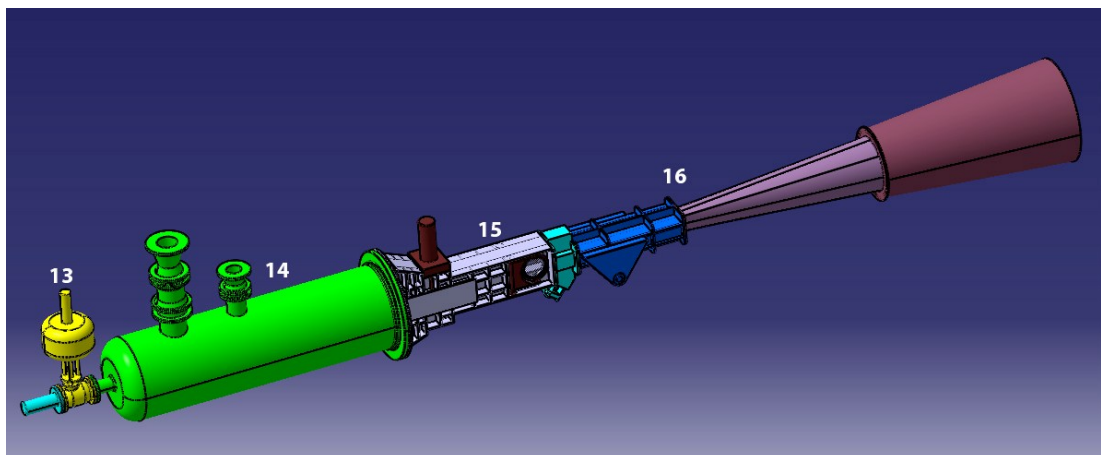


Figure 2.2 : Supersonic wind tunnel test section and other components.

13. Regulation Valve: After opening of the isolation valve, axial control regulation valve starts to operate. Since the exit of the wind tunnel opens to the atmosphere, at the beginning of the experiment, air flow fluctuations occur due to high pressure difference. Regulation valve adjusts the required total pressure in the stagnation chamber. The axial control regulation valve of the Mokveld Company is shown in Figure 2.3 and also it is labeled by 13 in Figure 2.2. It takes about 6 seconds for this valve to be fully opened or to be fully closed. Through a feedback mechanism, a desired stable pressure in the settling chamber is maintained by controlling the valve.

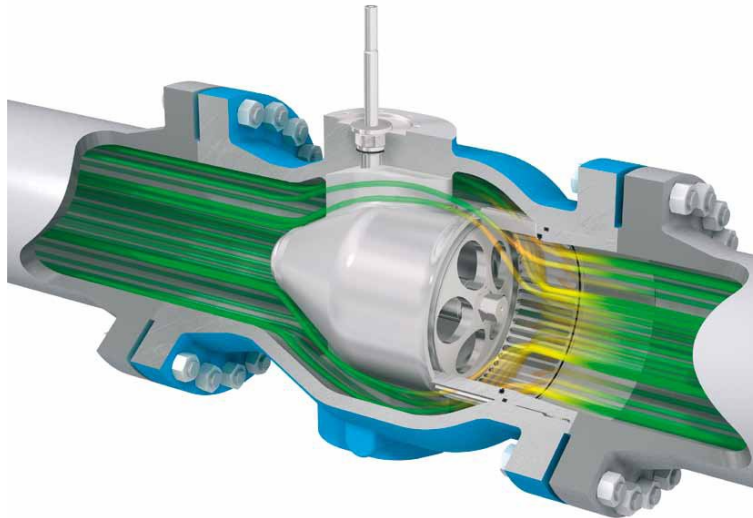


Figure 2.3 : Axial Control Valve from Mokveld Company.

14. Settling Chamber: After regulation valve, air flow goes into the settling chamber. This long settling tank helps reduce fluctuations and turbulence in the air flow and provide uniform and stable initial conditions for the flow in the test section. Settling chamber is the place where the static pressure is the highest at all along the downstream points of the tunnel. Therefore, two nickel membranes are used to burst in case of exceeding the maximum allowable pressure in the settling chamber for safety. These semispherical nickel membranes, shown in Figure 2.4, were designed to burst at different pressures, namely, at 5 bars and 14 bars for Mach 2 and Mach 4 test section modules, respectively. Also, a safety switch equipped with a pressure transducer in the settling chamber is used to close the isolation valve by sending signal to the control computer when the allowable pressure is exceeded.



Figure 2.4 : Nickel membrane.

15. Test Section: Test section of the supersonic wind tunnel is modular and two different test section modules are available for the Trisonic Wind Tunnel. One of these modules is designed for Mach number range 0.4 – 2.2 and the other one is designed

for Mach number range 2.4 – 4.0. For the present experiments, test section for Mach number range 0.4 – 2.2 is used and it has a cross section of 15×15 cm. With the help of an electric motor and a gear mechanism, the throat cross section area can be adjusted for different Mach numbers within its range. In the ideal condition, subsonic air flow, coming from the settling chamber, speeds up to Mach 1 in the converging section of the Converging - Diverging nozzle before the test section. In the diverging section of the C-D nozzle, flow speeds up and the desired Mach number is obtained. For optical methods such as schlieren or shadowgraph imaging, side walls of the test section are equipped with quartz windows as shown in Figure 2.5. A photograph of the designed inlet model assembly for the experiment is also shown in the figure. These quartz windows have great resistance for thermal shocks and have extreme flat surfaces with a homogeneous structure without impurities such as seeds and bubbles inside. A boundary layer suction mechanism which sucks the air flow through the perforated upper and lower walls can also be used in the test section module. However, lower perforated wall was modified to be able to mount the designed inlet model as shown in Figure 2.5 and no boundary layer suction mechanism was used in the lower wall for the experiments.

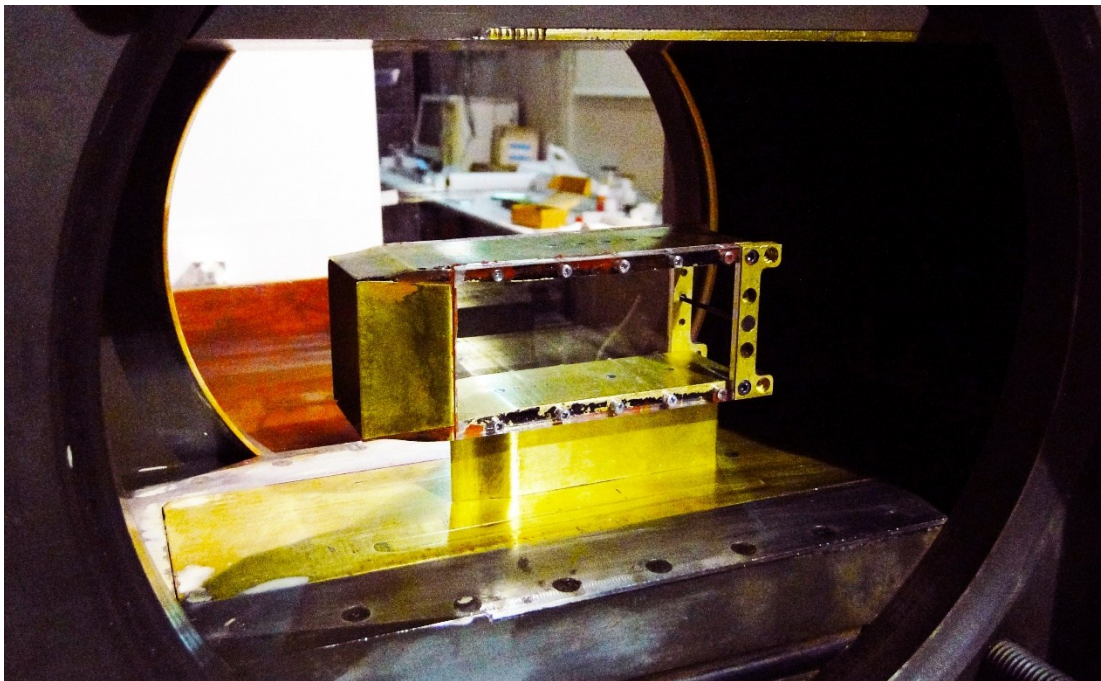


Figure 2.5 : Test section module and the designed inlet model assembly.

16. Diffuser: Air flow enters the diffuser after test section portion of the wind tunnel. In the diffuser, flow decelerates and a weak normal shock forms near the second throat. From this point on flow becomes subsonic. The diffuser numbered by 16 in Figure 2.2,

with its increasing cross section area, slows the flow down further and exhausts to the atmosphere.

Due to the geometry of inlet models, difficulties occur while mounting the inlet models to the test section using the original model mounting support of the wind tunnel. In the supersonic wind tunnel at the Trisonic Research Laboratory of ITU, only a stick-type support was available in the center of the test section along the flow direction as a mounting apparatus. Since this support was not suitable for mounting an inlet model, some modifications were made on the test section module in a previous study [17]. The supersonic wind tunnel had a boundary layer suction mechanism beneath both the upper and the lower walls to reduce the thickness of the boundary layer developing along the test section walls. The one in the bottom wall was removed and a new mounting apparatus was designed as shown in Figure 2.6. The original perforated plate of the boundary layer suction mechanism was replaced with the a stainless steel floor plate with a plug in the middle that enables to be able to mount different inlet models [17].

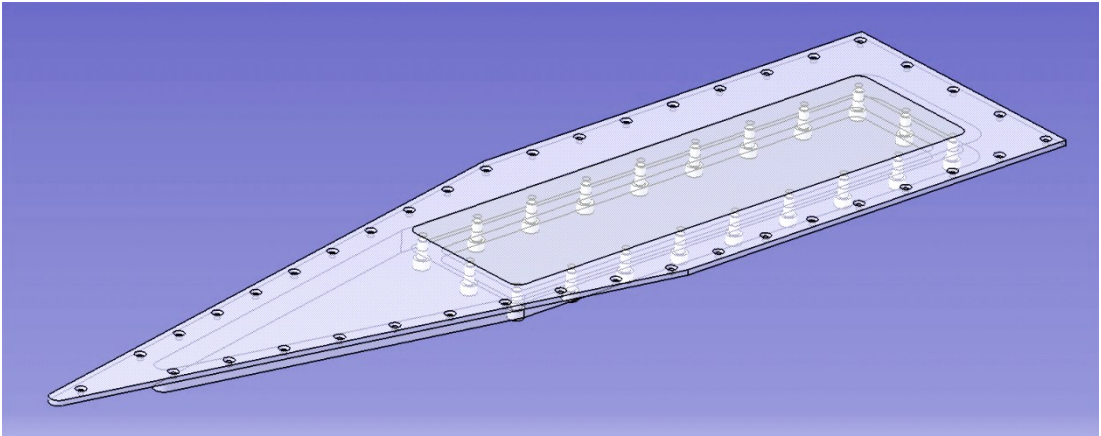


Figure 2.6 : Mounting apparatus.

2.2 Shadowgraph System

The shadowgraph visualization method is based on the second derivative of the gas density. While light rays pass through the test section, the regions where density gradient exists deflect the rays as shown in Figure 2.7 and the resultant deflections illustrate the dark and bright regions on the screen located outside the test section [18]. This method is useful for determining the location of shock waves besides observation of turbulent flow regions.

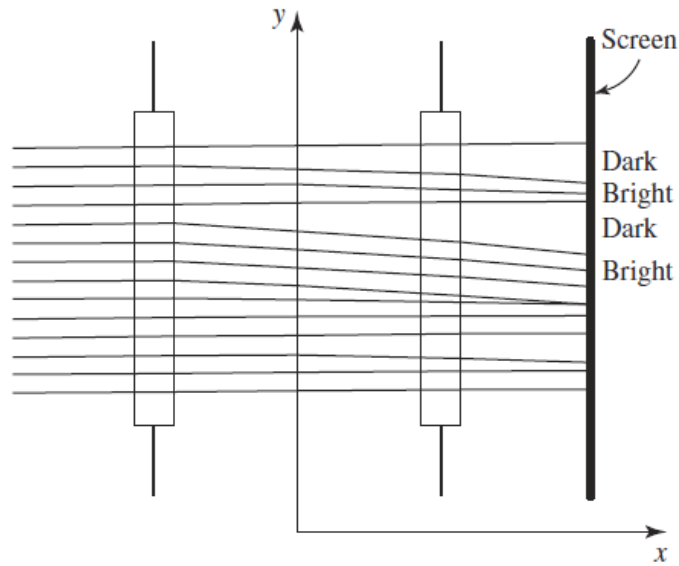


Figure 2.7 : Schematic of shadowgraph system [18].

2.3 Schlieren System

Schlieren system is a visualization technique based on the first derivative of the fluid density. This method indicates the density gradients that occur in compressible flow such as those across the shock waves, shear layers, etc. As shown in the schematics in Figure 2.8, light from a slit source ab is collimated by the lens L_1 and goes through the plane 1 in the test section [18]. After the light passes through the lens L_2 , inverted image of the source at the focal plane 2 is produced. In this focal plane a portion of the light is cut by the knife edge and L_3 lens generates the image of the test section on the screen at plane 3. By the knife edge, contrast is increased which is directly proportional to the density gradient in the flow.

In applications, most schlieren systems use mirrors instead of lenses due to economic reasons. An example of a schlieren system with mirrors is illustrated in Figure 2.9. The light after passing through the slit, goes onto the mirror and reflected toward the test section. The light deflected by the test section goes onto another mirror and reflected again. A knife edge, which is placed in the focal point, blocks some of the image of the light source and the remaining image is sent to a photographic recording device. These systems with mirrors are also used to shorten the total length of the schlieren system.

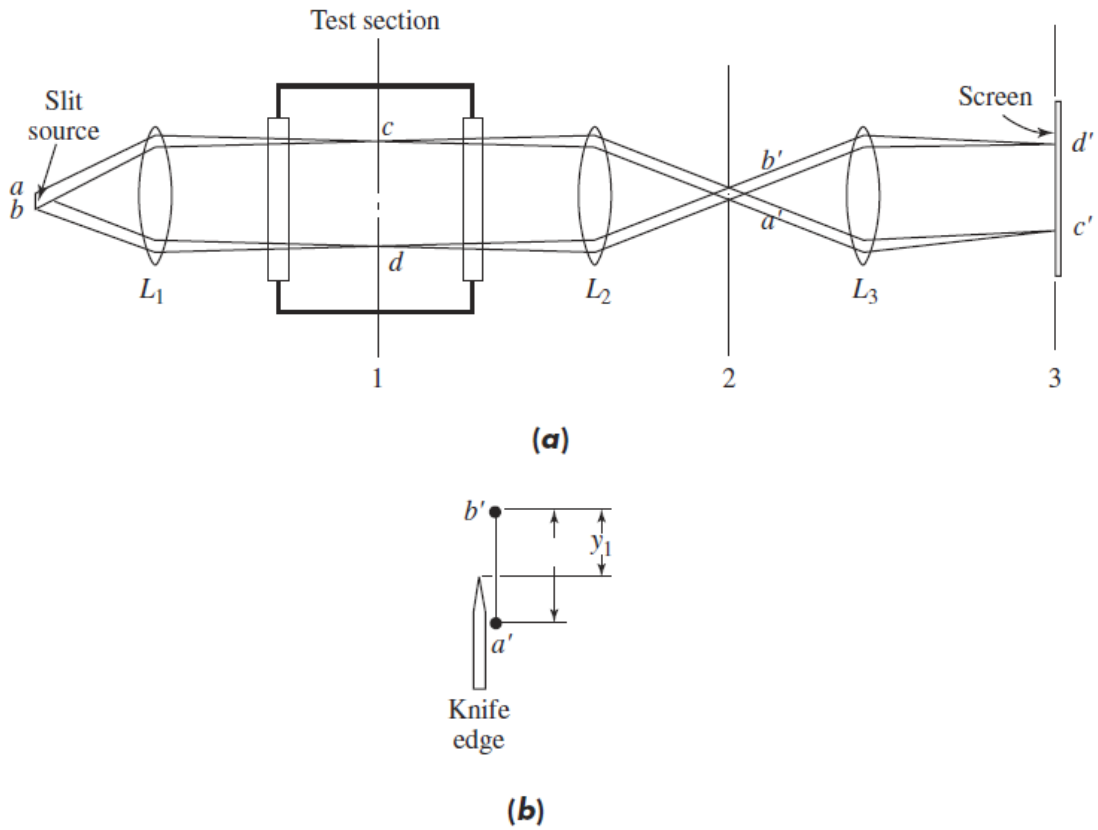


Figure 2.8 : Schematic of a schlieren system [18].

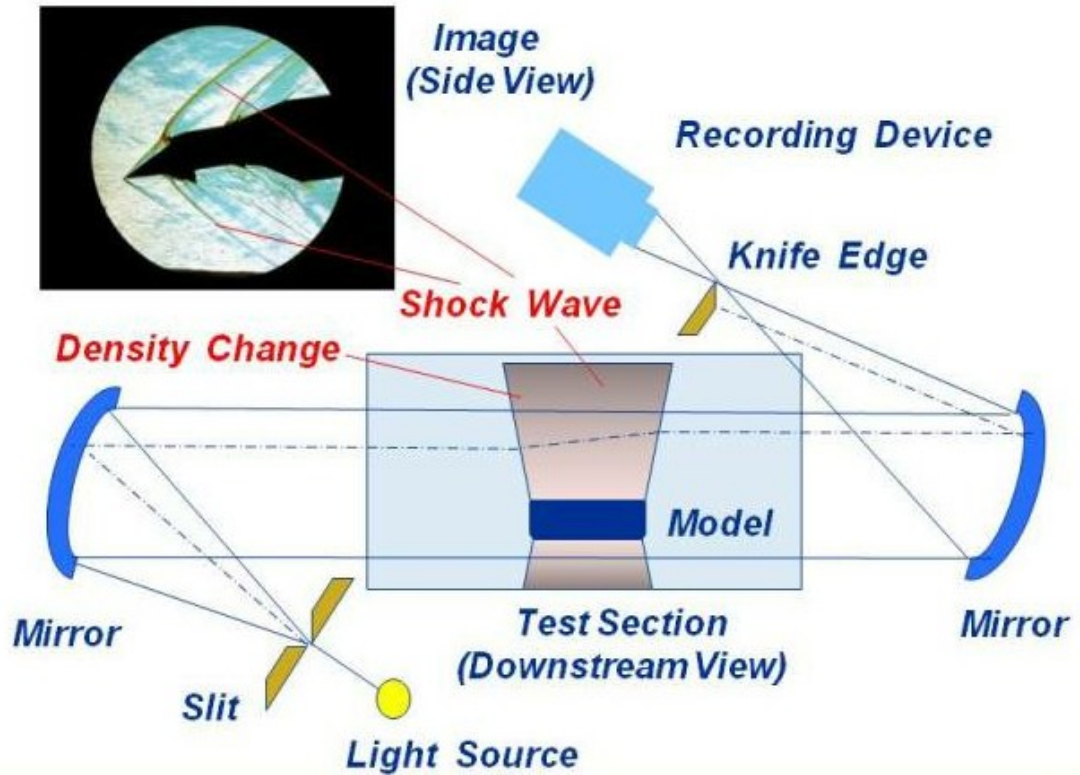


Figure 2.9 : Schlieren system with mirrors [19].

The Schlieren system at the supersonic wind tunnel in the Trisonic Research Laboratory is illustrated as a CAD drawing in Figure 2.10. During experiment, a video camera records the schlieren images of shock waves, which helps understand the behavior of the shock structure better by comparing the image frames and the pressure time history. Furthermore, the system can also be used as shadowgraph by placing a translucent screen back of the test section and recording the video directly from behind the screen.

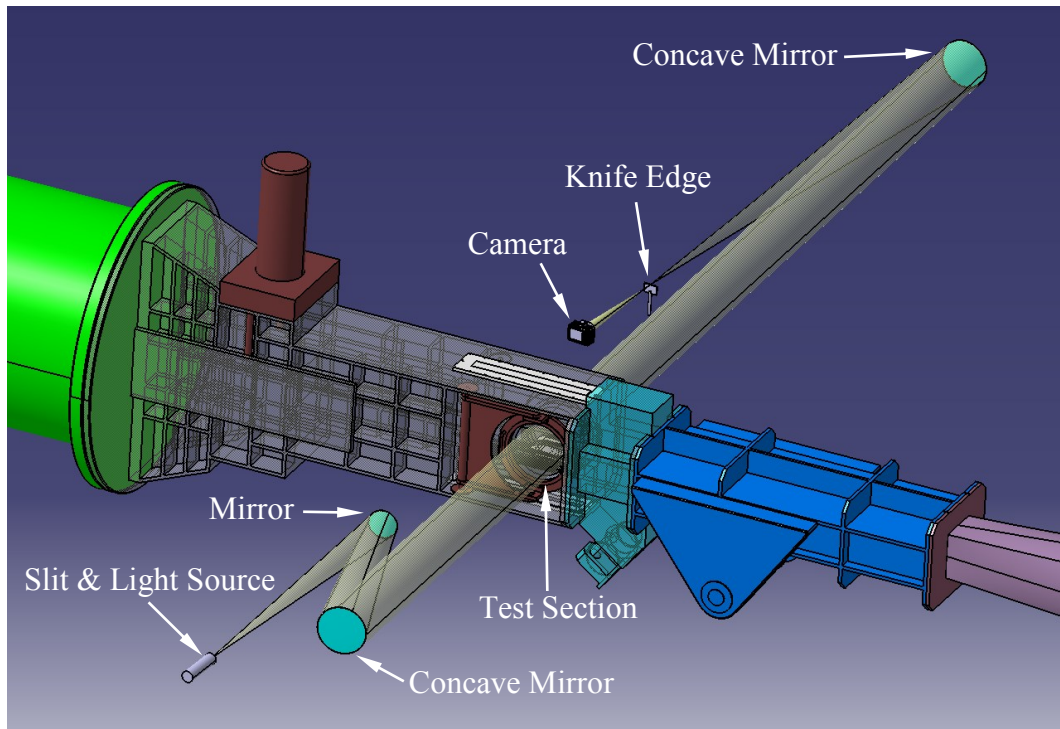


Figure 2.10 : Schlieren system of the supersonic wind tunnel.

2.4 Surface Oil Flow Visualization

Surface oil flow method is generally used to observe the boundary layer separations. A tiny layer of oil is basted at some upstream location and as the air flows over the surface, the oil is carried to downstream forming long strips. In regions where flow separation occurs, the oil accumulates along the separation line due to reverse flow. Thus, separation lines becomes visible. In the experiments, a mixture of liquid paraffin, oleic acid and a fine powder of titanium dioxide was used. Some skill and experience is important during suitably employing the mixture to the surface and making the mixture. After each run, the surface should be wiped clean for the next run. Furthermore, since titanium dioxide is white, to create contrast the surface is painted in black.

2.5 Internal Compression Inlet Model

The model was designed by using the CATIA software. A symmetrical 4° ramp angle was chosen for the internal compression inlet model. Further details about the compressible flow calculations and shock positions are given in the next chapter (see section 3.2.1). Experiments were performed for two different throat heights but since the first model did not satisfy the started flow condition due to the high value of captured area to throat area ratio, a second model was designed by enlarging the throat height. Details related to the dimensions of the upper and lower ramps are illustrated in Figure 2.11 where angles and lengths are given in degrees and millimeters, respectively. Additionally, in order to create a back pressure to push the started shock structure forward and obtain a normal shock after oblique shock reflections inside the inlet, various blocks were manufactured and placed at the exit section of the model in the experiments.

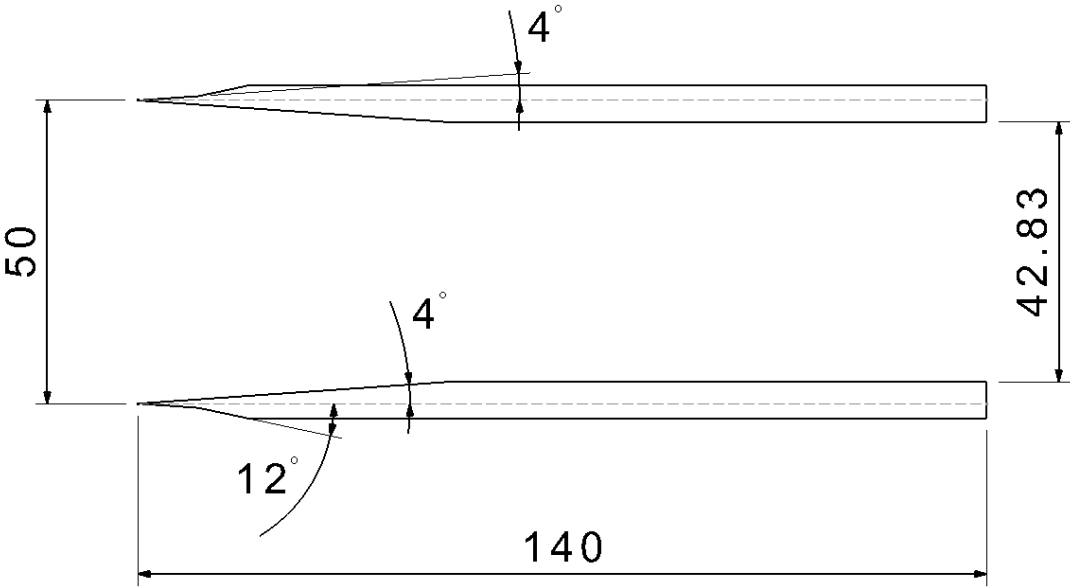


Figure 2.11 : Side view of upper and lower ramps for the 2nd model.

The details of the model assembly and components are shown in Figure 2.12. Acrylic side walls provide optical transparency for shadowgraph flow visualization. For the blocks, two different geometries, pieces with rectangular and cylindrical cross sections, were tested. The rest of the components were manufactured from brass by a CNC machine. Metric bolts and setscrews were used to assemble the model. Moreover, liquid seal were applied between parts during assembling to ensure sealing through the joints. Transducer slots and transducer cables are also illustrated schematically with red lines in Figure 2.12.

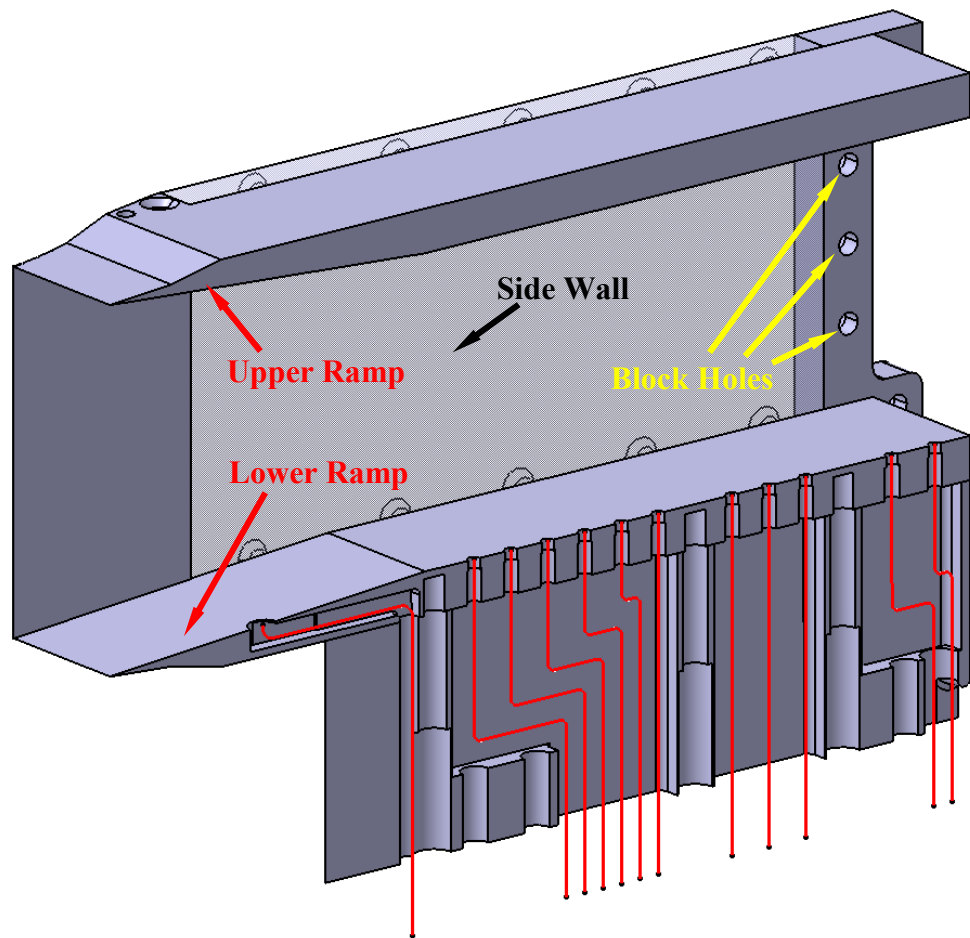
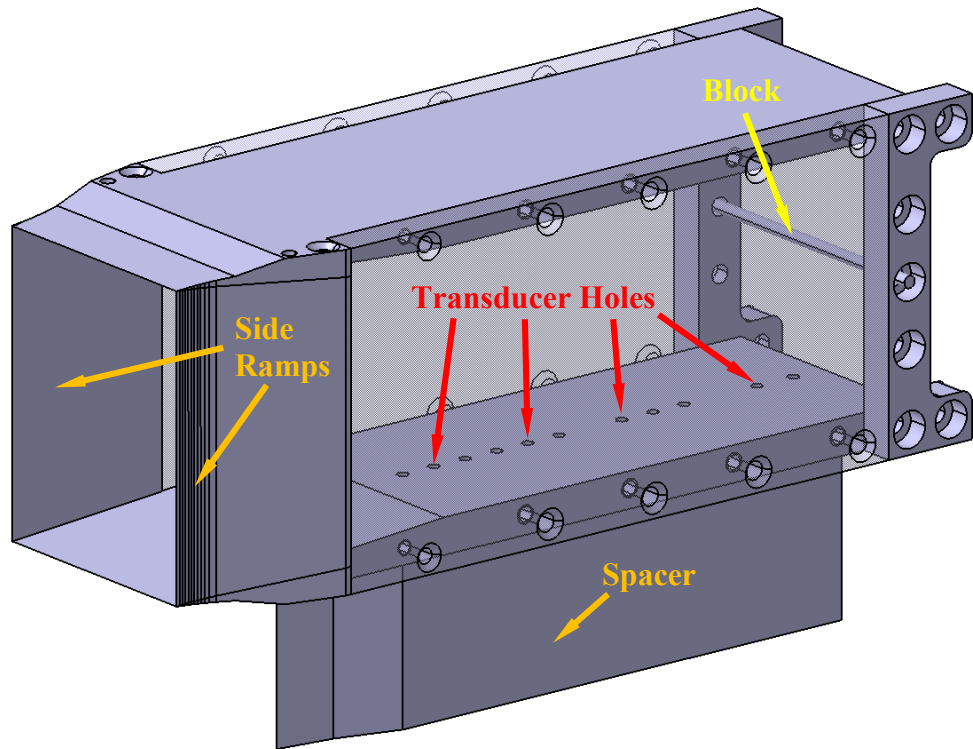


Figure 2.12 : Details of the model assembly and components.

2.6 Pressure Transducers

In the experiments, Kulite pressure transducers, which have good static and dynamic response, were used in surface pressure measurements. The types and dimensions of the transducers are shown in Figure 2.13. Since a limited number of transducers is available, total of six transducers were used in the experiments. Due to the small wall thickness at the foremost location on the lower ramp, only a flat type Kulite was suitable. Blank inserts were used to fill the empty transducer holes.

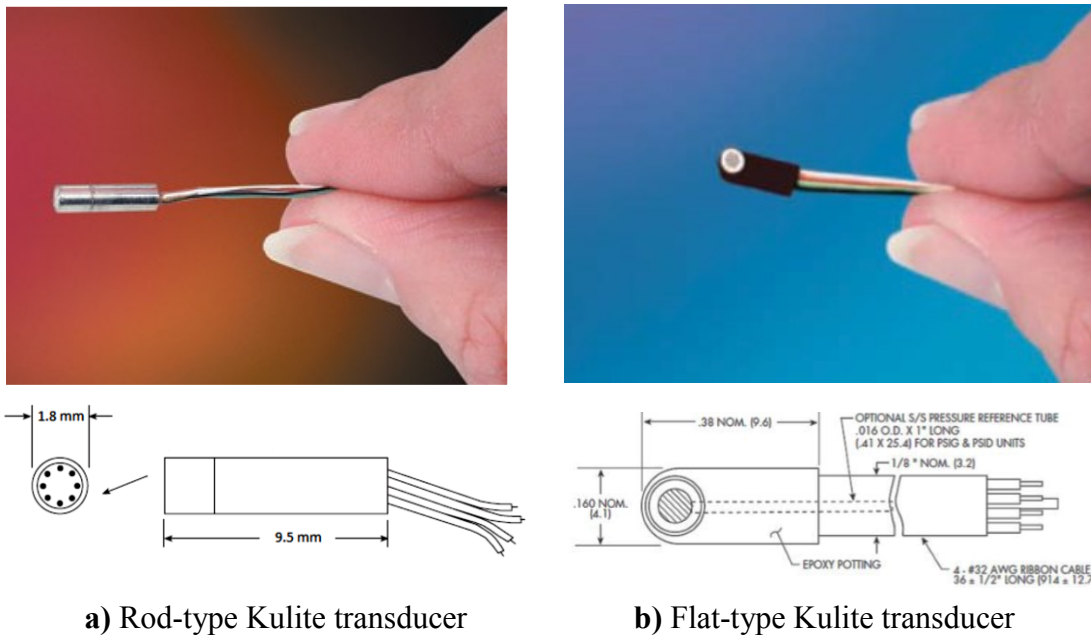


Figure 2.13 : Kulite transducers for pressure measurements.

To be able to place the transducers in the appropriate transducer holes, M3 bolts are drilled properly through its center axis to form sleeves and nail polish is applied as an adhesive to hold the transducer within the sleeve as shown in Figure 2.14.

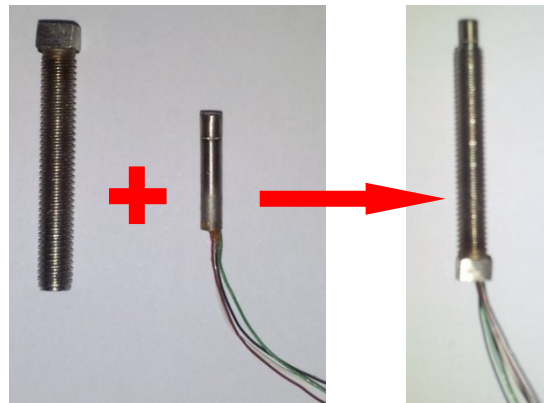


Figure 2.14 : Assembly details of Kulite transducers.

Three of the transducers have a working pressure range of 0 – 1.7 bara (0 – 25 psia), where other three have 0 – 3.4 bara (0 – 50 psia). For measurements during experiments, a in-house code written using LabVIEW software is used with its interface shown in Figure 2.15.

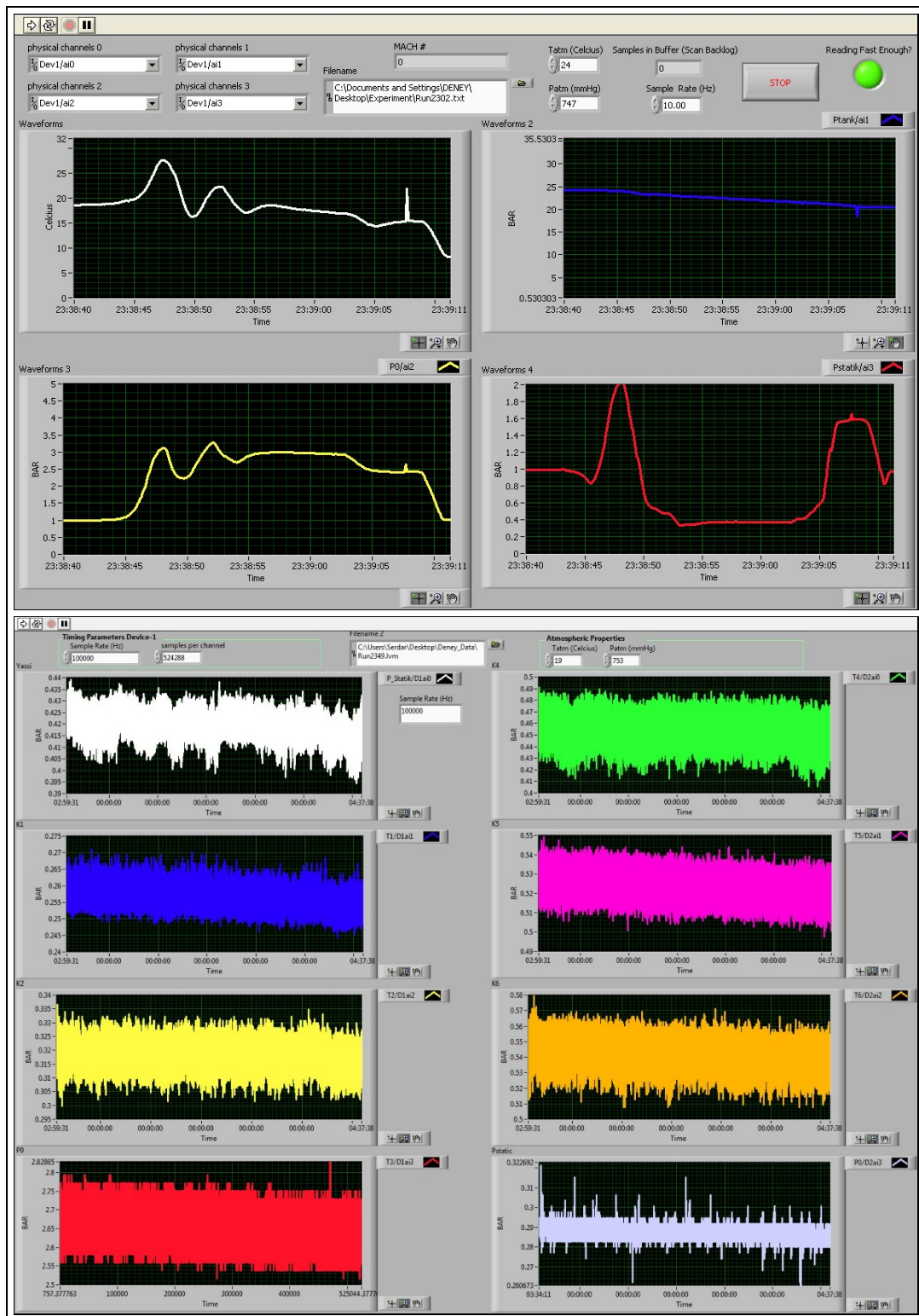


Figure 2.15 : Designed LabVIEW interface for measurements.

3. RESULTS

Before this thesis, a series of experiments was performed to investigate SBLI in the simplified model of the external compression inlet for the preliminary conceptual design project of TX\FX National Training/Fighter Aircraft. Therefore, this thesis is a complementary study containing experiments based on a simplified model of an internal compression inlet. Overall, the unsteadiness of shock waves, SBLIs, unstart and starting problems of internal compression inlets showed a significant reason why external compression inlets are more feasible for shock stability and have better performance characteristics as experienced with the previous national industrial project. Accordingly, an analytical study related to the optimization of total pressure recovery for external compression inlets is presented firstly and other results related to the internal compression inlet are introduced secondly. Moreover, analytical calculations of the designed internal compression inlet are followed by CFD analyses where the experimental results are presented in the last section.

3.1 External Compression Inlets

An analytical study was carried out in order to understand the limits of inlet geometry and to determine primary performance characteristics. By using shock wave and isentropic flow properties, a MATLAB code was written for several two-dimensional inlet geometries. Note that inviscid approach is valid for the used analytical equations. Therefore, friction losses are ignored. In other words, SBLI cannot be observed from the analytical results.

Figure 3.1 illustrates the results of total pressure loss for external compression inlets with n oblique shocks followed by a terminal normal shock. Total pressure ratio across a normal shock is denoted by $n = 0$ (blue line in Figure 3.1) which corresponds to a normal shock inlet. For 2, 3 and 4 shock inlets (n equals to 1, 2 and 3 respectively), a schematic diagram is shown in Figure 3.2 where freestream velocity is Mach 2. While p_{01} denotes the freestream total pressure, p_{02} corresponds to the downstream total pressure right after the terminal normal shock as seen in Figure 3.2c.

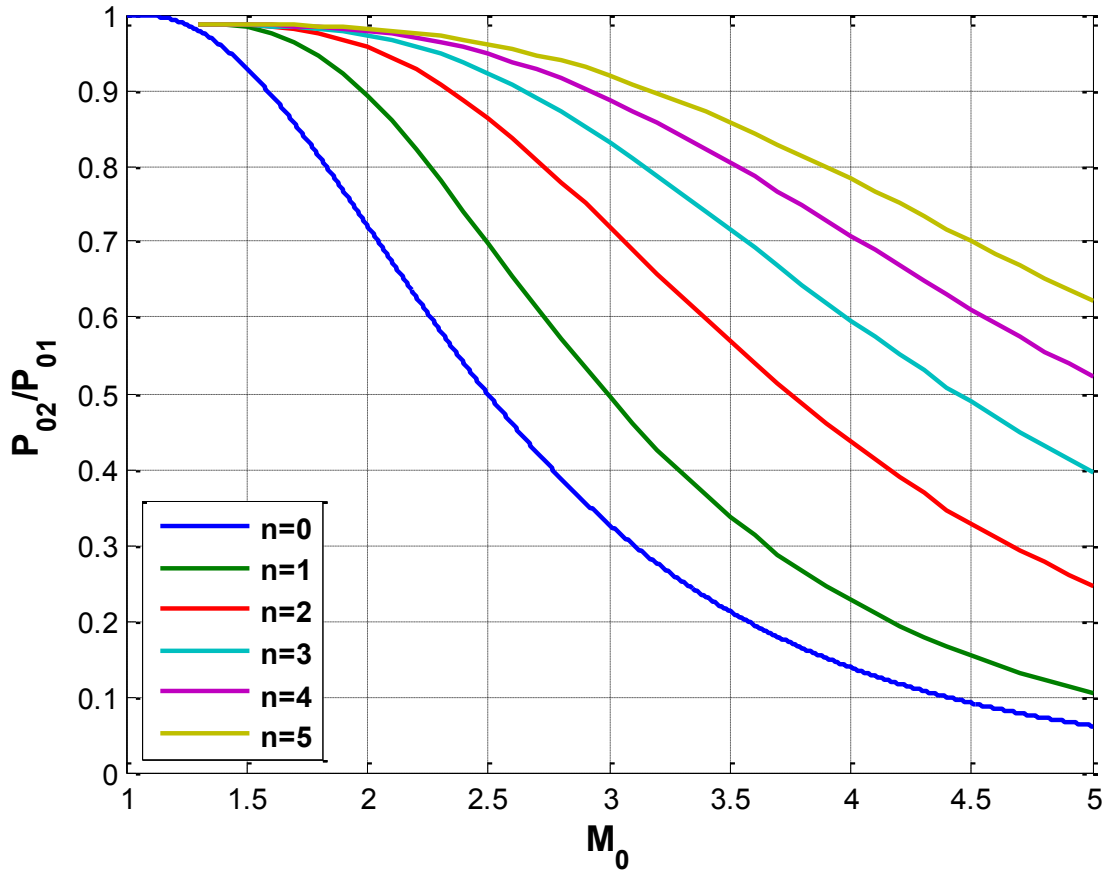


Figure 3.1 : Total pressure recovery of external compression inlets.

As stated before, across a normal shock the total pressure loss is less than 4% up to Mach 1.4. Therefore, in order to decrease the total pressure loss, it is desirable to diminish freestream velocity lower than Mach 1.4 before the terminating normal shock. Besides, due to the unsteadiness of shock waves, it is better to avoid Mach numbers very close to 1. Hence in the code, it was desired to obtain $Mach\ 1.25 \pm 0.01$ before the normal shock. Moreover, the tolerance value for the angles of ramps was adjusted up to the decimal point in degrees. Since the first upstream ramp encounters with the highest Mach number (freestream), it is more suitable to set the first deflection angle the smallest for efficiency on the basis of pressure recovery. As Mach number decreases passing through the subsequent ramps, deflection angles are increased gradually until reaching the preferred Mach number before the normal shock. For this purpose, an iteration process was defined in the code according to the number of oblique shocks. As seen from Figure 3.1, the more the number of ramps are, the higher the total pressure recovery is gained. Therefore, at high Mach numbers, number of deflection angles and their values are of vital importance.

Figure 3.2d shows the schematic view of isentropic compression. Infinitesimal deflection angles create infinitely weak oblique shocks. The structure of shock waves provides compression without total pressure loss which is the limiting case for external compression. With the help of characteristic lines, it is related to the reverse Prandtl-Meyer expansion. The disadvantage of this system is that it requires longer inlet geometries.

The short summary of the results obtained from the code is presented in Table 3.1. For a few freestream Mach numbers and number of oblique shocks, the changing Mach numbers at different regions (see Figure 3.2c which has regions numbered from 1 to 4) and the relating ramp angles can be easily compared between each other. p denotes static pressure where subscripts 1 and 2 correspond to freestream and downstream portion of the normal shock, respectively. If ramp angles are examined closely, the gradual increment can be observed from upstream to downstream direction. Additionally, as the number of oblique shocks (or ramps) rises, both the total deflection angle and the total pressure recovery increase.

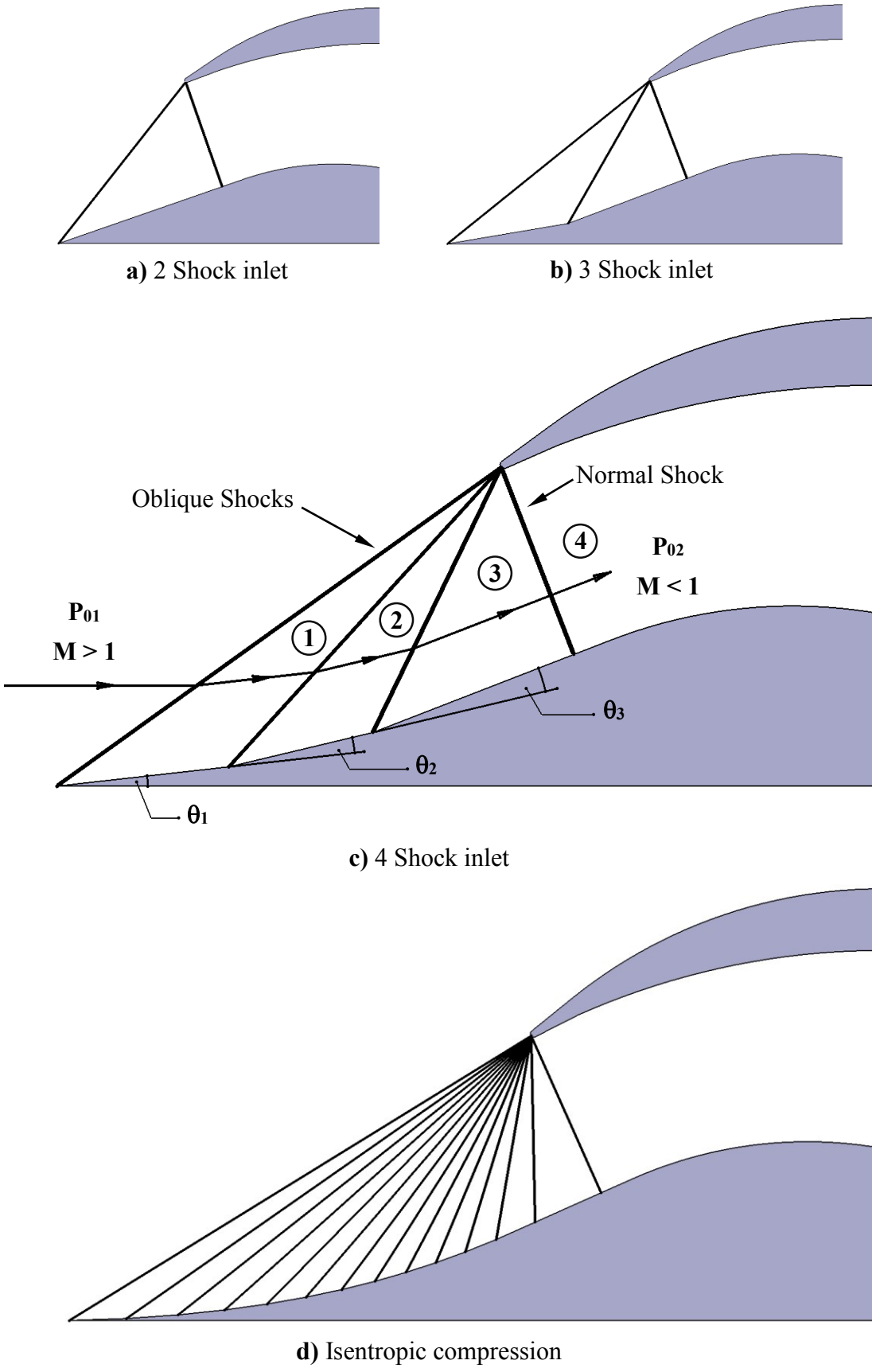


Figure 3.2 : Schematic diagram of external compression inlets.

Table 3.1 : Design calculations for external compression inlet performance.

	Freestream Mach #	Mach Number at Region #						Ramp Angle [degree]					Total Deflection Angle [degree]	P ₂ /P ₁	Total Pressure Recovery [%]
		1	2	3	4	5	6	θ ₁	θ ₂	θ ₃	θ ₄	θ ₅			
n = 1	2.0	1.254	0.811	-	-	-	-	19.2	-	-	-	-	19.2	2.86	89.3
	3.0	1.254	0.810	-	-	-	-	32.0	-	-	-	-	32.0	7.45	49.5
	4.0	1.260	0.807	-	-	-	-	37.2	-	-	-	-	37.2	14.07	22.8
	5.0	1.258	0.808	-	-	-	-	39.8	-	-	-	-	39.8	22.69	10.5
n = 2	2.0	1.655	1.252	0.812	-	-	-	9.6	11.2	-	-	-	20.8	3.08	95.6
	3.0	2.204	1.254	0.811	-	-	-	16.0	22.9	-	-	-	38.9	10.84	72.0
	4.0	2.670	1.257	0.809	-	-	-	18.6	29.0	-	-	-	47.6	27.03	43.6
	5.0	3.032	1.258	0.809	-	-	-	19.9	32.2	-	-	-	52.1	53.22	24.7
n = 3	2.0	1.771	1.530	1.251	0.812	-	-	6.4	7.0	7.8	-	-	21.2	3.13	97.3
	3.0	2.475	1.923	1.253	0.811	-	-	10.6	13.4	17.6	-	-	41.6	12.52	83.1
	4.0	3.115	2.264	1.251	0.812	-	-	12.4	16.4	23.9	-	-	52.7	37.27	59.7
	5.0	3.682	2.531	1.254	0.811	-	-	13.2	18.0	27.5	-	-	58.7	85.54	39.4
n = 4	2.0	1.828	1.652	1.464	1.252	0.811	-	4.8	5.1	5.5	5.9	-	21.3	3.14	97.9
	3.0	2.603	2.200	1.769	1.251	0.812	-	8.0	9.4	11.4	14.1	-	42.9	13.41	88.8
	4.0	3.336	2.697	2.046	1.254	0.810	-	9.3	11.4	14.6	20.1	-	55.4	44.08	70.8
	5.0	4.009	3.122	2.268	1.255	0.810	-	9.9	12.4	16.4	23.9	-	62.6	112.87	52.1
n = 5	2.0	1.864	1.725	1.578	1.424	1.251	0.812	3.8	4.0	4.3	4.5	4.8	21.4	3.16	98.2
	3.0	2.681	2.359	2.027	1.673	1.254	0.811	6.4	7.3	8.4	9.8	11.6	43.5	13.84	92.0
	4.0	3.469	2.956	2.445	1.906	1.255	0.810	7.4	8.7	10.5	13.2	17.2	57.0	48.63	78.2
	5.0	4.207	3.485	2.792	2.096	1.255	0.810	7.9	9.4	11.7	15.1	21.0	65.1	134.36	62.1

3.2 Internal Compression Inlets

The primary purpose of this section is to collect experimental data and discuss the results based on SBLIs and unstart phenomena. In order to understand the shock structure inside the designed inlet model, first an analytical study was carried out and then 2D CFD analyses were performed to compare the results. In the last section, results of experiments are given in detail.

3.2.1 Analytical Calculations

An internal compression inlet geometry which has top and bottom ramp angles of 4° each is chosen for the preliminary design. At least one reflection of oblique shocks is aimed before the throat and the existence of expansion waves as shown in Figure 3.3. The ratio of the captured area to the throat area for such an inlet geometry is around 1.288. On the other hand, since the desired Mach number for the experiments is chosen as 2, by using Equation (1.3), the theoretical area ratio is calculated as 1.216. In order to overcome the starting problem of internal compression inlets, area ratio should be lower than the theoretical value. The ratios for theoretical result and the actual geometry are close to each other, but the slight difference in values is expected to cause the inlet unstart even though the inviscid shock wave calculations do not reveal this problem at all. Studies related to unstart phenomena continue with CFD analyses and experiments in the following sections.

In order to determine the shock wave positions and the compressible flow properties of such inlets, another MATLAB code was developed which calculates the shock-shock interactions and shock-expansion interactions by using an iterative process.

For the first model, the regions of the shock wave structure are numbered from 1 to 8 in Figure 3.4. The results obtained from the code are given in Table 3.2 in which the last two columns show static pressure and density ratios. The dashed lines in Figure 3.3 and 3.4 are a rough estimation due to the lack of the computation at regions where two expansion waves interact.

The second model is shown in Figure 3.5. The height of the throat is enlarged by 4 mm with respect to the first model. The ratio of the captured area to the throat area for this

new geometry is 1.167 which is lower than the required theoretical value. If shock wave structure is examined closely, it is observed that the expansion waves interact with the shock waves and the reflection of shock waves occur after the interaction. Since 4° ramps and turns create weak shock and expansion waves, refraction of shocks and expansions due to the interaction cannot be observed easily for this case. Furthermore, this interaction creates a slip line that separates the two regions having the same static pressures but different flow velocities. Since the model upper and lower ramps are identical, which generates the interacting shocks with the same strength, no slip line occurs after shock-shock interaction for this case. Flow properties of the regions shown in Figure 3.6 numbered from 1 to 8 are obtained from the code and the results are given in Table 3.3. As compared to the first model, it can be said that expansion waves reduce the strength of reflecting shock waves slightly. The dashed lines in Figure 3.5 and 3.6 are an approximation of the extensions of shock and expansion waves. In reality, due to the mixed regions generated by the expansion-expansion interactions and reflection of expansion waves from the walls, shock waves are refracted and further reflection of shocks occur slightly more upstream positions than shown in the schematics in the figures.

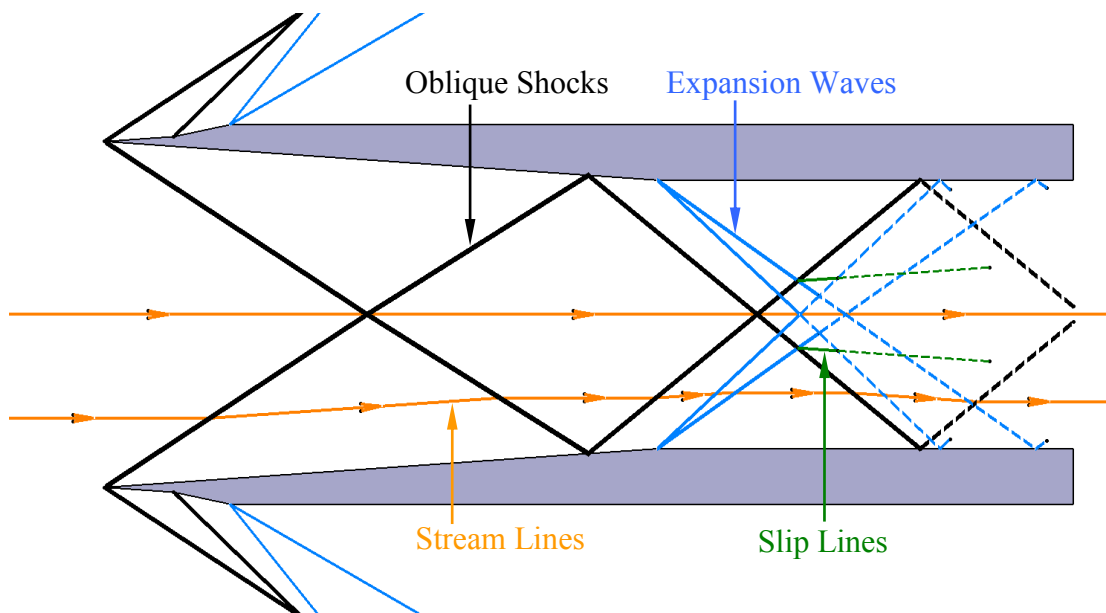


Figure 3.3 : Shock wave structure of the 1st internal compression inlet model.

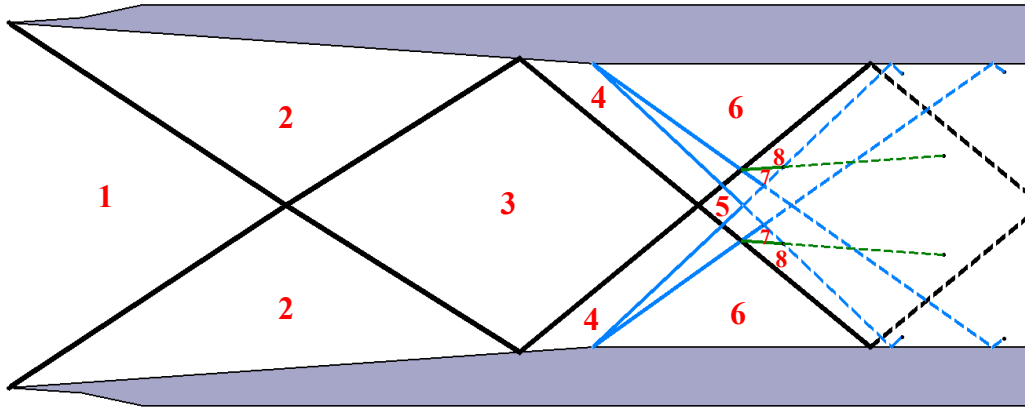


Figure 3.4 : Interior flow regions of the 1st internal compression inlet model.

Table 3.2 : Analytical results of the 1st internal compression inlet model.

Region #	Mach	$p\#/p_1$	$\rho\#/\rho_1$
1	2.0	1.0	1.0
2	1.857	1.247	1.170
3	1.718	1.539	1.360
4	1.582	1.886	1.572
5	1.445	2.297	1.810
6	1.717	1.540	1.360
7	1.581	1.886	1.572
8	1.581	1.886	1.572

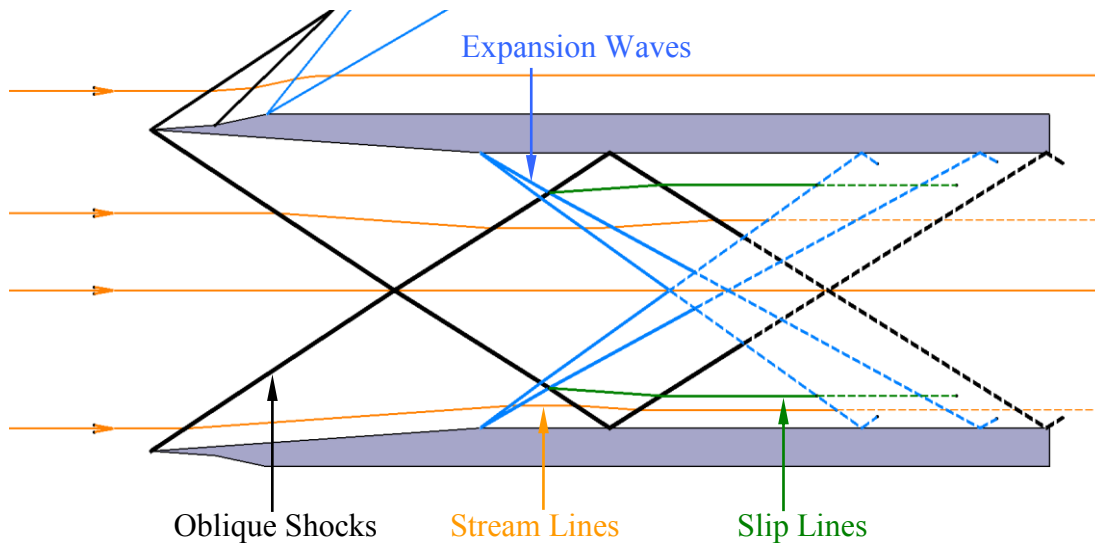


Figure 3.5 : Shock wave structure of the 2nd internal compression inlet model.

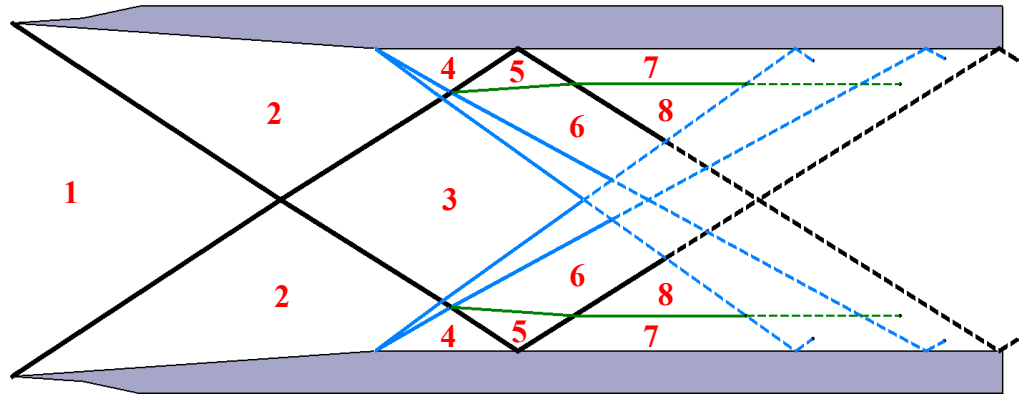


Figure 3.6 : Interior flow regions of the 2nd internal compression inlet model.

Table 3.3 : Analytical results of the 2nd internal compression inlet model.

Region #	Mach	$p\#/p_1$	$\rho\#/\rho_1$
1	2.0	1.0	1.0
2	1.857	1.247	1.170
3	1.718	1.539	1.360
4	1.999	1.000	1.000
5	1.856	1.247	1.170
6	1.856	1.247	1.170
7	1.717	1.540	1.360
8	1.717	1.540	1.360

3.2.2 CFD Analyses

2D Computational Fluid Dynamics analyses were performed both for the first and second model in order to compare the results obtained from analytical calculations. In the analyses, while ANSA software of Beta CAE Systems S.A. was used for mesh generation, FLUENT software of ANSYS Inc. was used as the solver. Both inviscid and viscous cases were studied to reveal the effects of SBLI.

Mesh properties of the CFD model are given in Table 3.4. For the inviscid case, no boundary layer mesh was generated and the edge length of cells was kept approximately around 0.11 mm. A uniform, structured grid was created with quadrilateral elements. For the viscous case, an additional boundary layer mesh was generated, in which the first cell height ensures $y^+ \leq 1$ condition to resolve the viscous sublayer. Figure 3.7 shows the details of cell edge-length for the viscous case of the second model and cell growth in the boundary layer region is kept relatively small.

Table 3.4 : Mesh properties.

Mesh Information	
Grid Type	Structured
Cell Type	Quadrilateral
Cell Number	~ 6.7 million (Inviscid case) ~ 9.6 million (Viscous case)
Inlet Length	140 mm
Cell Length	~ 0.11 mm

Boundary Layer Information	
First Cell Height	0.00127 mm
y^+	< 1

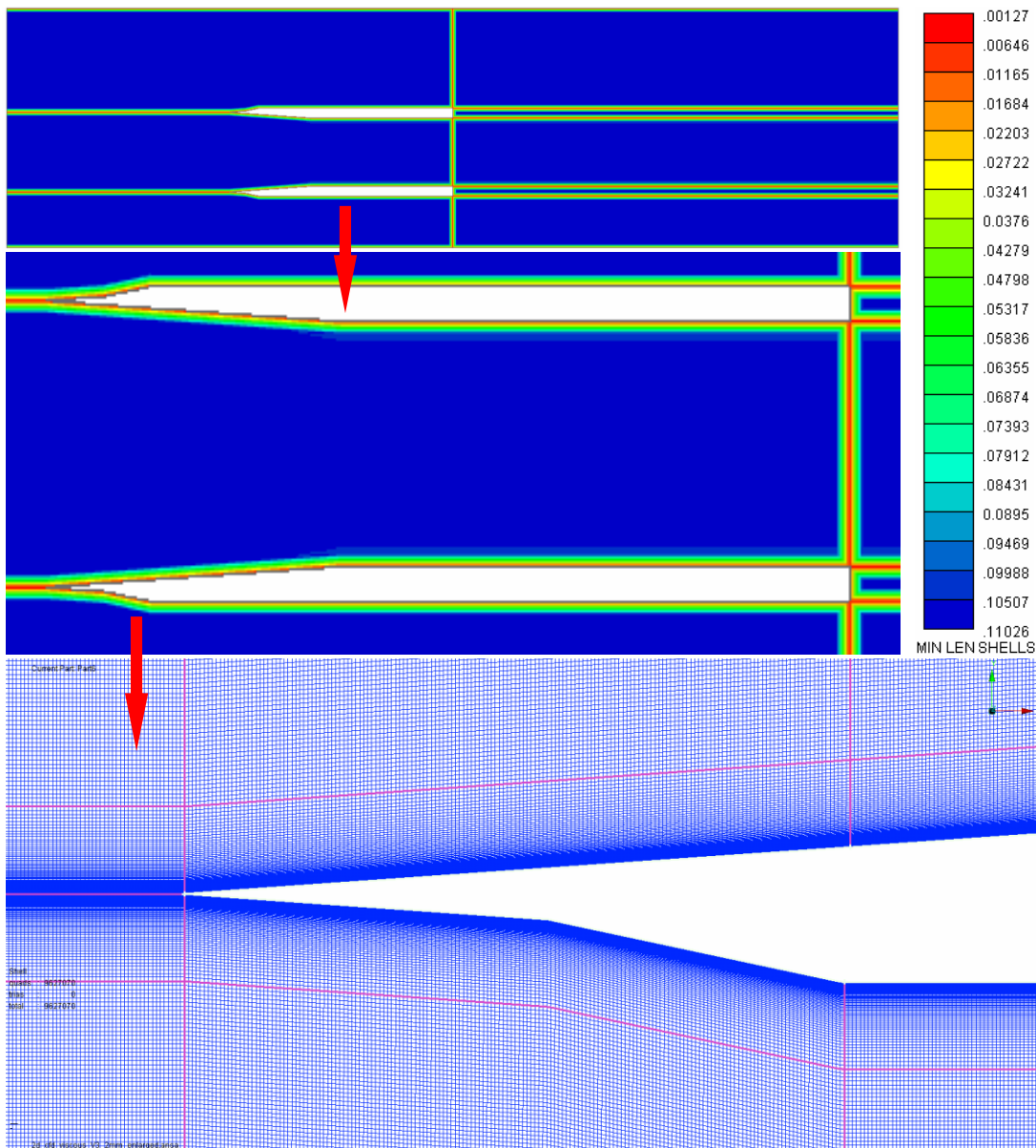


Figure 3.7 : Cell edge length details of viscous 2nd model.

Boundaries of the CFD model are illustrated in Figure 3.8 and the boundary conditions are tabulated in Table 3.5. For inflow (green line), Mach number was defined as 2.0. The upper and lower walls of the wind tunnel and the walls of the internal compression inlet were modelled as stationary walls (blue and black lines). For outflow (red line), non-reflecting boundary condition was used.

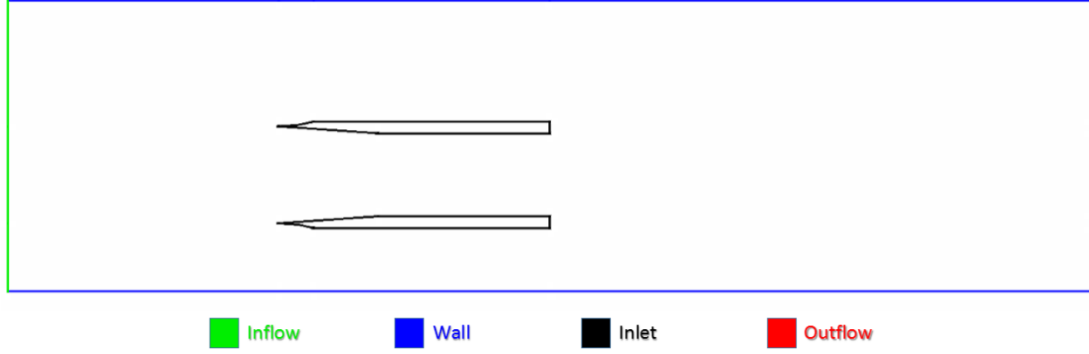


Figure 3.8 : Boundaries of the CFD model.

Table 3.5 : Boundary conditions of CFD model.

Boundary	Type
Inflow	Pressure-Far-Field
Wall	No-Slip Wall
Inlet	No-Slip Wall
Outflow	Pressure-Outlet

In order to simulate the conditions in the wind tunnel test section, isentropic flow equations are used taking the fluid as standard air assumed as ideal gas.

$$\begin{aligned}
 T_{tank} &= T_0 = 288 \text{ K} \\
 \left. \frac{T_0}{T} \right|_{M=2} &= 1 + \frac{\gamma - 1}{2} M^2 = 1.8 \\
 T &= \frac{T_0}{T_0/T} = \frac{288 \text{ K}}{1.8} = 160 \text{ K} \\
 p_{tank} &= p_0 = 2.8 \text{ atm} \\
 \left. \frac{p_0}{p} \right|_{M=2} &= \left[1 + \frac{\gamma - 1}{2} M^2 \right]^{\frac{1}{\gamma - 1}} = 7.8244
 \end{aligned} \tag{3.1}$$

$$p = \frac{p_0}{p_o/p} = \frac{2.8 \text{ atm}}{7.8244} = 0.357855 \text{ atm} \cong 36260 \text{ Pa} \quad (3.2)$$

$$a = \sqrt{\gamma RT} = \sqrt{1.4 \times 287 \text{ J/kg} \cdot \text{K} \times 160 \text{ K}} \cong 253.55 \text{ m/s} \quad (3.3)$$

Where T_0 and T is the tank (stagnation) and the freestream temperatures, respectively, M is the freestream Mach number, γ is the ratio of specific heats (1.4 for air), p_0 and p is the tank (stagnation) and the freestream absolute pressures respectively, a is the speed of sound and R is the specific gas constant.

As the initial condition, the inflow temperature and pressure were set to 160 K and 36260 Pa, respectively, as derived from Equations 3.1 and 3.2. In addition, from Equation 3.3, freestream velocity in the x -direction was set to 507 m/s which equals twice the speed of sound.

The properties related to the methodology of the analysis are presented in Table 3.6. In order to obtain a fast solution, one-equation turbulence model (Spalart-Allmaras) was selected.

Table 3.6 : Analysis methodology.

Solver Type	Density-Based
Velocity Formulation	Absolute
Time	Steady
Space	2D-Planar
Turbulence Model	Spalart-Allmaras
Formulation	Implicit
Flux Type	AUSM
Spatial Discretization	First Order Upwind
Gradient	Cell-Based

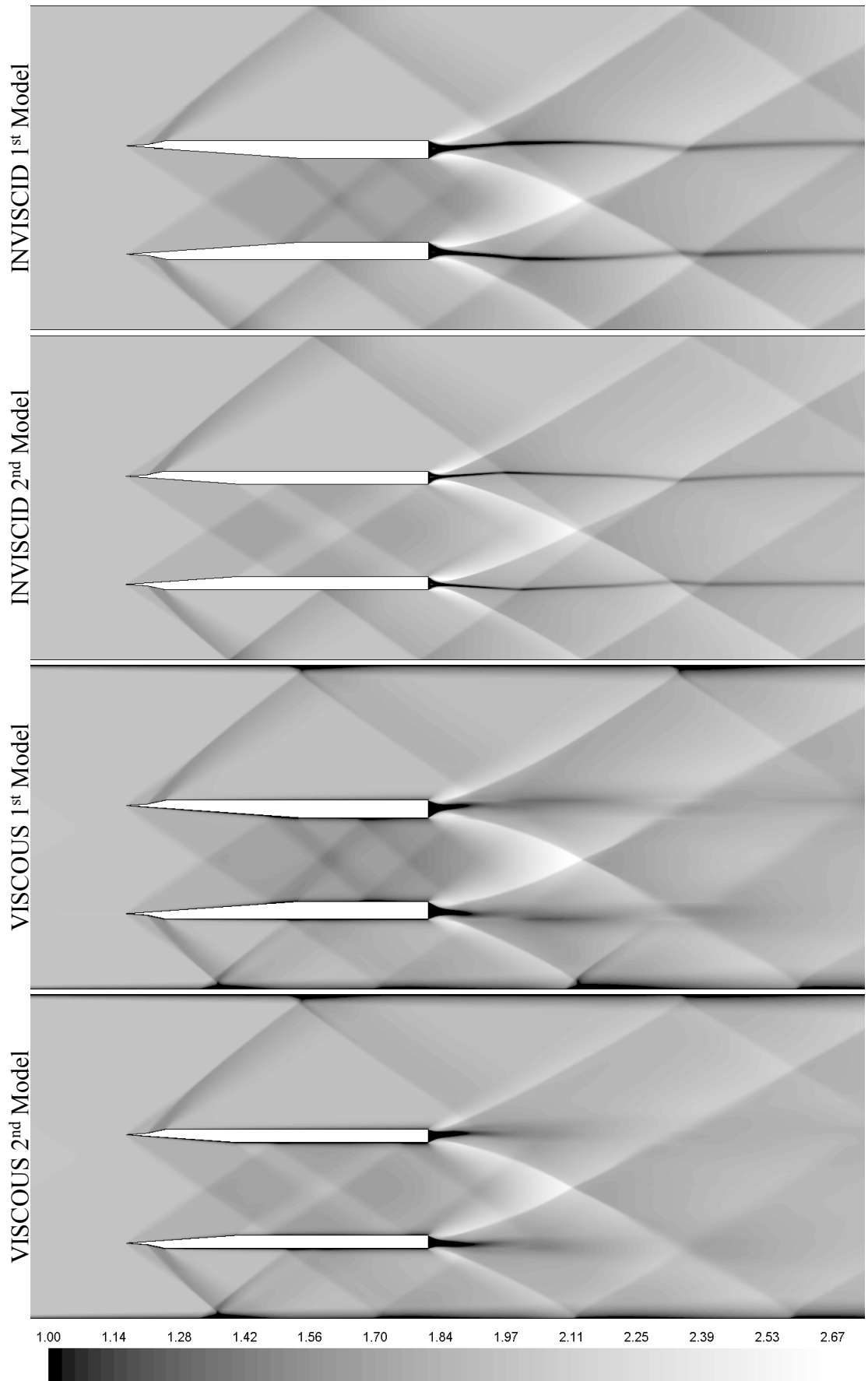


Figure 3.9 : Mach contours.

Mach contours from the CFD analyses are given in Figure 3.9. The results are considerably consistent with the theoretical calculations. Table 3.7 shows the Mach number contour levels obtained from the “colorbar” output for the inviscid case of the second model. As compared with Table 3.3, the values of the Mach numbers in various regions obtained from CFD calculations agree quite well with those in the analytical results. Even though the first model seems to have started flow both in the CFD analyses and in the analytical calculation, as mentioned previously, due the high value of the ratio of capture to throat areas, the inlet model stays in the unstarted condition in the experiments (see the following section). The possible reason for the started inlet in the CFD results can be the fact that the 2D-Planar solution does not take into account the three-dimensional and unsteady effects of the actual flow.

Table 3.7 : Mach number range outputs of the inviscid 2nd model.

Region #	Mach Number Range	
	Min	Max
1	1.998	2.001
2	1.856	1.859
3	1.717	1.720
4	1.995	1.998
5	1.853	1.856
6	1.853	1.856
7	1.717	1.720
8	1.717	1.720

Since ramp angles are relatively small, which result in relatively weak shock waves, no significant effect such as boundary layer separation and reattachment shock is observed related to SBLIs inside the inlet as presented in Figure 3.10a. However, Mach contours illustrate that the boundary layer thickness is increased near the downstream of the shock, which is an evidence of SBLI. On the other hand, if outside of the inlet is examined, due to the adverse pressure gradient created by the reflecting shock, reverse flow vectors demonstrate the possible boundary layer separation in Figure 3.10b. In addition to Mach contours and velocity vectors, non-dimensional pressure and density contours are illustrated in Figure 3.11 and 3.12, respectively where they agree well with the analytical calculations.

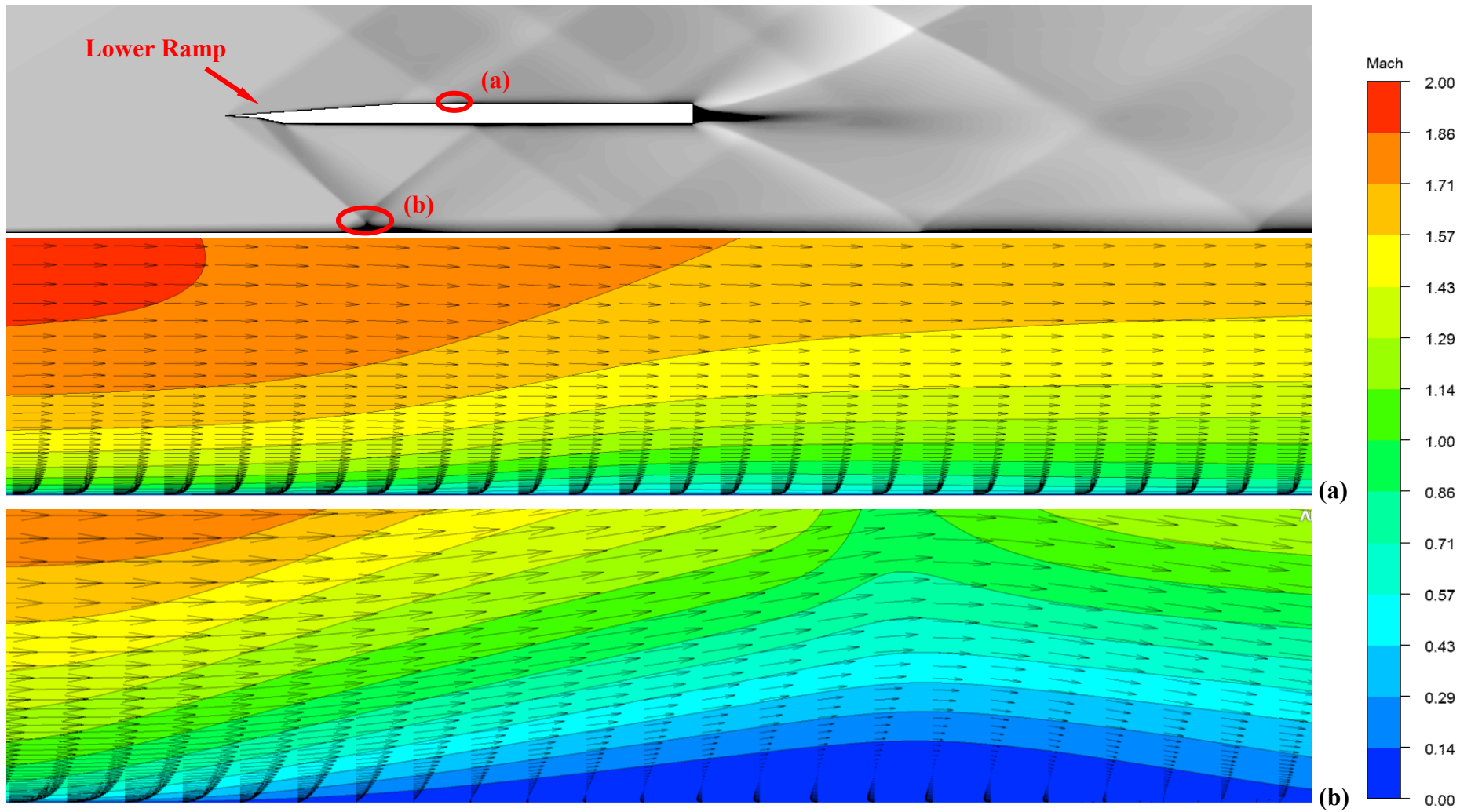


Figure 3.10 : Vector field of the viscous calculations for the 2nd model.

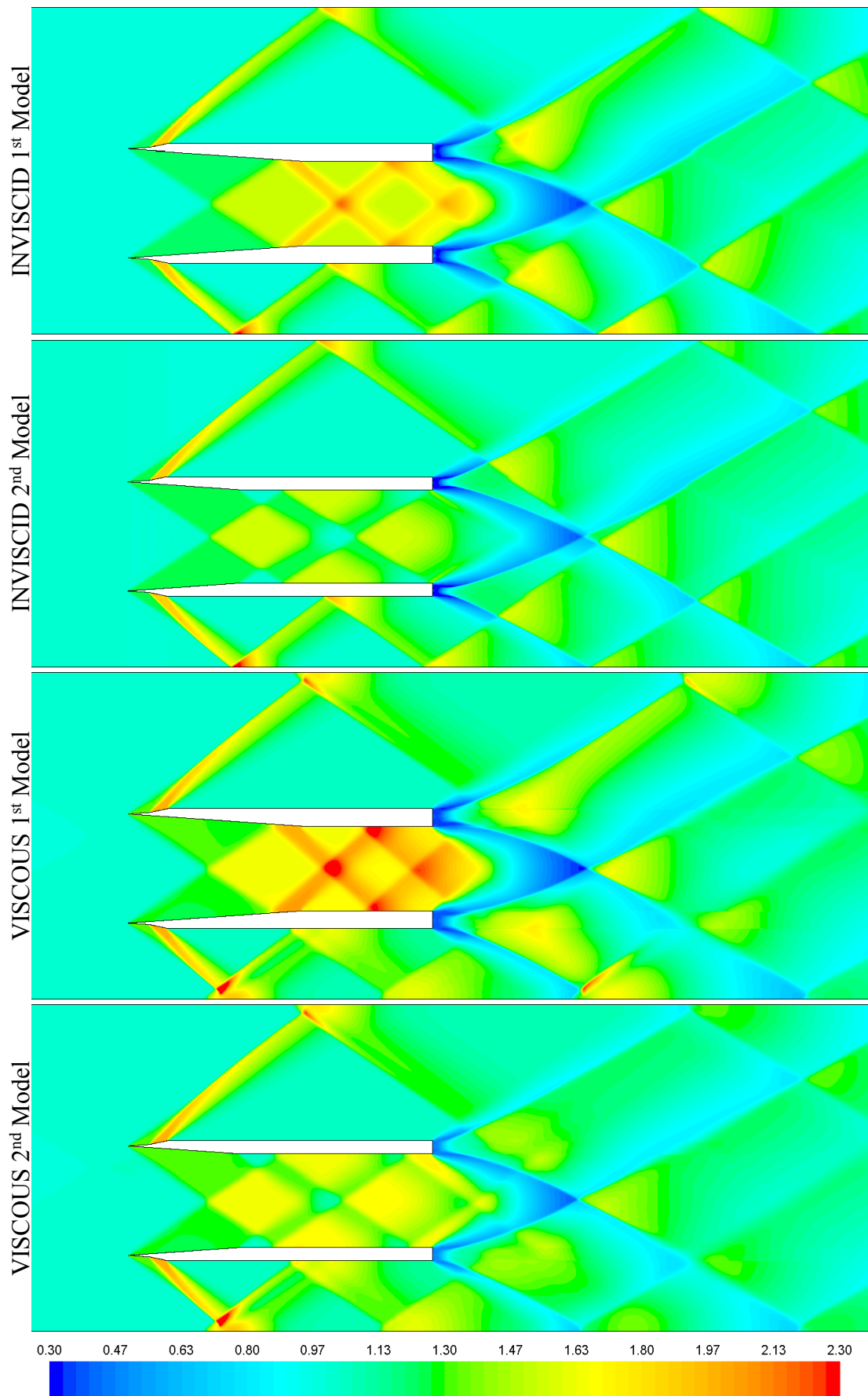


Figure 3.11 : p/p_∞ contours.

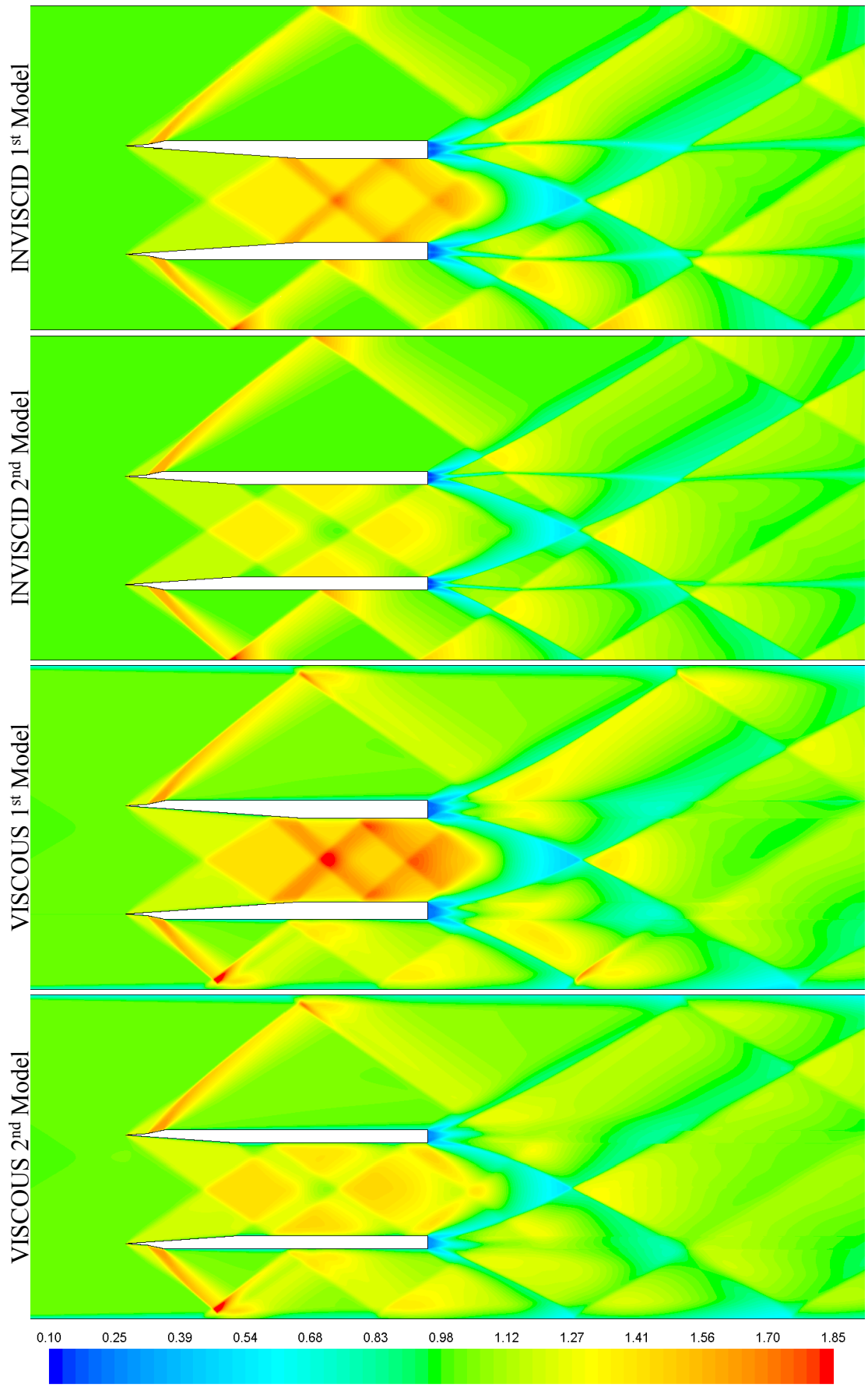


Figure 3.12 : ρ/ρ_∞ contours.

3.2.3 Experimental Results

Experiments with the first and second models were performed and the effect of captured area to throat area ratio was observed for inlet unstart characteristics. These models are called as "*short*" models in this thesis because additionally an extension part was attached to the back of the second model and thereby a "*long*" model was created. A total of about 70 runs were performed in the tunnel. Firstly, shadowgraph images were obtained to understand the shock wave structure and unstart condition. Secondly, pressure measurements were performed at different sampling rates, and finally, surface oil flow visualization method was used in order to observe the separation and reattachment lines caused by the SBLIs. Moreover, blocks having different thicknesses were placed at the back of the long and short models to create back pressure which simulates the existence of jet engine and as a result, unstart behavior was observed better.

As mentioned in the analytic calculations section, since the ratio of the capture area to the throat area was slightly higher than the theoretical value, as shown in Figure 3.13 unstart condition was observed in the experiments for this model. Several runs performed with Mach number varied between 2.03 and 2.14 resulted in the same unstart condition.

In Figure 3.13, arrows denoted by "*C*" shows the internal cracks of acrylic side wall. "*B*" denotes the detached normal shock just in front of the inlet, and hence the flow inside the inlet becomes subsonic. "*S_{out}*" shows the shock waves formed outside of the inlet by the ramps on the model side walls, reflecting shocks from test section floor and test section side walls and other small protrusions such as mounting bolts and junction surfaces on the outside of model. In addition, since suction mechanism is on during the experiments in the upper wall of the test section, shock waves seem to have been absorbed in the ceiling.

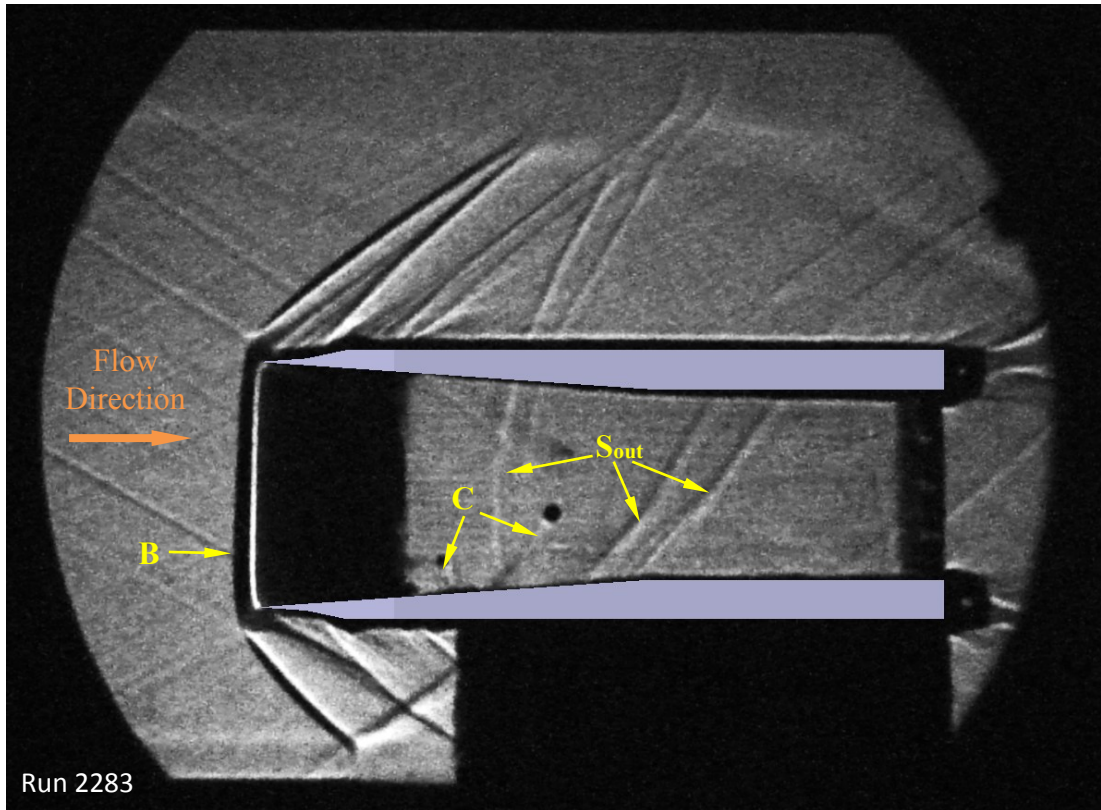


Figure 3.13 : Shadowgraph image of the 1st model at Mach 2.03.

By machining off both of the inner surfaces downstream of the ramps by 2 mm, throat height was enlarged by 4 mm. Thus, second model geometry was obtained with capture-to-throat area ratio satisfying the theoretical value of started inlet condition.

In Figure 3.14, the results from the analytic calculations (see section 3.2.1) are superimposed on the experimental results where “ S_r ” shows the shock waves created by 4° ramps and the reflections of ramp shocks are indicated by “ S ”. The superimposed image (see red arrow in the figure) shows that the analytical calculations agree quite well with the experiment up to the point where expansion-expansion interaction occurs. Also, due to the SBLI, the shock reflection points of the ramp shocks are slightly in the front with respect to the analytical calculation.

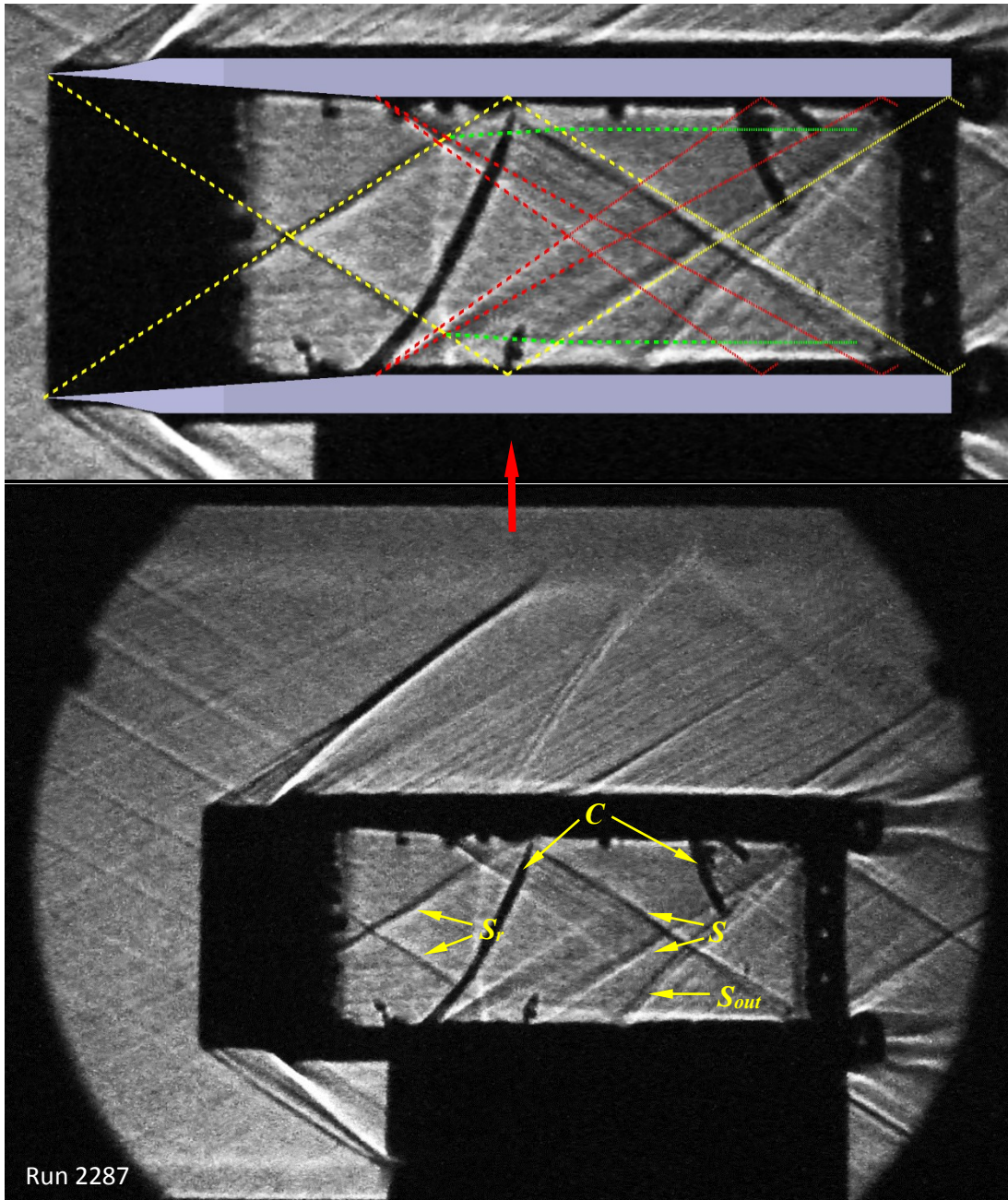


Figure 3.14 : Shadowgraph image of the flow around 2nd model at Mach 2.03.

For some of the experiments, because of very small misalignments between the components of the inlet model, which occurred during assembling, the model had a slight positive angle-of-attack of about 1° . Therefore, reflections of the ramp shocks appear at slightly different streamwise positions on the upper and lower walls of the inlet as shown with vertical arrows in Figure 3.15. “*E*” denotes the expansion waves. If the figure is examined closely, small refractions of waves caused by shock-shock and shock-expansion interactions can be observed. Since deflection and turn angles are small, the refraction of the waves after interactions is also very small.

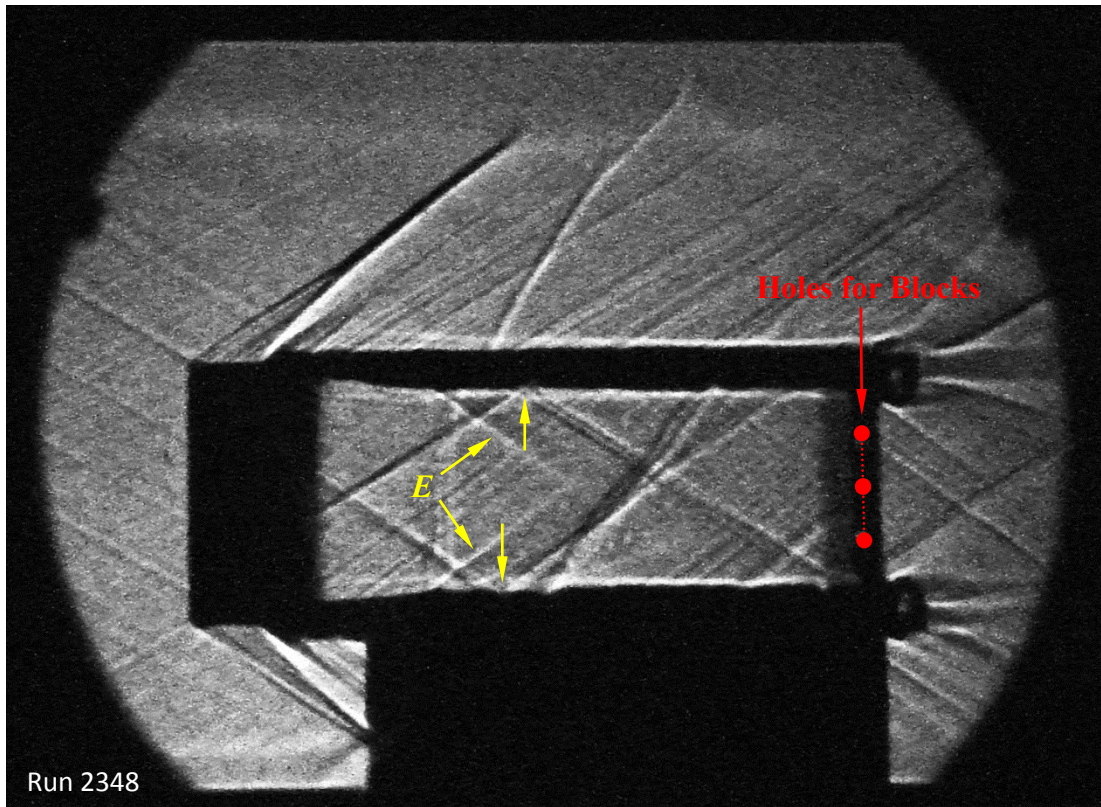


Figure 3.15 : Shadowgraph image at Mach 2.02.

The essential objective of using internal compression inlets was to obtain a normal shock wave after one or more oblique shock reflections. On this basis, blocks with different sizes were tested to achieve the desired condition. These blocks are used to produce a back pressure which resembles the presence of the engine downstream of the inlet. Table 3.8 shows some of the experiments performed with different sets of size, shape and vertical location of blocks. As can be seen from the results given in the table, none of the sets produced a flow with series of oblique shocks followed by a normal shock within the inlet. These results show the difficulty of obtaining a terminating normal shock inside the inlet. The back pressure produced by the blocks either is large enough to push the oblique shock system out of the inlet and cause unstart or small enough to maintain started condition. Slight variations in the size of the block change the type of the flow within the inlet from started to unstarted or vice versa. It was impossible to obtain an intermediate case with a normal shock wave within the inlet using the block sizes given in Table 3.8. While the leftmost column shows the run number which is just a record number for the related experiment, the rightmost column indicates the size and the shape of the block. Fourth column shows

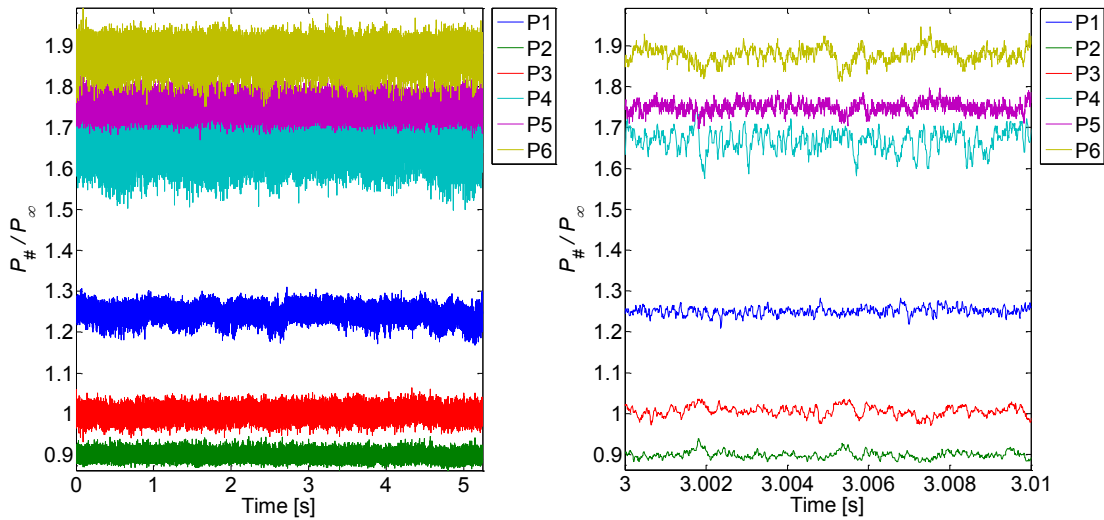
the value of the block thickness in millimeters, in which the rows are separated into three for each cell. These equally divided rows in the table indicate the predefined positions on the exit plane where blocks are placed as shown in red in Figure 3.15.

Table 3.8 : Experiments with blocks placed at the back of the inlet model.

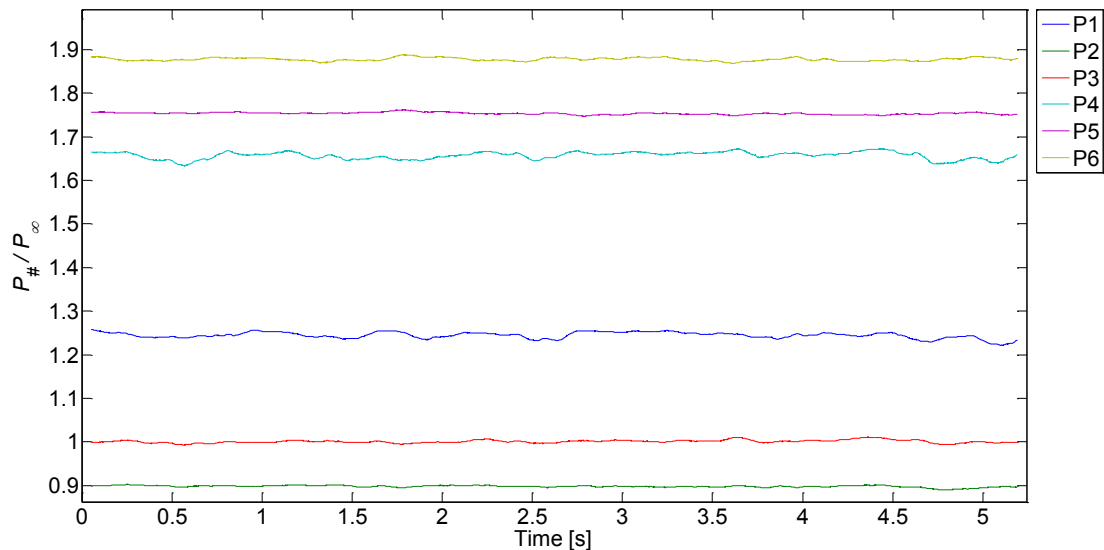
Run #	Mach	Condition	Block Height [mm]	Block	Run #	Mach	Condition	Block Height [mm]	Block
Run2302	1.94	Unstarted	4.2	■	Run2308	2.01	Started	0.8	●
Run2303	1.94	Unstarted	3.6	■	Run2309	2.01	Started	0.8	●
Run2304	1.94	Unstarted	2.9	●	Run2310	2.01	Unstarted	0.8	●
Run2305	2.15	Unstarted	2.4	●	Run2317	2.01	Unstarted	0.5	●
Run2306	2.01	Unstarted	1.9	●	Run2324	2.01	Unstarted	1.2	●
Run2320	2.14	Unstarted	1.9	●	Run2325	2.14	Unstarted	1.2	●
Run2307	2.14	Unstarted	1.9	●	Run2326	2.14	Unstarted	1.2	●

Surface pressure measurements were performed both for short and long models. The location of pressure transducers on the model floor are illustrated by red lines numbered from 1 to 8 in Figure 3.17. The transducer at the most upstream location was a flat-type and the rest of the five transducers were placed into selected taps to provide a somewhat evenly distribution along the model floor. A sample set of pressure time history for the short and started model is given in Figure 3.16 where data sampling frequency and freestream Mach number were 100 kHz and 2.14, respectively. Mean values were obtained by applying moving average smoothing with a window of 10001 data points. The total number of data points was set as multiples of two for FFT analyses to obtain SPL values (see Appendix A). Before each run pressure data were taken with no flow in the tunnel to balance the possible drift and noise on channels. When the no-flow data were compared with the actual flow data, a frequency of 50 Hz of the power main and its harmonics were observed. However, for cases where the normal shock stays in front of the inlet, no other dominant frequency in subsonic

region was obtained due to the lack of normal shock wave formation (thereby the effect of a strong SBLI) inside the inlet.



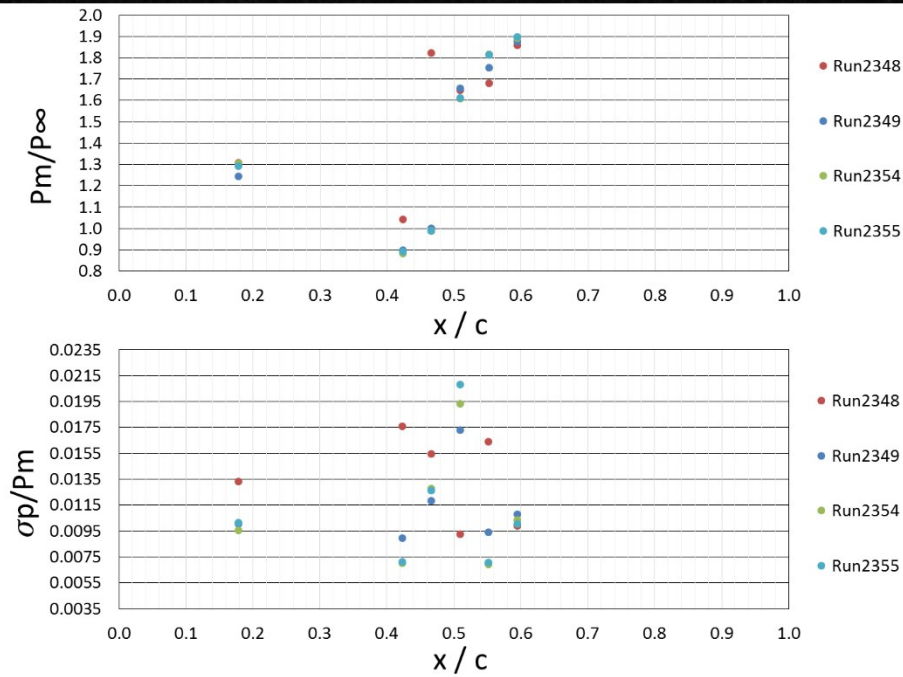
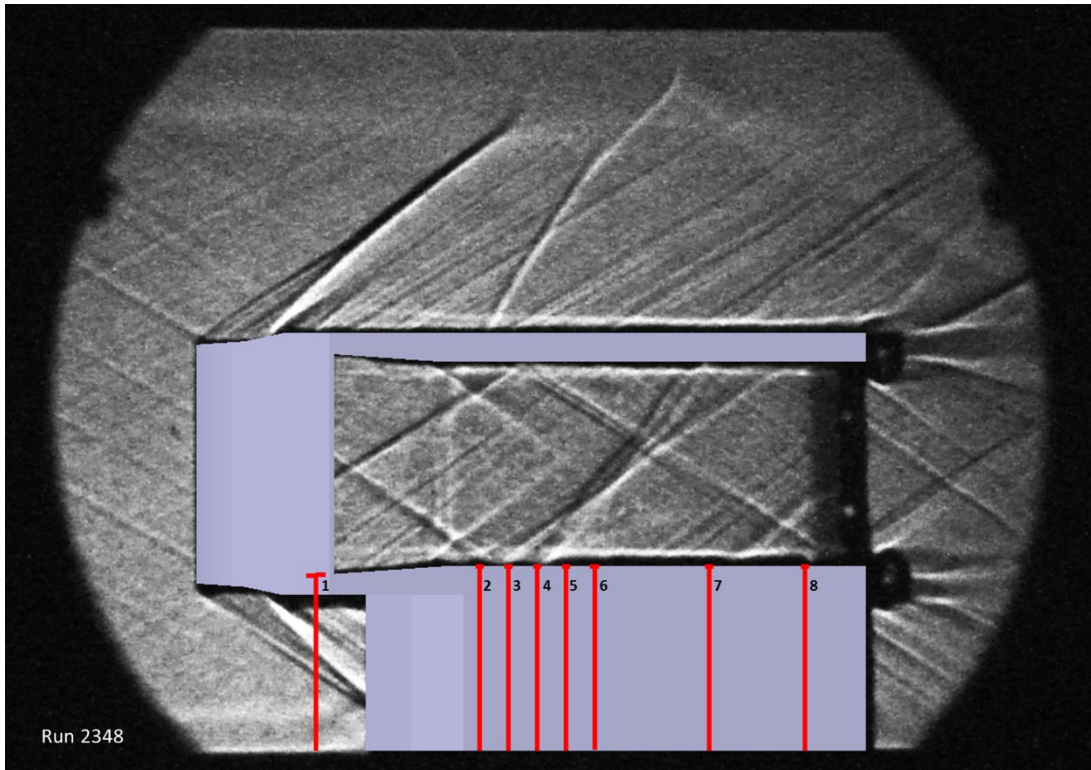
a) Pressure data and 10 ms window



b) Mean pressure data for each channel

Figure 3.16 : $p_{\#} / p_{\infty}$ values of Run2349.

For cases of started inlet, analytical and CFD results agree quite well with experimental results up to the ramp shock reflection point as plotted in Figure 3.17. Due to relatively weak SBLIs caused by the oblique shock reflections on the inlet floor, nondimensional pressure values are slightly higher from the analytical results after the interaction. Furthermore, RMS values simply show the amplitude of pressure fluctuations. From Figure 3.17, it can be observed that RMS values increase around SBLI regions.

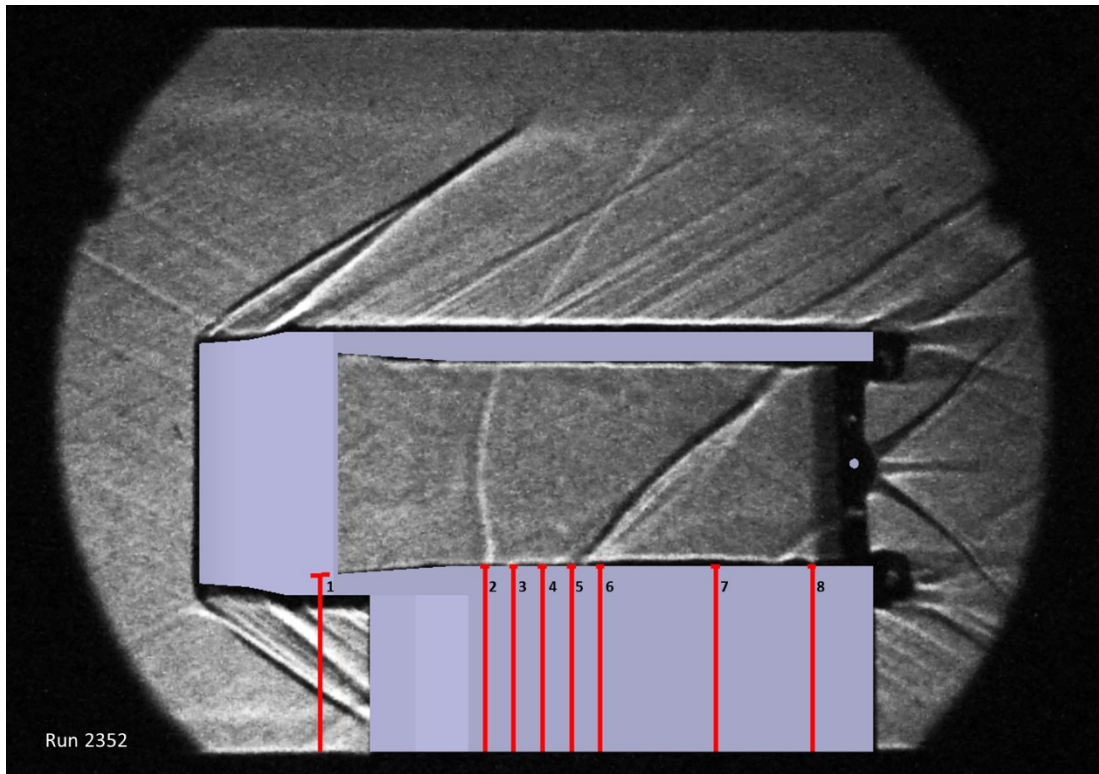


Run #	2348	2349	2354	2355
Mach #	2.02	2.14	2.14	2.15

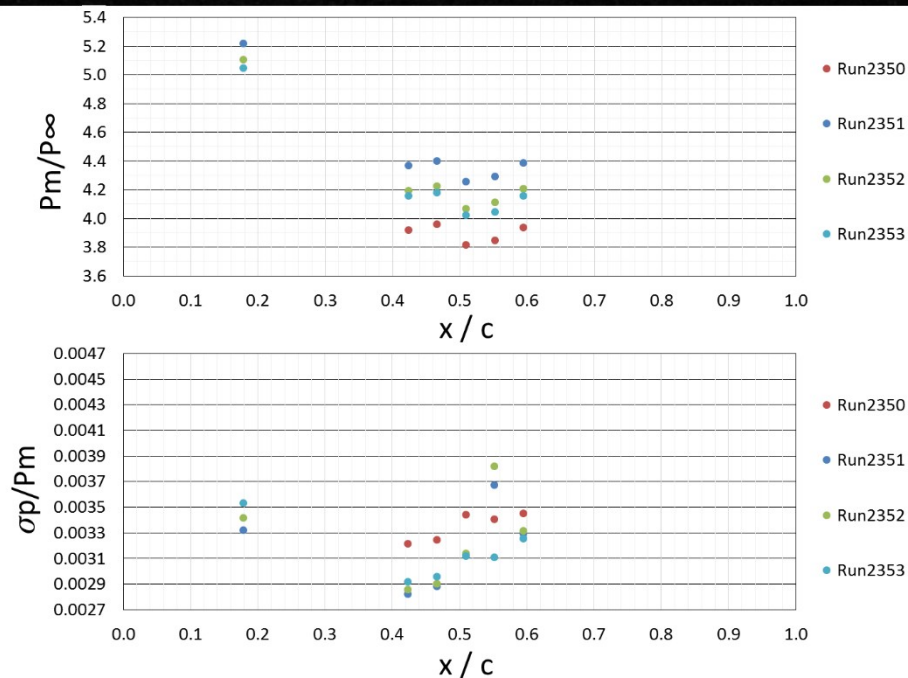
Figure 3.17 : Short started model without block.

When a block was placed in the center height at the back of the model, unstart condition was obtained for certain block sizes. Therefore, the flow inside the inlet became subsonic. From normal shock relations, at Mach 2.0 the ratio of p_2/p_1 is calculated as 4.5 where p_1 is the freestream pressure and p_2 is the static pressure behind

the normal shock. Also, this ratio becomes 5.18 at Mach 2.14, which agrees with the data plotted in Figure 3.18 measured at the first pressure transducer. Since there was no interaction inside, RMS values were lower compared to started case.



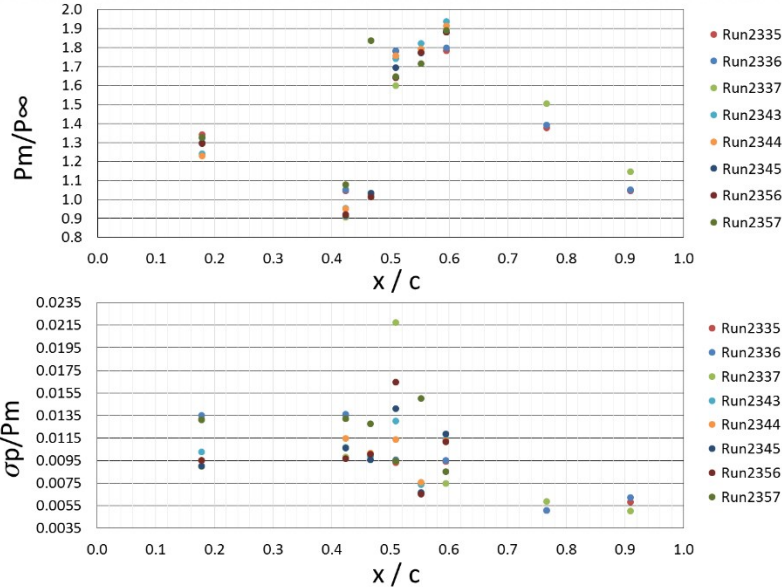
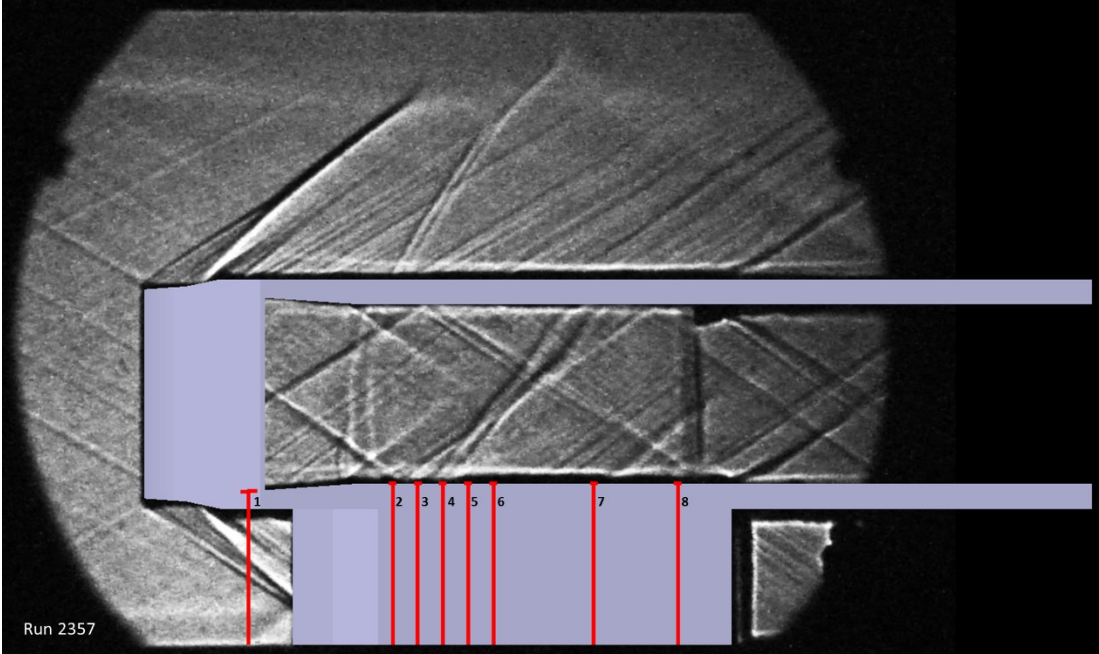
Run 2352



Run #	2350	2351	2352	2353
Mach #	2.01	2.14	2.14	2.13
Block [mm]	1.9	1.9	1.2	1.2

Figure 3.18 : Short unstarted model with block in the center height at the back.

Additionally, experiments with the long model were performed as illustrated in Figure 3.19. No significant difference with the short started model was observed in the pressure data. The downward trend of pressure transducers 7 and 8 showed the existence of expansion waves coming from the end of the upper ramp.



Run #	2335	2336	2337	2343	2344	2345	2356	2357
Mach #	2.03	1.96	2.16	2.15	2.14	2.14	2.14	2.02

Figure 3.19 : Long started model without block.

In the experiments with the long model for the unstarted condition, since the pressure downstream of the normal shock was quite high, the flat transducer in the first tap became out of range. Therefore, the pressure measurement in the first tap were

performed correctly only for Run2342 as shown in Figure 3.20. Likewise, the obtained nondimensional pressure and RMS values stayed nearly the same as those in the short unstarted model case.

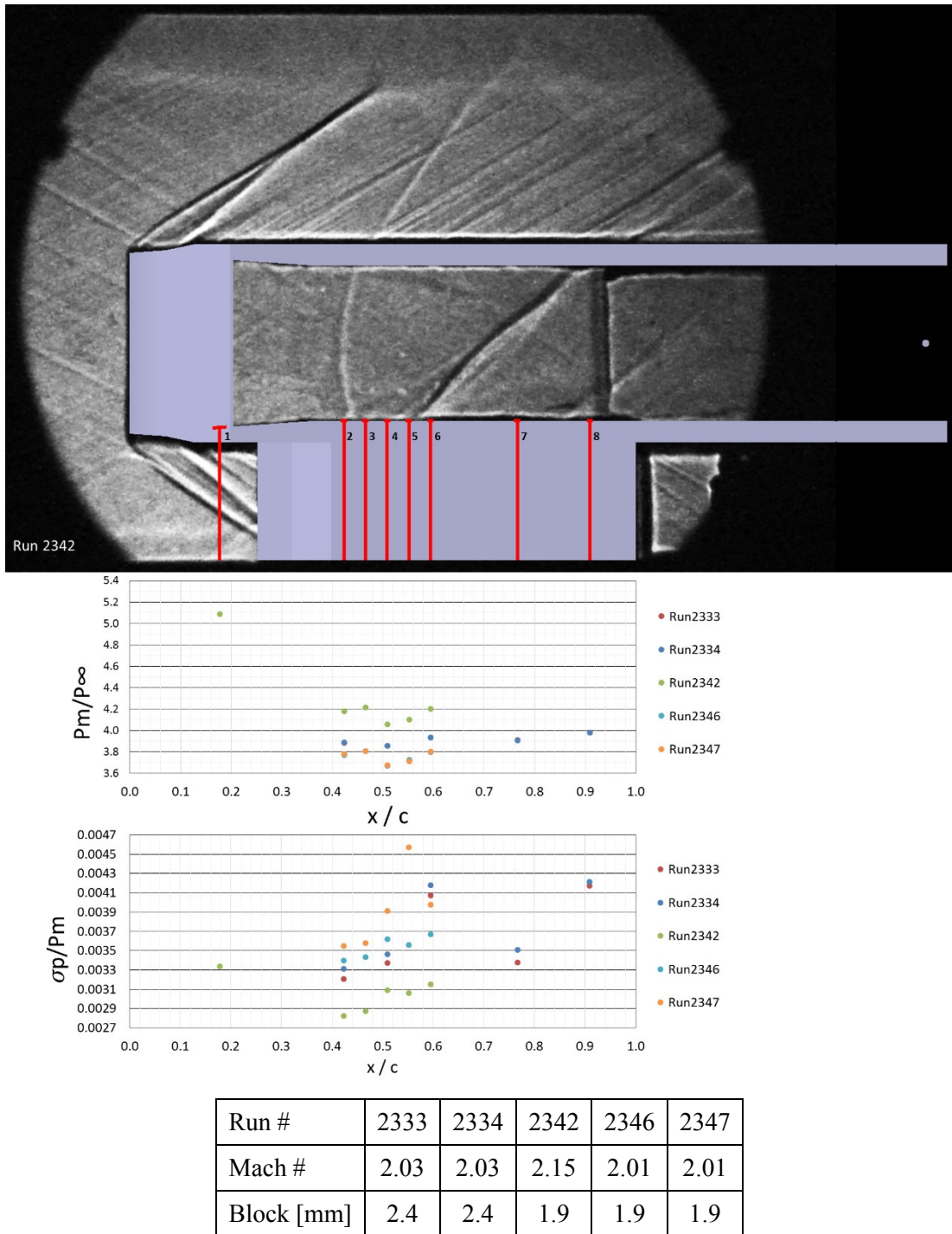


Figure 3.20 : Long unstarted model with block in the center height at the back.

Lastly, surface oil flow visualization method was used to see the flow separation regions as a results of a possible SBLI. Figure 3.21 shows the oil flow image in the short model for the started condition. First separation line in the front was caused by

the upper ramp shock and the second one at the back was due to the reflecting shock of the lower ramp shock. Since SBLIs are not very strong, the boundary layer thickness of the separation regions are not large enough to form a reattachment shock. Oil dilution occur around reattachment region due to the opposite flow directions but no reattachment line appears prominently in the figure. Further details about the theory of SBLI are given in Figure 3.22.

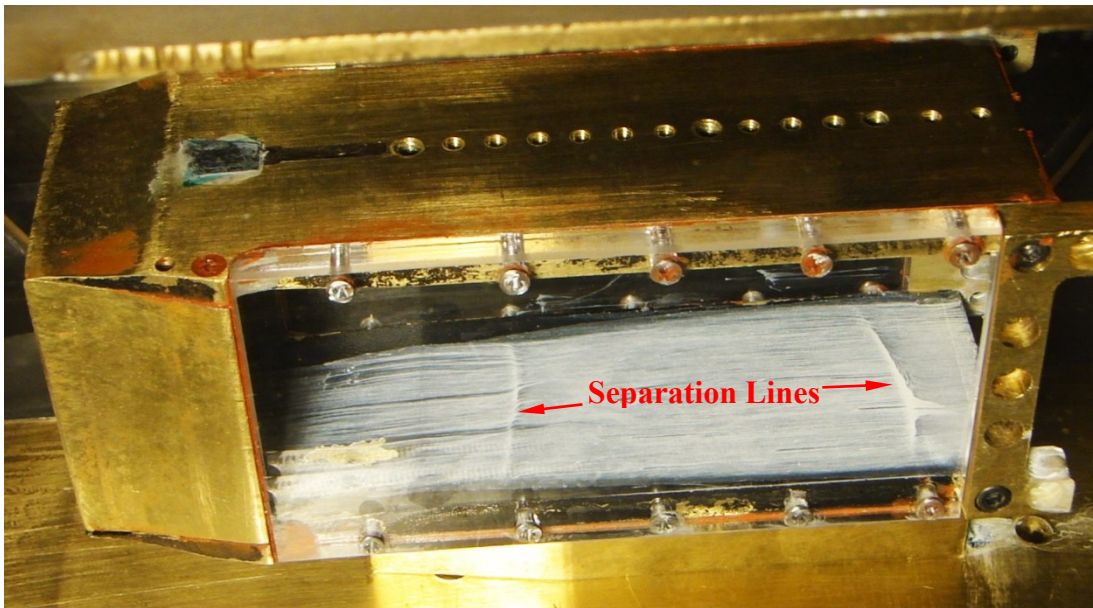


Figure 3.21 : Oil flow image of short started model.

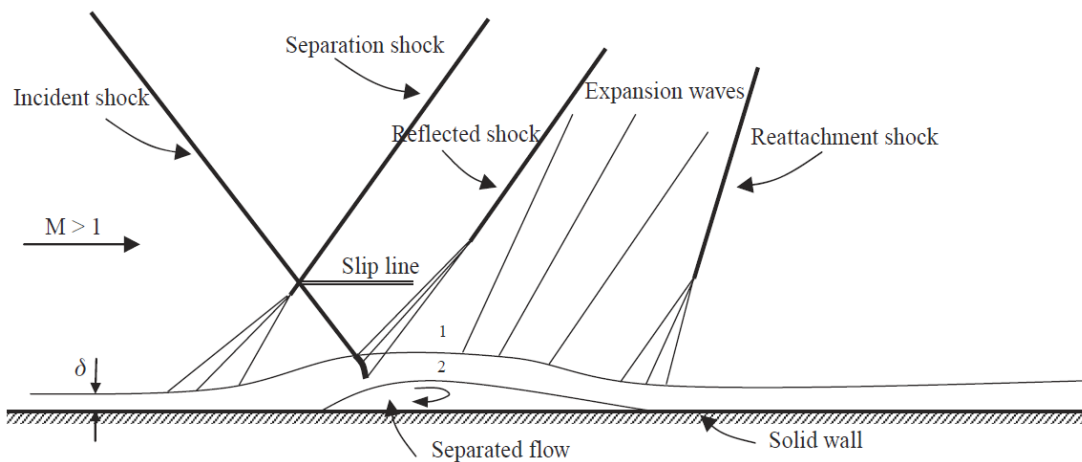


Figure 3.22 : Planar shock-wave/boundary-layer interaction [20].

A simplified schematic sketch of a planar shock-wave-induced boundary-layer separation is illustrated in Figure 3.22 where δ denotes the boundary layer thickness. Pressure increases downstream portion of the impinging shock and this adverse pressure is transmitted to upstream through the subsonic region of the boundary layer, causing the thickening of the boundary layer [20]. Therefore, a region of flow

separation may appear under this adverse pressure. Since the pressure in region 1 is larger than that in region 2, the flow reattaches. Hence, the streamline formation of the boundary layer creates expansion waves followed by a compression shock related to the reattachment. This phenomenon is observed with the help of surface oil flow method where separation lines show boundary layer separation.

4. CONCLUSIONS AND RECOMMENDATIONS

In this study, experimental investigation of an internal compression inlet were carried out. Long and short models were tested with/without different sized blocks. Simultaneous pressure measurements and shadowgraph imaging were made and oil flow visualization method were used to see the separation lines. The importance of the ratio of the captured area to the throat area were observed for internal compression inlets. For the short/long started models, analytical calculations showed a good agreement with the measurements. A significant increase was observed in the RMS values near the SBLI regions. The main purpose of obtaining a normal shock inside the inlet was never achieved during experiments. Most of the blocks caused inlet unstart and it was observed that internal compression inlets did not allow the formation of a stable normal shock after one or more oblique shock reflections. The back pressure created by the exit blokage either forced the started shock waves out of the inlet and caused inlet unstart or made no change on the shock wave structure and the inlet stayed started. In order to overcome this problem for future studies on the subject several recommendations can be carried out:

1. Designing an inlet model with a larger throat cross-section area which reduces three-dimensional effects of corner wall flow interactions and boundary layer effects.
2. Increasing freestream Mach number.
3. Trying new type of blocks which would emerge from the bottom or top surfaces towards the center of the inlet.

For the reasons explained above, external compression inlets have better characteristics on the basis of shock stability. An analytical study was carried out to optimize the total pressure recovery performance for several two-dimensional inlet geometries under inviscid approach. Furthermore, in order to observe SBLI better, ramps having larger angles should be manufactured because they will create stronger shocks and due to the higher adverse pressure gradients SBLI will be more effective.

REFERENCES

- [1] **Mattingly, Jack D.** (2006). Elements of Propulsion: Gas Turbines and Rockets, AIAA Education Series.
- [2] **Raymer, Daniel P.** (1992). Aircraft Design: A Conceptual Approach, AIAA Education Series.
- [3] **Sforza, Pasquale M.** (2012). Theory of Aerospace Propulsion, Elsevier Inc.
- [4] **Seddon, J., & Goldsmith, E. L.** (1999). Intake Aerodynamics, 2nd Edition, AIAA Education Series.
- [5] **Mattingly, Jack D., Heiser, W. H. and Pratt, D. T.** (2002). Aircraft Engine Design, 2nd Edition, AIAA Education Series.
- [6] **Connors, J. F., and Mayer, R. C.** (1956). Design criteria for axisymmetric and two-dimensional supersonic inlets and exits, NACA TN. Note 3589.
- [7] **Huenecke, K.** (2003). Jet Engines, Motorbooks International Publishers & Wholesalers.
- [8] **Trapier, S., Duveau, P. And Deck, S.** (2006). Experimental Study of Supersonic Inlet Buzz, AIAA Journal, Vol. 44, No. 10.
- [9] **Gefroh, D., Loth, E., Dutton, C. And McIlwain, S.** (2002). Control of an Oblique Shock/Boundary-Layer Interaction with Aeroelastic Mesoflaps, AIAA Journal, Vol. 40, No. 12.
- [10] **Srinivasan, K. R., Loth, E. And Dutton, J.C.** (2006). Aerodynamics of Recirculating Flow Control Devices for Normal Shock/Boundary-Layer Interactions, AIAA Journal, Vol. 44, No. 4.
- [11] **Herges, T., Kroeker, E., Elliott, G. And Dutton, C.** (2010). Microramp Flow Control of Normal Shock/Boundary-Layer Interactions, AIAA Journal, Vol. 48, No. 11.
- [12] **Babinsky, H., Li, Y. And Pitt Ford, C. W.** (2009). Microramp Control of Supersonic Oblique Shock-Wave/Boundary-Layer Interactions, AIAA Journal, Vol. 47, No. 3.
- [13] **Rybalko, M., Babinsky, H. And Loth, E.** (2012). Vortex Generators for a Normal Shock/Boundary-Layer Interactions with a Downstream Diffuser, Journal of Propulsion and Power, Vol. 28, No. 1.
- [14] **McCormick, D. C.** (1993). Shock/Boundary-Layer Interaction Control with Vortex Generators and Passive Cavity, AIAA Journal, Vol. 31, No. 1.

- [15] **Valdivia, A., Yüceil, K. B., Wagner, J. L., Clemens, N. T. And Dolling, D. S.** (2009). Active Control of Supersonic Inlet Unstart Using Vortex Generator Jets, 39th AIAA Fluid Dynamics Conference, 22-25 June, San Antonio, Texas.
- [16] **Valdivia, A., Yüceil, K. B., Wagner, J. L., Clemens, N. T. And Dolling, D. S.** (2014). Control of Supersonic Inlet-Isolator Unstart Using Active and Passive Vortex Generators, AIAA Journal, Vol. 52, No. 6.
- [17] **Seçkin, S.** (2012). Flow Visualization of a Scramjet Inlet - Isolator Model in Supersonic Flow, *BSc Thesis*, ITU, Istanbul, Turkey.
- [18] **Holman, J. P.** (2001). Experimental methods for engineers. McGraw-Hill.
- [19] **Schlieren System.** (n.d.). Retrieved April 2012, from NASA:
<http://www.grc.nasa.gov/WWW/k-12/airplane/tunvschlrn.html>
- [20] **Segal, C.** (2009). The Scramjet Engine, Cambridge University Press.

APPENDICES

APPENDIX A: Sound Pressure Level

APPENDIX A

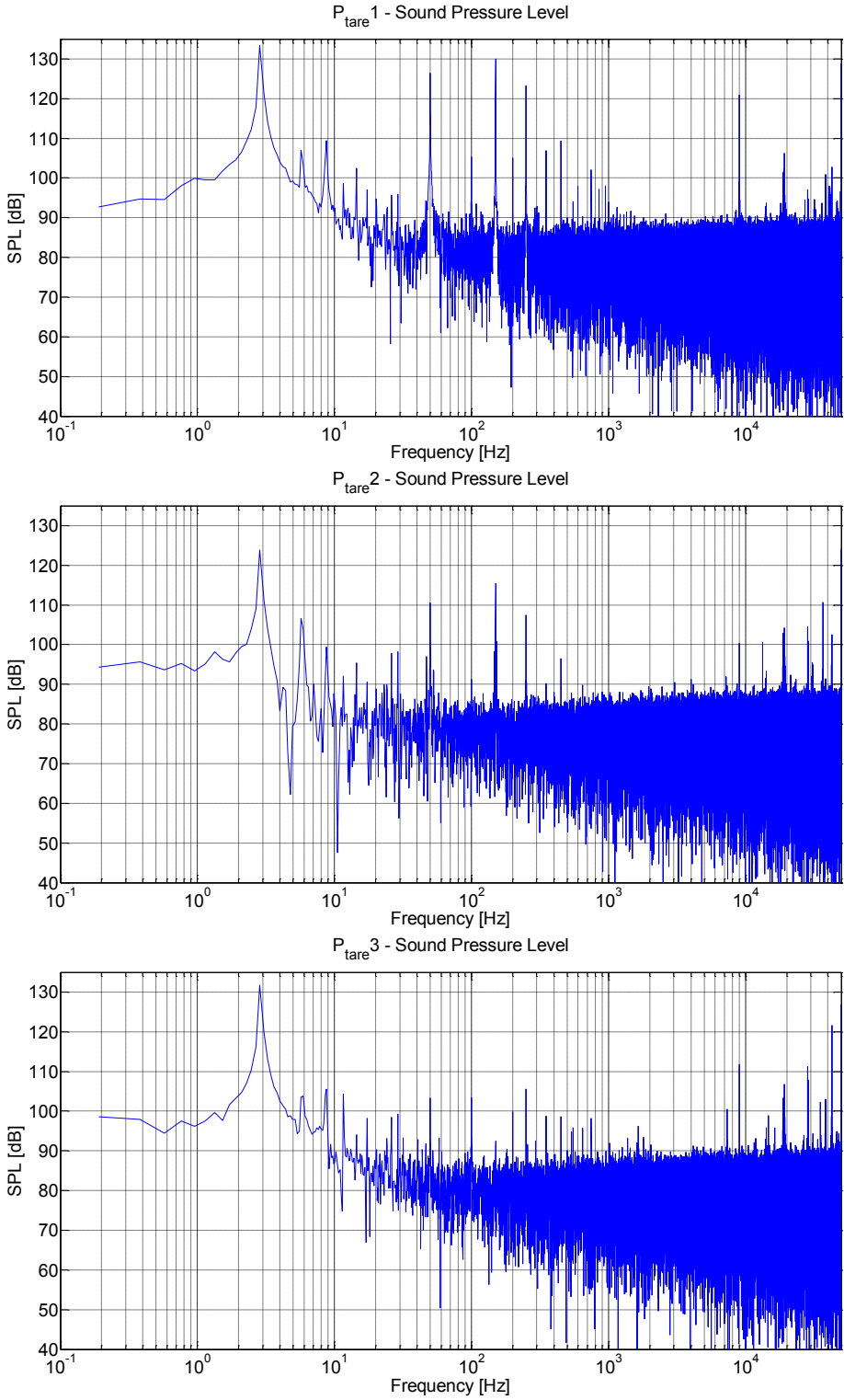


Figure A.1 : Power spectra of the tare pressure at P1, P2 and P3 for Run2352.

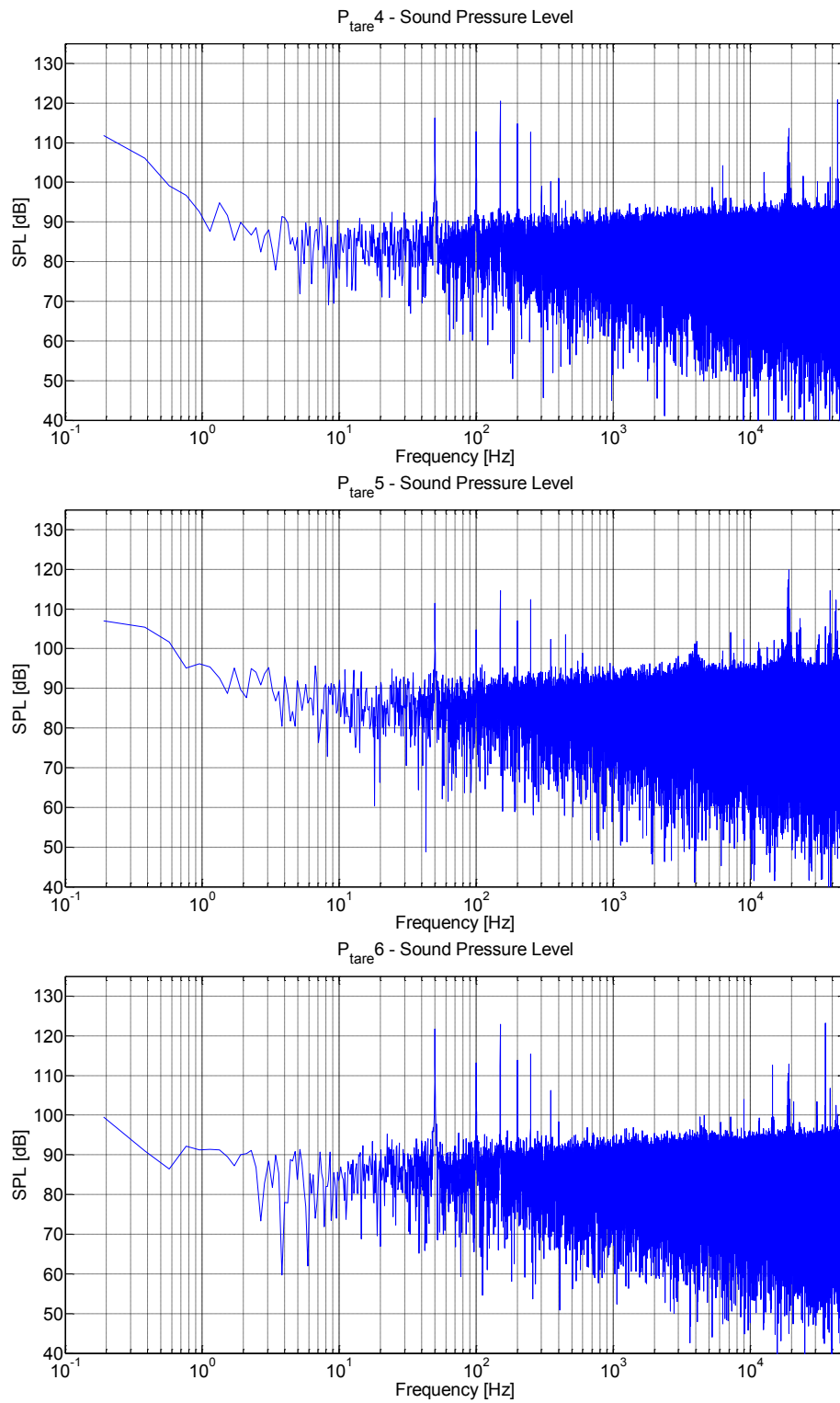


Figure A.2 : Power spectra of the tare pressure at P4, P5 and P6 for Run2352.

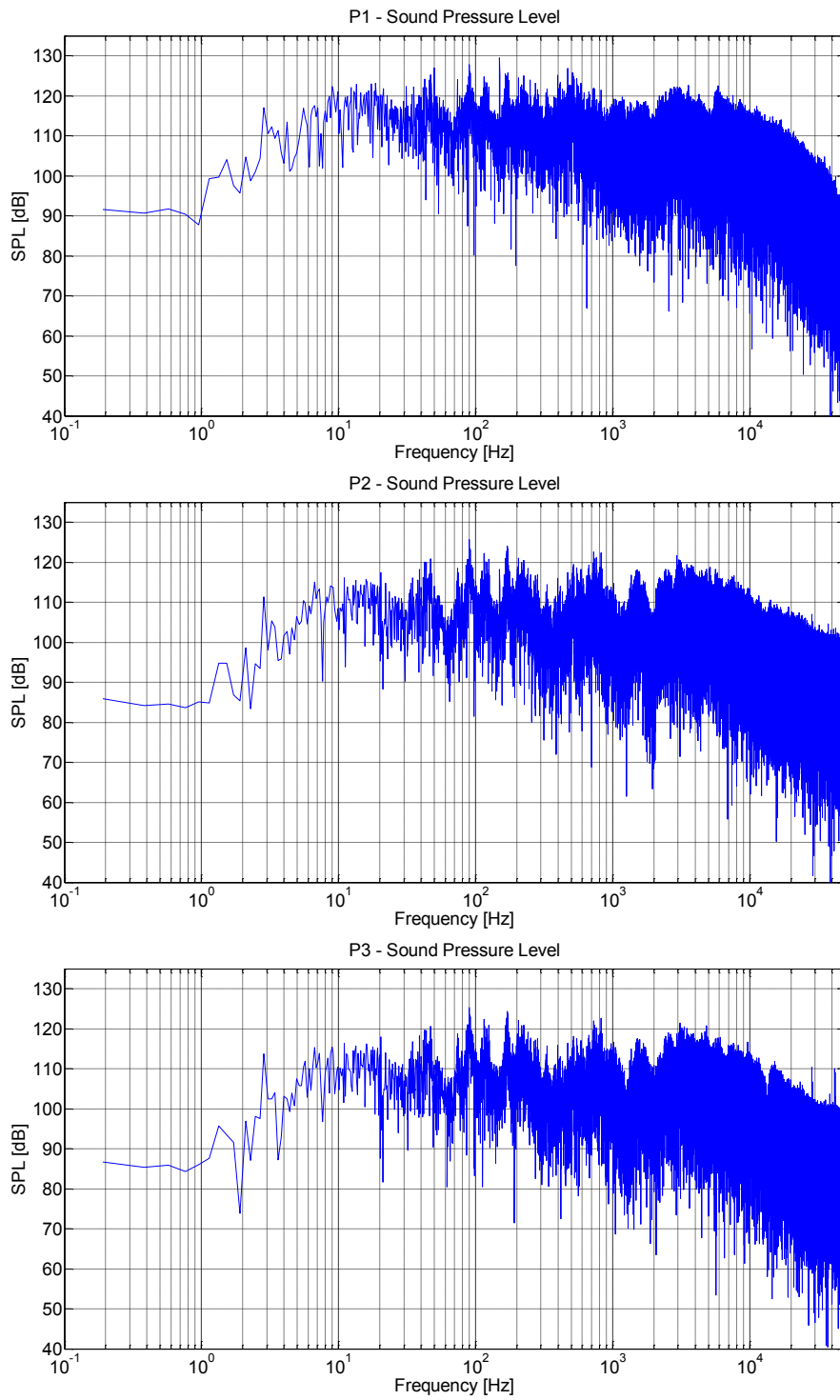


Figure A.3 : Power spectra of the pressure at P1, P2 and P3 for Run2352.

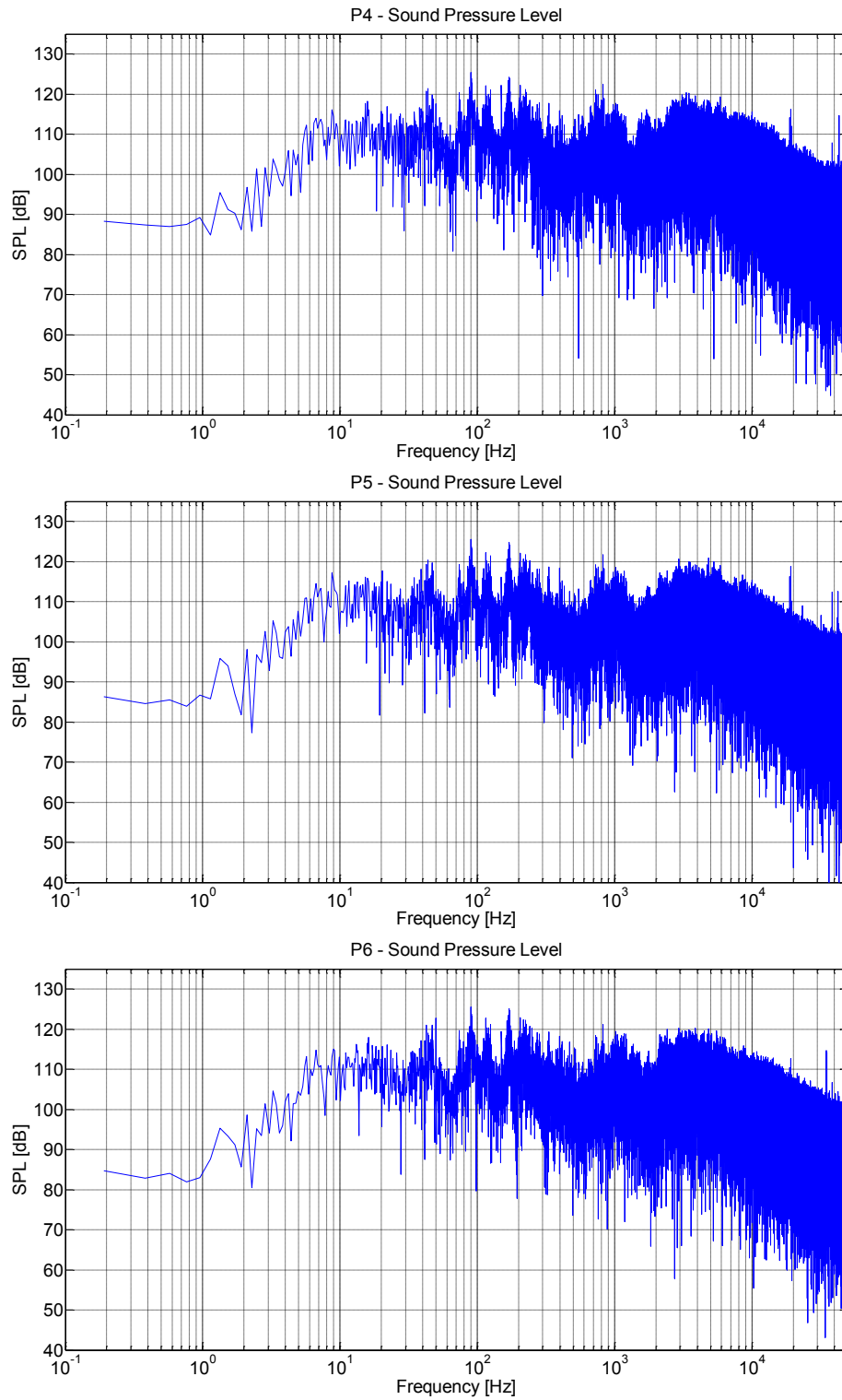


Figure A.4 : Power spectra of the pressure at P4, P5 and P6 for Run2352.

CURRICULUM VITAE



Name Surname: Serdar Seçkin

Place and Date of Birth: Shumen - 18.12.1987

E-Mail: seckins@itu.edu.tr , serdar.seckin@hotmail.com

B.Sc.: Istanbul Technical University - Astronautical Engineering

Istanbul Technical University - Manufacturing Engineering (Double Major)

Awards:

Fulbright Scholarship Grantee Finalist, 2013

Istanbul Technical University, Graduation at High Honor List, 2012

List of Publications:

▪ **Seçkin, S., Yüceil, K. B.,** *Flow Visualization of a Scramjet Inlet - Isolator Model in Supersonic Flow*, Experimental Fluid Mechanics 2012 Conference, 20-23 November 2012, Hradec Kralove, Czech Republic.